VILNIUS UNIVERSITY

MILDA PUČETAITĖ

VIBRATIONAL SPECTROSCOPY AND MICROSPECTROSCOPIC IMAGING OF URINARY STONES AND BIOLOGICAL FLUIDS

Doctoral Dissertation

Physical Sciences, Physics (02P)

Vilnius, 2016

The dissertation has been developed during the years 2012 – 2016 in Vilnius University

Supervisor - Prof. Dr. Valdas Šablinskas (Vilnius University, physical sciences, physics - 02P)

Advisor - Prof. Dr. Per Uvdal (Lund University, physical sciences, physics - 02P)

VILNIAUS UNIVERSITETAS

MILDA PUČETAITĖ

INKSTŲ AKMENŲ IR BIOLOGINIŲ SKYSČIŲ TYRIMAS VIRPESINĖS SPEKTROMETRIJOS IR MIKROSKOPIJOS METODAIS

Daktaro disertacija

Fiziniai mokslai, Fizika (02P)

Vilnius, 2016 metai

Disertacija rengta 2012 – 2016 metais Vilniaus universitete

Mokslinis vadovas - prof. dr. Valdas Šablinskas (Vilniaus universitetas, Fiziniai mokslai, Fizika - 02P)

Mokslinis konsultantas - prof. dr. Per Uvdal (Lundo universitetas, Fiziniai mokslai, Fizika - 02P)

Contents

Abbreviations

ACP – amorphous calcium phosphate

ATR – attenuated total reflection

CARS – coherent anti-Stokes Raman scattering

CCD – charge-coupled device

COD – calcium oxalate dihydrate

COM – calcium oxalate monohydrate

DFT – density functional theory

DTGS – deuterated triglycine sulphate

FIR – far infrared

FTIR – Fourier transform infrared

HCA – hierarchical cluster analysis

IR – infrared

KKT – Kramers-Kronig transform

LSPR – localized surface plasmon resonance

MCT – mercury cadmium telluride

MIR – middle infrared

Nd:YAG – neodymium doped yttrium aluminum garnet

NIR – near infrared

PMT – photomultiplier tube

ROI – region of interest

SERS – surface enhanced Raman scattering

SHG – second harmonic generation

TPEF – two-photon emission fluorescence

Introduction

Rapid advance in biology and medicine leads to an increasing demand of knowledge about chemical composition and structure of related molecular compounds, their function and response to changing environment. Vibrational spectroscopy has been increasingly used for this purpose [1–7]. It provides information about vibrational modes in sample molecules and is a standard method for determination of chemical composition, molecular structure and intermolecular interactions. Versatility of sample preparation methods, possibility to analyze small samples provided by coupling the spectrometers to microscopes and the fact that no labelling is needed to obtain contrast makes vibrational spectroscopy extremely attractive for studies of biological samples: from small molecules to complex structures of proteins, from biological fluids to cells and tissues [8–13].

Many scientific research nowadays is based on a thought that vibrational spectroscopy could also be useful for early diagnostics of diseases [5,14–17]. It allows detecting alterations in biochemistry of cells, tissues, biological fluids, etc. caused by various pathologies. Due to sensitivity of vibrational spectroscopy, these alterations could be discovered earlier than with any other currently available chemical or spectroscopic method. When experiments are performed according to protocol and under constant conditions, vibrational spectroscopy can also provide objective and operator independent results. In addition, availability of fiber optics and the fact that vibrational spectra can be recorded in a fraction of seconds opens up a possibility for diagnosis *in viv*o [12,18–20].

Despite the potential of vibrational spectroscopy methods and a vast amount of laboratory research being carried out, application of vibrational spectroscopy in routine biomedical tests is still episodic. There are

several reasons for this. Firstly, for the method to be approved in medical practice, it has to produce certain values of sensitivity and specificity, go through reliability tests and clinical trials [21,22]. With lack of close cooperation between medics and scientists, this is a difficult task to accomplish. Secondly, analysis of biological samples is challenging in itself due to issues related to sample preparation and spectral analysis [21]. Normally, they contain a mixture of macromolecules which all contribute to the resultant spectrum causing spectral bands to overlap and broaden. While such spectra contain vast amounts of information that can be used for diagnostic purposes, their analysis by simply evaluating peak positions, intensities and half-widths usually gives little use; particularly, when the spectral data set is large. Therefore, data pre-processing algorithms and multivariate statistical analysis for data reduction and classification is necessary [23–25]. Furthermore, samples of various nature and in various environments require consideration of the most suitable approach for their analysis. For instance, solid biological samples, such as urinary stones, often require use of infrared (IR) microscopy in specular reflection mode which yields Reststrahlen spectral bands in the recorded spectra [26]. This method allows obtaining information about both chemical composition and structure of samples as, unlike other techniques, does not require sample grinding. On the other hand, specular reflectance spectra require complex mathematical processing before both qualitative and quantitative analysis can be performed [27]. Standard Kramers-Kronig transform is rarely applicable due to issues related to acquisition of spectra, sample homogeneity and surface roughness. Alternatively to the specular reflection IR microspectroscopy, Raman scattering methods could be applied. While this technique requires no sample preparation, fluorescence background is a common issue when biological samples are analyzed. In addition, due to low yield of Raman scattered photons, spectral acquisition time is long.

Low efficiency of Raman scattering also prevents it from applications in detection of small concentrations of substances in solutions, such as biological fluids. This can be overcome by using signal enhancement by metal nanoparticles – surface enhanced Raman scattering spectroscopy. The challenge for this method to be used in clinical practice lies in achieving reproducibility and selectivity when biological fluids of complex compositions are analyzed [28,29].

Finally, despite the fact that complementary use of vibrational spectroscopy techniques provides the best perspectives for their practical applications, they are often viewed at as separate and competing techniques. This limits their acceptance among other routine methods.

Goals and tasks of the thesis

Responding to the challenges highlighted above, **the main goal of this thesis** is complementary application of vibrational spectroscopy and microspectroscopy methods for analysis of biomedical samples - urinary stones, urinary deposits and biological fluids. The work is focused on adapting the methods and data analysis techniques to obtain reliable and repeatable results. To achieve this goal, the following **tasks were formulated**:

1. Apply and evaluate potential of vibrational spectroscopy and microspectroscopy techniques for comprehensive morphochemical analysis of human urinary stones.
2. Apply and evaluate potential of infrared spectroscopy and microspectroscopy for chemical analysis of urinary deposits.
3. Explore enhancement effects of various drop-dried colloidal substrates with differently shaped silver nanoparticles and find optimal experimental conditions for detection traces of uric acid in aqueous solutions by means of surface enhanced Raman scattering (SERS) spectroscopy and perform

assignment of the SERS spectral bands by means of density functional theory calculations.

4. Perform infrared spectral analysis of extracellular fluid taken from healthy and tumor kidney tissue during nephrectomy surgery for identification of spectral markers of cancer.

Statements of the thesis

1. Specular reflection IR microspectroscopy in MIR and FIR spectral region can be efficiently used for chemical imaging of solid, rough surface samples such as human urinary stones only when specific spectral pre-processing is performed.

2. Epi-detected non-linear optical imaging provides chemically sensitive information concerning microstructure of urinary stones at lateral resolution higher than 1 μm.

3. Macro-ATR IR spectroscopy is found to be superior method to conventional optical microscopy for determining chemical composition of atypical crystal, poly-crystal and amorphous urinary deposits.

4. Semi-quantitative analysis of uric acid in biological fluids by means of colloidal SERS with detection limits down to 10^{-6} M is possible only when special drop-drying technique is used for preparation of the substrates.

5. Statistical multivariate analysis applied to IR spectral bands of glycogen in the spectral region of C-O stretching vibrations allows differentiating between healthy and cancerous kidney tissue with sensitivity up to 91 %.

Novelty and relevance of the results

- Complementary use of vibrational spectroscopy techniques has the best prospects for practical biomedical applications due to their versatility regarding sample size, aggregation state or concentration.
- In this work we show for the first time that for solid samples, such as urinary stones, diffuse reflection influence has to be taken into account for reliable qualitative and semi-quantitative analysis using specular reflection IR microspectroscopy. This can be done either by subtracting the diffuse reflection component from the specular reflection spectra or by applying FIR radiation for the analysis.
- Despite the fact that nonlinear optical microscopy has been mostly used for analysis of tissues and lipid structures, the method is suitable to determine both chemical composition and microstructure of urinary stones for more comprehensive pathogenesis of urolithiasis.
- The only currently applied method for early diagnosis of urolithiasis – optical microscopy of urinary deposits – is unreliable both in detecting the deposits and determining their chemical composition. Macro-ATR IR spectroscopy is found to be superior method for determining chemical composition of atypical crystal, poly-crystal and amorphous urinary deposits.
- Possibility to obtain quantitative information about low concentration substances in solutions (or biological fluids) by means of SERS is of great importance if the method is going to be used in clinical practice. We show that for detection of uric acid by colloidal SERS technique it is possible only when special drop-drying technique is used for preparation of the substrates
- IR spectroscopic analysis of extracellular fluid is a new, never before applied method for differentiation of healthy and cancerous tissue.

Publications included in the thesis

Peer-reviewed publications

1. M. Pucetaite, V. Hendrixson, A. Zelvys, F. Jankevicius, J. Ceponkus, V. Sablinskas, Application of Infrared Spectroscopical Imaging in Specular Reflection Mode for Morphological Studies of Urinary Stones, J. Mol. Struct. **1031**, 38-42 (2013).
2. S. Tamošaitytė, V. Hendrixon, A. Želvys, R. Tyla, Z. A. Kučinskienė, F. Jankevičius, M. Pučetaitė, V. Jablonskienė, V. Šablinskas, Combined studies of chemical composition of urine sediments and kidney stones by means of infrared microspectroscopy, J. Biomed. Opt. **18(2)**, 027011 (2013).
3. M. Pucetaite, S. Tamosaityte, A. Engdahl, J. Ceponkus, V. Sablinskas, P. Uvdal, Microspectroscopic Infrared Specular Reflection Chemical Imaging of Multi-Component Urinary Stones: MIR vs. FIR, Cent. Eur. J. Chem. **12(1)**, 44-52 (2014).
4. M. Pucetaite, M. Velicka, J. Pilipavicius, A. Beganskiene, J. Ceponkus, V. Sablinskas, Uric acid detection by means of SERS spectroscopy on dried Ag colloidal drops, J. Raman Spectrosc. **47(6)**, 681-686 (2016).
5. M. Pucetaite, S. Tamosaityte, R. Galli, V. Sablinskas, G. Steiner, Microstructure of urinary stones as studied by means of multimodal nonlinear optical imaging, J. Raman Spectrosc, n/a-n/a (2016) (online Early View, DOI: 10.1002/jrs.4985).

Conference proceedings

1. M. Pucetaite, P. Banys, V. Sablinskas, Application of infrared reflection microspectroscopy for chemical imaging of cross-sectioned urinary calculi, Proc. of SPIE **8798**, 87980U (2013); doi:10.1117/12.2032506.

2. M. Pucetaite, M. Velicka, S. Tamosaityte, V. Sablinskas, Application of SERS spectroscopy for detection of trace components in urinary deposits, Proc. of SPIE **8957,** 895708-1 (2014); doi: 10.1117/12.2040386.
3. V. Urboniene, M. Velicka, J. Ceponkus, M. Pucetaite, F. Jankevicius, V. Sablinskas, G. Steiner, Intra-operative on-line discrimination of kidney cancer from normal tissue by IR ATR spectroscopy of extracellular fluid, Proc. of SPIE **9704**, 97040E (2016); doi:10.1117/12.2213408.

Papers not included in the thesis

1. S. Tamosaityte, E. Baltakyte, D. Blazevic, M. Pucetaite, J. Ceponkus, V. Hendrixson, S. Varvuolytė, V. Sablinskas, Baseline correction of infrared absorption spectra of urinary sediments by taking Mie scattering effects into account, Proc. of SPIE **8798**, 87980V (2013); doi:10.1117/12.2032508.
2. V. Urboniene, M. Pucetaite, F. Jankevičius, A. Želvys, V. Sablinskas, G. Steiner, Identification of kidney tumor tissue by infrared spectroscopy of extracellular matrix, J. Biomed. Opt. **19(8)**, 087005 (2014).
3. J. Ceponkus, M. Jonusas, C. P. Cotter, M. Pucetaite, V.Aleksa, G. A. Guirgis, V. Sablinskas, Structural Studies of 1,1-Dimethyl-2-oxy-1-silacyclohexane by Means of Matrix Isolation Infrared Absorption Spectroscopy, J. Phys. Chem. A **119(11)**, 2721-2726 (2015).
4. J. Ceponkus, V. Sablinskas, V. Aleksa, M. Pucetaite, R. Platakyte, C. W. Reed, C. Cotter, G. Guirgis, Raman and infrared spectroscopic studies of structure and stability of 1,1,2,2-tetrachloro-1,3-disilacyclopentane, Vib. Spectrosc. **81**, 136–43 (2015).
5. M. Velicka, V. Urboniene, J. Ceponkus, M. Pucetaite, F. Jankevicius, V. Sablinskas, Detection of cancerous biological tissue areas by means of infrared absorption and SERS spectroscopy of intercellular fluid, Proc. of SPIE **9550**, 95500A, (2015); doi:10.1117/12.2186395.

6. A. Stirke, R.-M. Apetrei, M. Kirsnyte, L. Dedelaite, V. Bondarenka, V. Jasulaitiene, M. Pucetaite, A. Selskis, G. Carac, G. Bahrim, A. Ramanavicius, Synthesis of Polypyrrole Microspheres by Streptomyces Spp., Polymer **84**, 99–106 (2016).
7. J. Pilipavicius, R. Kaleinikaite, M. Pucetaite, M. Velicka, A. Kareiva, A. Beganskiene, Controllable Formation of High Density SERS-Active Silver Nanoprism Layers on Hybrid Silica-APTES Coatings, Appl. Surf. Sci. **377**, 134–40 (2016).

Conference abstracts

1. Valdas Sablinskas, Milda Pucetaite, Justinas Ceponkus, Chemical Imaging of Heterogeneous and Rough Surfaces by Means of Infrared Microspectroscopy in Specular Reflection, ScIX2012 39th annual meeting of FACSS, Kansas City, USA
2. Sandra Tamošaitytė, Evelina Baltakytė, Milda Pučetaitė, Valdas Šablinskas, Šlapimo nuosėdų cheminės sudėties tyrimai FT-Ramano sklaidos spektriniu metodu, 40-oji Lietuvos Nacionalinė Fizikos Konferencija, 2013, Vilnius, Lietuva
3. Milda Pucetaite, Jonas P. Banys, Sandra Tamošaitytė, Justinas Čeponkus, Valdas Šablinskas, Biologinių paviršių cheminio vaizdinimo panaudojant infraraudonosios spinduliuotės veidrodinio atspindžio spektrus ypatumai, 40-oji Lietuvos Nacionalinė Fizikos Konferencija, 2013, Vilnius, Lietuva
4. Milda Pucetaite, Jonas P. Banys, Valdas Šablinskas, Application of Infrared Reflection Microspectroscopy for Chemical Imaging of Cross-sectioned Urinary Calculi, European conferences on biomedical optics (ECBO) (part of congress World of photonics) 2013, Munich, Germany
5. Sandra Tamosaityte, Evelina Baltakyte, Dominyka Blazevic, Milda Pucetaite, Justinas Ceponkus, Sonata Varvuolyte, Vaiva Hendrixson and

Valdas Šablinskas, Baseline Correction of IR Spectra of Urinary Sediments by Taking *Mie* Scattering Effects into Account, European conferences on biomedical optics (ECBO) (part of congress World of photonics) 2013, Munich, Germany

6. Milda Pucetaite, Martynas Velicka, Valdas Sablinskas, Application of SERS spectroscopy for detection of trace components in urinary deposits, Photonics West 2014, San Francisco, USA
7. Vidita Urboniene, Milda Pucetaite, Feliksas Jankevicius, Valdas Sablinskas, Gerald Steiner, IR spectroscopical studies of intercellular liquid as tool for cancer detection, Photonics West 2014, San Francisco, USA
8. Milda Pucetaite, Martynas Velicka, Jurgis Pilipavicius, Almira Ramanaviciene, Indre Aleknaviciene, Evaldas Pabreza and Valdas Sablinskas, Comparative study of Raman enhancement effect for uric acid on various SERS substrates, EUCMOS 2014, Dusseldorf, Germany
9. Milda Pucetaite, Dominyka Blazevic, Elvyra Malysko, Vaiva Hendrixson and Valdas Sablinskas, Infrared spectroscopic analysis of urinary sediments: transmission vs. ATR, EUCMOS 2014, Dusseldorf, Germany
10. Milda Pučetaitė, Sandra Tamošaitytė, Roberta Galli, Gerald Steiner, Valdas Šablinskas, CARS mikroskopijos taikymas inkstų akmenų cheminiam vaizdinimui (Chemical Imaging of Urinary Stones by CARS Microscopy), 41-oji Lietuvos Nacionalinė Fizikos Konferencija, 2015, Vilnius, Lietuva
11. Milda Pučetaitė, Martynas Velička, Jurgis Pilipavičius, Valdas Šablinskas, SERS spektrometrijos taikymas šlapimo rūgšties aptikimui biologiniuose skysčiuose (Application of SERS Spectroscopy for Detection of Uric Acid in Biological Fluids), 41-oji Lietuvos Nacionalinė Fizikos Konferencija, 2015, Vilnius, Lietuva
12. Martynas Velicka, Milda Pucetaite, Justinas Ceponkus, Valdas Sablinskas, Application of various colloidal SERS approaches for detection of traces of uric acid, Global Biotechnology Congress 2015, Boston, USA

Participation in funded science projects

Major part of the studies presented in this thesis was supported by:

- Project funded by The State Studies Foundation „Studies of Relations between kidney stone disease and metabolic syndrome“ (2010-2011).
- Project funded by Lithuanian Research Council „Diagnostical studies of chronical noninfectious diseases by means of infrared spectral microscopy“ (2011-2012).
- Project funded by European Social Fund „Synthesys of Materials for Advanced Semiconductor and Nano Technologies and its Characterization by Means of Steady-state and Ultrafast Spectroscopies in Wide Spectral Range“ (2013-2015).
- Project funded by Lithuanian Research Council „Spectroscopic express analyzer of cancerous tissue“ (2015-2018).

Author’s contribution

For the results of the analysis of urinary stones presented in this thesis, all the experimental work, data analysis and the substantial part of publication writing was done by the author of the thesis. The experimental work for the analysis of urinary deposits was performed by Sandra Tamošaitytė, Dominyka Blaževič and Evelina Baltakytė. The author participated in conceiving the ideas and the writing, performed major part of data analysis. All the results presented in this work on detection of small concentrations of uric acid in aqueous solutions were obtained by the author through experimental work, data analysis and theoretical calculations. Substantial part of the publication on the topic was also written by the author. Major part of experimental work on extracellular fluid analysis was performed by Doc. Vidita Urbonienė and Martynas Velička, although the

author also participated in some of them. Data analysis of the recorded spectra, the results of which are presented in this thesis, and part of the writing was performed by the author.

Chapter 1 Biomedical applications of vibrational spectroscopy: current status and technical advances

1.1. Vibrational spectroscopy measurement techniques and their biomedical applications

Vibrational spectroscopy is a classical method for material characterization. It probes molecular vibrations within samples. Frequencies of these vibrations uniquely define chemical composition and structure of molecules within given environment. Two main techniques of vibrational spectroscopy are infrared (IR) absorption and Raman scattering spectroscopy.

Radiation absorption in matter is associated with various processes one of which is transition between energy states of an atom or a molecule. For the transition to take place, the energy (i.e., frequency) of the incident photon has to be equal to the band gap between the states. Absorption of infrared radiation corresponds with transitions between vibrational energy levels. IR radiation covers spectral region between 10000 and 10 cm^{-1} (corresponding wavelengths - 1 and 1000 μm). This region is further subdivided into three smaller intervals: near infrared (NIR) – 10000÷ 4000 cm^{-1}, middle infrared (MIR) - 4000÷200 cm^{-1} and far infrared (FIR) – 200÷10 cm^{-1}. Most of fundamental vibrational transitions are found in the MIR spectral region; however, some vibrational transitions can also appear in NIR (mostly combinations and overtones of fundamental vibrations) or FIR (vibrations of heavy atoms or intermolecular vibrations) spectral regions [30,31].

Fourier transform infrared (FTIR) spectrometers are used to record IR absorption spectra [31]. Since it is a standard technique, it will not be discussed in detail here. The recorded IR absorption spectrum is unique to a given compound and is often referred to as “fingerprint” of molecules. Thus, analysis of the IR absorption spectra allows identification of chemical composition of molecular substances. For instance, frequencies of vibrational modes when only a few atoms have large displacements and the rest of the

molecule remains stationary are characteristic to functional groups in which the vibrations are centered. When the vibrations involve displacements of many atoms (skeletal modes), the frequencies of absorption bands are specific to structure of the molecule.

Raman scattering spectroscopy is a complementary or alternative technique to the infrared absorption spectroscopy. It is based on inelastic scattering of monochromatic light – a phenomenon when frequency of the incident radiation changes due to its interaction with molecular vibrations [30,32]. Both dispersive and FT spectrometers can be used to record Raman scattering spectra. Dispersive Raman scattering spectrometers with excitation lasers emitting light in the visible spectral region (VIS) and either photomultiplier tubes (PMT) or charge-coupled device (CCD) detectors for signal detection are the most popular. However, excitation with visible lasers often produces fluorescence in colorful samples and samples with impurities. The fluorescent background overwhelms the weak Raman scattering signal and makes it difficult or impossible to analyze. The fluorescence effect can be minimized by use of lasers emitting radiation in the NIR spectral region. There are two major drawbacks of using these lasers, however. First, high laser power is required to obtain signal, due to the intensity being inversely proportional to the power of four of the excitation wavelength; second, sensitivity of detectors in the NIR spectral region is much lower than sensitivity of PMTs or CCDs in the visible spectral region. Low signal-to-noise ratio caused by these factors can be overcome by averaging a lot of spectra which is only reasonable if FT-Raman spectrometer is used.

Similarly as IR absorption spectra, Raman scattering spectra are unique to molecular substances and can be used for their identification. Of note is that the most information about samples can be gained by complementary application of the both methods. For instance, molecules having an inversion center obey alternative forbiddance rule: their vibrations

are either infrared (asymmetric modes) or Raman (symmetric modes) active [30].

Versatility, chemical and structural sensitivity of vibrational spectroscopy makes it extremely attractive for studies of biological systems. With development of novel techniques it has become possible to analyze bio-samples regardless of their aggregation state, environment they are in, etc. and address specific questions related to their composition, structure, intermolecular interactions and function. While there are a number of such techniques (for instance, surface enhanced IR absorption (SEIRA) spectroscopy, nano-IR spectroscopy, spatially offset Raman spectroscopy, etc.) only the ones related to this work will be covered in the following sections. Both their advantages and shortcomings will be discussed as well as their most important applications for analysis of biological samples highlighted.

1.2.1. Accessories of FTIR spectrometer: ATR units

In addition to the common transmission measurements, FTIR spectrometers can have various attachments which expand their capabilities. For instance, attenuated total reflection (ATR) units are widely used as they simplify sample preparation to a great extent. The ATR method is based on a total internal reflection phenomenon at the interface between ATR element of high refractive index and the sample of lower optical density [31]. At the point of the reflection, electromagnetic field of the incident IR radiation penetrates into the sample and decays exponentially with the distance from the interface (evanescent wave). Thus, the reflected beam contains spectral information about absorbance in the sample. The depth of penetration depends on the wavelength (λ), refractive indices of the ATR element and the sample (n_1 and n_2) and the angle of incidence (θ):

$$d = \frac{\lambda}{2\pi n_1 \sqrt{\sin^2 \theta - (n_2/n_1)^2}}. \quad (1)$$

As the penetration depth is linearly dependent on the wavelength, absorption bands at the lower wavenumbers (larger wavelengths) of the spectrum will be of smaller intensity than at the larger wavenumbers (smaller wavelengths). This effect is compensated by applying correction to the absorbance spectra:

$$ATR = AB \cdot \frac{\tilde{\nu}}{1000}, \quad (2)$$

here *AB* is absorbance spectrum, *ATR* – spectrum after the correction and $\tilde{\nu}$ - wavenumber.

ATR technique enables analysis of gaseous, liquid and solid samples with minimal sample preparation as long as it is possible to obtain full contact between the ATR element and the sample. It does not require samples to be thin as the volume where the spectrum is measured is determined by the penetration depth. Single and multiple internal reflection ATR elements are available. The materials mostly used as the ATR elements are listed in Table 1.

Table 1. Materials used as ATR elements and their refractive indices at 10 μm wavelength [33].

Material	Refractive index
Zinc selenide (ZnSe)	2,41
Germanium (Ge)	4,00
Silicon (Si)	3,42
Diamond	2,38

The fact that FTIR ATR technique does not require any specific sample preparation, is non-destructive and label-free makes it extremely attractive for various biomedical applications. To name a few, the method has been applied to find biomarkers in urine samples [34], diagnose brain cancer

from serum [35,36], detect harmful additives in food (meat, milk, and other) [37–40], etc. Moreover, use of array (focal-plane array – FPA) detectors allows employing the ATR technique for chemical imaging, for which not only no sample preparation is needed, but spatial resolution is enhanced as well [41]. Since incident radiation is travelling through the ATR element of high refractive index (*n*) before it hits the sample adhered to it, numerical aperture (NA) and, in turn, diffraction limited spatial resolution (*r*) is increased [41]: $r = \frac{0.61\lambda}{\mathrm{NA}}$, here $NA = n \cdot \sin\alpha$. α is a half-angle of the radiation cone that enters/exits the objective. FTIR ATR chemical imaging has been used for analysis of both dried and live cells at sub-cellular level [42,43], for analysis of breast tissue to find small mineral calcifications [44], for analysis of processes in microfluidic systems [45], etc.

1.2.2. Accessories of FTIR spectrometer: microscope

FTIR microscopes may be used for analysis of micro-samples or imaging/mapping of macro-samples. The smallest details that can be analyzed

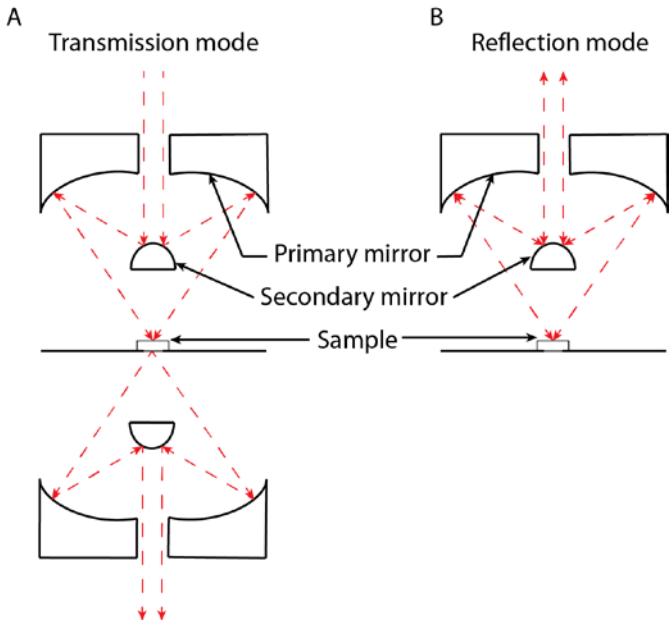

Fig. 1. Scheme of Cassegrain objective in (A) transmission and (B) reflection modes.

are limited by diffraction and for MIR radiation are as small as ~10×10 μm. In the microscope, radiation from the interferometer is usually focused onto the sample and collected into the detector by Cassegrain optics (Fig. 1). Microscopes can operate both in transmission (Fig. 1 A) and reflection modes (Fig. 1 B). MCT single-point or FPA detectors are used for signal detection. In order to view at the sample and select regions of interest (ROI), visible radiation is directed onto the sample through the optics as well. The sample may be viewed at through an ocular or CCD camera.

Emergence of IR microscopes has expanded the capabilities of IR spectroscopy as imaging of samples with chemical sensitivity and specificity became available. In the biomedical field, IR microspectroscopic imaging of fixed cells and tissues has been of particular importance. It has been used to uncover protein folding in cells in order to diagnose diseases such as Alzheimer's, Parkinson's, Huntington's and others [46–49]. Tissue imaging has mostly been used in order to determine boundaries between cancerous and healthy tissue in prostate, kidneys, breast, colon etc. [50–54]. In all these studies the method has shown excellent correlation with histopathological images and has a potential to be used in clinical practice. IR microspectroscopy in reflection mode allows analyzing thick, solid samples such as bone [55]. However, reflectance spectra are influenced by anomalous dispersion of refractive index which distorts the spectral band shapes [27]. This issue prevents wider applications of IR microspectroscopy in reflection mode. Since analysis of reflectance spectra is within the scope of this thesis it will be more extensively discussed in sections 1.3.4, 2.4.1 and 2.4.2.

Synchrotron has been increasingly used as a radiation source for IR microspectroscopy. Due to beam properties of synchrotron radiation (SR), its use allows increasing spatial resolution when chemical images are made through mapping. SR has been used for imaging biomedical samples from cells and tissues to human hair sections and bones [46,56–60]. Despite the

fact that SR is considered an ideal source in FIR spectral range, FIR has rarely been used for analysis of biosamples. The main reason for this is that water, which is abundant in most of the biosamples, has an intense absorption in the FIR spectral region.

1.2.3. Raman scattering spectroscopy techniques: surface enhanced Raman scattering – SERS

Raman scattering spectroscopy is often considered complementary to the IR absorption spectroscopy rather than stand-alone technique due to its low yield. However, Raman scattering signal can be considerably (up to 10^8) enhanced by locating sample molecules in the vicinity of metal (Ag, Au, Cu, Pt) nanoparticles – a phenomenon known as surface enhanced Raman scattering (SERS) [61]. There are two possible enhancement mechanisms: (I) electromagnetic and (II) chemical. The former one is responsible for approximately 10^3-10^7 of the overall enhancement. It takes place when the nanoparticles are affected by external electromagnetic field (the field is constant at a given moment of time if the nanoparticle is much smaller than the radiation wavelength) of incident laser radiation and localized surface

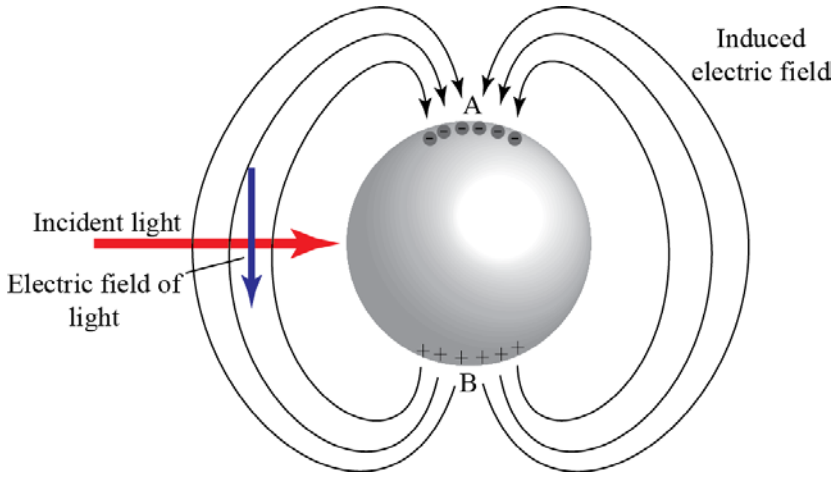

Fig. 2. Interaction between metal nanoparticle and electromagnetic field of incident light.

plasmons – collective oscillations of electrons – are induced. They produce a local electromagnetic field around the nanoparticles (Fig. 2.) which is the strongest at the two points (A and B) along the axis of the nanoparticle directed parallel to the external field. In addition, at these points the directions of the local field coincides with the direction of the external field; thus, superposition of the fields yields an intensity enhancement. If a molecule is located in either one of these positions, its Raman scattering signal is enhanced as well. The enhancement is even larger if the molecule is in a small gap – so called hot spot - between two nanoparticles [61,62].

An important condition to obtain high Raman scattering signal enhancement is to attain resonance (local surface plasmon resonance – LSPR) between the frequency of incident radiation and natural frequency of the plasmons determined by the nature of the metal, size and shape of the nanoparticles. It has been shown that metals are useful as plasmonic materials if the real part of their dielectric function ($\mathrm{Re}(\varepsilon(\lambda))$) in the wavelength region of excitation is both large and negative [62]. For this reason, silver and gold which both meet these conditions are the most widely used in SERS applications. When the size of the nanoparticles increases, the LSPR red-shifts and is damped. The shape of the nanoparticles also influences the position and intensity of the LSPR. For instance, the LSPR of Ag nanoprisms is red-shifted from 400-450 nm to 700-1000 nm as compared to the spherical Ag nanoparticles. In addition, resonance conditions could be met for more than one wavelength which makes it easier to select the excitation laser for the SERS experiment to obtain maximum enhancement [62].

The second, chemical, enhancement mechanism is responsible for only additional factor of 10 of the overall enhancement. It stems from the interactions between the analyte molecule and the metal, such as electron transfer between the two [62].

When analyzing biological molecules, and, in particular, when creating biosensors it is important to achieve reproducibility of the recorded SERS spectra to be able to perform quantitative analysis. This remains the major drawback of SERS spectroscopy since there are many factors that can affect the intensity of the spectra [63]. Firstly, preparing identical uniform substrates is only possible by implementing relatively expensive and complex lithography techniques. Synthesizing colloidal metal nanoparticle solutions is cheap and easily available; however, reproducible results are hardly achievable when they are used in SERS spectroscopy. Adsorption characteristics of analyte molecules on the metal nanoparticles influence the SERS signal intensity as well. For instance, different extent of surface coverage may lead to different molecule orientation, and in turn, due to surface selection rules [64], different relative intensities of SERS spectral bands [63]. In addition, SERS signal intensity depends on the overall surface coverage, described by adsorption isotherms. It has been shown, that with increasing number of molecules adsorbed on the metal nanoparticle surface, the SERS signal intensity increases and, at a certain point, reaches its maximum value. Further addition of molecules does not increase the signal intensity and might even reduce it, as the “free”, not adsorbed molecules damp the resonance of the nanoparticles [63].

Despite the issues mentioned above, SERS spectroscopy has been increasingly proposed as a method of choice for disease diagnosis and prevention [65–68]. Due to its high sensitivity the method has mostly been used for detection of low concentration substances in biological fluids such as urine, blood, saliva, tears, etc. [69–74]. It has also been employed to differentiate between bacterial strains for detection of disease inducing microorganisms in food and water [75–78]. Moreover, imaging of cells and tissues by use of SERS labeling has been reported both *ex-* and *in vivo* [79–81]. However, the biggest issue with SERS spectroscopy that prevents it from

being used in routine clinical practice is production of metal nanoparticle substrates that would provide reproducible results suitable for quantitative analysis.

1.2.4. Raman scattering spectroscopy techniques: coherent anti-Stokes Raman scattering - CARS

Another technique that allows obtaining much higher Raman scattering signal is coherent anti-Stokes Raman scattering (CARS) microscopy [82]. CARS is a four-wave mixing process based on sample excitation using two ultra-short spatially and temporally tuned lasers. The frequency difference of these lasers is selected to match the energy of molecular oscillations (Fig. 3). For the four photons that are involved in the CARS process, phase matching condition has to be met (Fig. 3). This is the case for

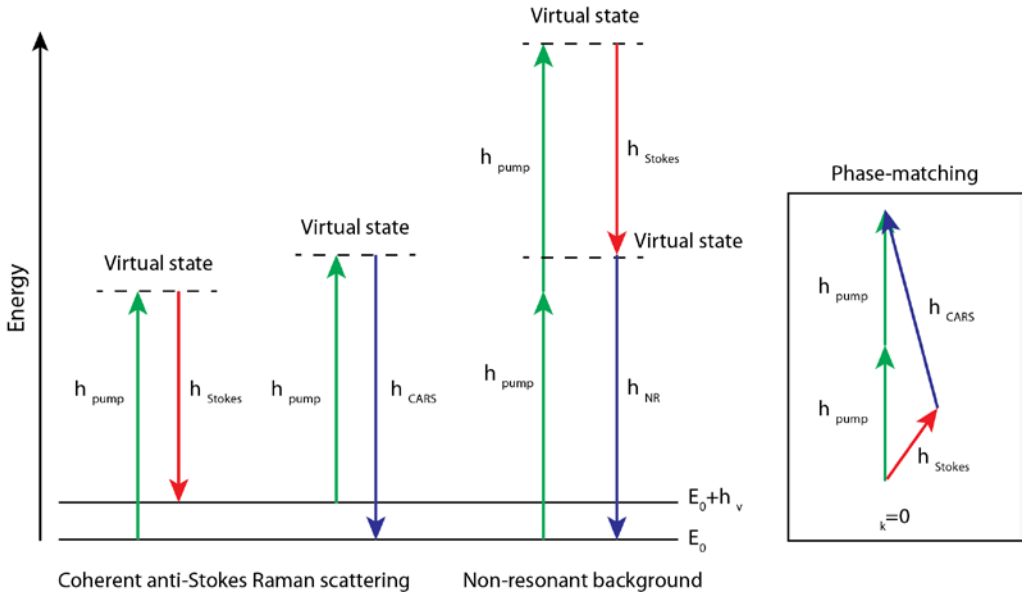

Fig. 3. Energy level diagram showing transitions for CARS and non-resonant background (left); scheme of phase matching between the two pump, Stokes and CARS photons (right).

only one direction of $\boldsymbol{k}_{aS}$ vector of the anti-Stokes photon. That means that all the CARS photons are directed in a single direction different from the one the laser radiation is propagating in. This makes CARS signal easy to record. In

addition, intensity of the recorded anti-Stokes Raman scattering signal is proportional to the square of the number of the oscillators. For this reason CARS has an advantage of high sensitivity as well as faster image acquisition rates over spontaneous Raman scattering. Furthermore, recording signal in the anti-Stokes spectral region means that one-photon fluorescence background generated by colorful samples and impurities is not recorded which is extremely important when biological samples are analyzed [82]. On the other hand, together with the resonant CARS signal, frequency independent non-resonant background is generated. It is attributed to electronic transitions between virtual states in non-resonant molecules (Fig. 3). The overall CARS signal is then described by contributions of both resonant and non-resonant contributions of third-order susceptibility (χ^3_R and χ^3_{NR} respectively) [83]:

$$I_{CARS}(\omega) \propto (|\chi_R^3(\omega)|^2 + |\chi_{NR}^3|^2 + 2\chi_{NR}^3 \mathrm{Re}[\chi_R^3(\omega)]) \cdot I_{pump}^2 \cdot \cdot I_{Stokes}, \quad (3)$$

where, I_{CARS}, I_{pump} and I_{Stokes} – intensities of the CARS, pump and Stokes beams respectively. The contribution of the non-resonant background (I) distorts shapes of the CARS spectral bands as compared to the bands in the spontaneous Raman scattering spectra and (II) overwhelms the resonant CARS signal causing lower contrast in the CARS images [83]. There are CARS detection schemes, such as epi-CARS [84], polarization CARS [85], frequency modulated CARS [86], interferometric CARS [87], that allows avoiding the undesirable non-resonant background in the images. In the epi-CARS technique, the resonant CARS signal is recorded in the backward direction while the non-resonant background is only generated in the forward direction [84,88].

In the CARS microscopy experiment (simplified experiment scheme is presented in Figure 4), phase matching condition between the lasers is achieved by fine tuning a delay line. The radiation is directed onto the sample

and scattered radiation is collected with an optical microscope equipped with non-descanned detectors. Signal can be recorded in either trans- or epi-directions depending on the nature of the sample. Finally, the non-linearity of

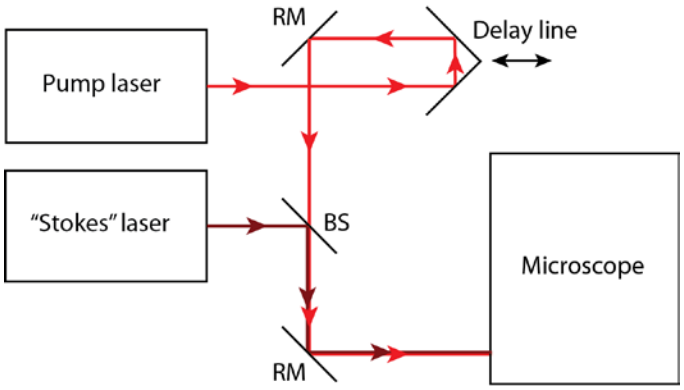

Fig. 4. Block scheme of CARS imaging system.

the CARS process determines that the coherent scattering signal is only generated in a small volume where the lasers are focused and the phase matching condition is met. For this reason, 3D imaging of samples is possible with this method [82].

CARS is a technique mostly used for label-free imaging of various biological systems and offering biochemical specificity with submicron spatial resolution [89–91]. Possibility of simultaneous acquisition of other non-linear optical signals enables multimodal imaging: CARS, two-photon excited fluorescence (TPEF) and second harmonic generation (SHG) signals [82]. While CARS is generated by specific molecular vibrations, TPEF is generated by endogenous fluorophores (such as pigments). SHG signal is generated by non-centrosymmetric microstructures lacking inversion symmetry. Thus, multimodal imaging allows distinguishing different chemical species and their morphological distribution in the sample. In addition, it has been shown that in vivo measurements are possible by utilizing single mode optical fibers for so called CARS endoscopy [92,93].

Multimodal CARS microscopy proved to be of particular use for imaging lipid-rich structures such as brain and kidney tissues [94,95].

However, its potential in imaging and analysis of mineral samples has also been shown [96]. While trans- detection is preferable for thin samples due to more intensive signal acquired, epi- detection is also possible and allows analysis of samples independent of their thickness. It has been recently demonstrated that epi-detected multimodal imaging can be used to uncover distributions of mineral (apatite) and organic matter in tooth which provides better understanding of its morphological structures in micro scale and facilitate optical diagnosis and tooth characterization in dentistry [97].

1.3. Data analysis techniques

1.3.1. Spectral pre-processing

First step in spectral data analysis is pre-processing which allows correcting artefacts related to signal acquisition (e.g., scattering, influence from atmospheric gases, uneven sample thickness, etc.) [23,24,98]. It usually includes atmospheric compensation (physical models are used to estimate and account for the amount of CO_2 and H_2O influencing the spectra), baseline correction (which can be a simple offset correction or scattering correction; rubber-band method is used to correct more complex baseline deviations) and normalization. Sometimes, spectral smoothing may be required to obtain higher signal-to-noise ratio. However, this comes with a price of lowered spectral resolution [31]. Another technique for spectral de-noising is use of principal component analysis (PCA) [99]. Spectra are decomposed into principal components (PCs) and then reconstructed from only few of them leaving the ones that represent the noise out.

Better separation of overlapped spectral bands is achieved by calculating derivatives of spectra or by applying Fourier self-deconvolution algorithm [31,100]. The latter includes altering the decay function of the recorded signal which results in narrower spectral bands. Differentiation produces narrower lineshapes of spectral bands as well. While odd derivatives have dispersive lineshape, even derivatives result in symmetric lineshape. Of note, derivatives of order higher than two are rarely used as their lineshape is complex and may lead to incorrect interpretation of spectra.

1.3.2. Qualitative and quantitative spectral analysis

After spectral pre-processing, further analysis can be performed. Qualitative analysis is usually performed by comparing vibrational spectra of

samples with vibrational spectra of pure components. There are several free-access spectral libraries (for example, http://webbook.nist.gov/; http://rruff.info/) which contain vibrational spectra of various molecular compounds and which can be used for determination of chemical composition of samples. Otherwise, such libraries can be purchased or constructed according to the samples analyzed in a laboratory. Of note, it is usually preferred that both the sample and the library spectrum would be recorded using the same method (e.g., IR transmission or ATR) and under similar environmental conditions.

Absorbance is directly proportional to concentration of absorbing matter. As long as this relationship is linear, quantitative information (relative concentration) about the substances in the sample can be extracted by calculating integral intensities of characteristic spectral bands and dividing them by corresponding integral intensities of spectral bands in the reference spectrum of pure component.

When the spectral data set is very large, it is difficult, and often unnecessary, to analyze spectra one by one. Multivariate analysis methods allow separating the large data set into groups according to the differences between the spectra (i.e., chemical changes in the sample(s)) [101]. One of such methods is hierarchical cluster analysis (HCA) which forms clusters that are organized as tree – the root of the tree contains the whole data set, while the leaves are individual spectra. The results of the HCA are often displayed as a tree-like graph – a dendrogram. In the HCA, the clustering begins with the single spectra which are successively merged into groups according to their similarity. The similarity is usually determined by calculating Euclidean distances between every point in the spectra; then a specific algorithm (usually Ward's algorithm) is used for the grouping [102]. The procedure is repeated until only one cluster remains. Such approach has been used for classification of cells, tissue types, microorganisms, plants etc. [103,104].

1.3.3. Chemical imaging

IR and Raman microscopy allows obtaining morphochemical information about samples which means that not only chemical composition is known, but also where in the sample a specific chemical component is located. A spectral data set obtained by imaging or mapping is pre-processed as described above. Calculation of integral intensities of characteristic spectral bands or use of the HCA (or other multivariate analysis techniques) generates a single value - the integral intensity or cluster number - associated with each spectrum in the data set. In order to create a chemical image, these values are color-coded and attributed to each pixel in the image [23].

1.3.4. Basic theory of Kramers-Kronig transform (KKT)

As mentioned above, in the external reflectance measurements, the spectral band shapes are affected by the dispersion of refractive index (*n*) [27]:

$$n^2 = 1 + \frac{N(q^2/m)}{2\varepsilon_0(\omega_0{}^2 - \omega^2 + i\gamma\omega)}, \qquad (4)$$

here ω – incident radiation frequency, ω_0 – natural resonant frequency of the oscillators in the sample, γ –damping coefficient, q – charge, associated with the oscillator, m – oscillator mass, N – number of oscillators. The dispersion affected spectral bands, or Reststrahlen bands, appear as first derivative of absorbance spectral bands: they acquire negative values at the high frequency side and their peak position is red shifted. Such distortion aggravates spectral analysis and, therefore, needs to be corrected.

Dispersion is normal when $0<\omega<\omega_0$ and $\omega_0<\omega<\infty$. In the range of normal dispersion, the refractive index is real, i.e., $|\ \omega_0{}^2 - \omega^2\ | >> i\gamma\omega$. When $\omega=\omega_0$, i.e., in the spectral range of absorption, the refractive index becomes complex [27]:

$$n' = n + ik\,, \tag{5}$$

here *k* describes the absorption and relates with the absorption coefficient (α) as follows [27]: $\alpha = \frac{4\pi k}{\lambda}$. Then, the dispersion relation for the real and the complex parts of the refractive index becomes [27]:

$$n = 1 + \left(\frac{Nq^2}{\varepsilon_0 m}\right)\frac{\frac{1}{2}\left({\omega_0}^2 - \omega^2\right)}{({\omega_0}^2 - \omega^2)^2 + \gamma^2\omega^2}\,, \tag{6}$$

$$k = \left(\frac{Nq^2}{\varepsilon_0 m}\right)\frac{-\frac{1}{2}\gamma\omega}{({\omega_0}^2 - \omega^2)^2 + \gamma^2\omega^2}\,. \tag{7}$$

Dispersion is anomalous when the refractive index is decreasing when the frequency is increasing (in the spectral range around $\omega=\omega_0$). The real and the complex parts of the refractive index are related through the Kramers-Kronig transform [27]:

$$n(\nu_0) = n(\infty) + \frac{2}{\pi}P\int_0^\infty \frac{\nu k(\nu)}{\nu^2 - {\nu_0}^2}\,\mathrm{d}\nu\,, \tag{8}$$

$$k(\nu_0) = -\frac{2\nu_0}{\pi}P\int_0^\infty \frac{n(\nu) - n(\infty)}{\nu^2 - {\nu_0}^2}\,\mathrm{d}\nu\,. \tag{9}$$

Here $n(\infty)$ – asymptotic value of the refractive index when frequency is approaching infinity, $\nu = \omega/2\pi$ and the *P* denotes Cauchy principal value which allows calculating the value of the integral at $\nu = \nu_0$ [105]:

$$P\int_0^\infty \frac{F(\nu)}{\nu - \nu_0}\,\mathrm{d}\nu = \lim_{r\to 0}\left(\int_0^{\omega_0 - r}\frac{F(\nu)}{\nu - \nu_0}\,\mathrm{d}\nu + \int_{\omega_0 + r}^\infty \frac{F(\nu)}{\nu - \nu_0}\,\mathrm{d}\nu\right), \tag{10}$$

here *F(ω)* is a complex function.

When analyzing the external reflectance, Kramers-Kronig relations are used to calculate the phase change between the incident (*r*) and the reflected (*r'*) radiation. It is known from the Fresnel equations that for an absorbing material, the amplitude of the reflected unpolarised radiation [27]:

$$r' = |r| \exp[i\delta] = \sqrt{R(\nu)} \exp[i\delta] = \frac{n_2 + ik - 1}{n_2 + ik + 1}, \quad (11)$$

here δ is the phase change ($-\pi \leq \delta \leq \pi$), $R(\nu)$ - reflectivity; the incidence is from air (refractive index n_1=1) and normal (angle of incidence ϑ=0^0). It can be then shown that [27]:

$$n_2 = \frac{1 - R}{1 + R - 2\sqrt{R}\cos\delta}, \quad (12)$$

$$k = \frac{-2\sqrt{R}\sin\delta}{1 + R - 2\sqrt{R}\cos\delta}. \quad (13)$$

The phase change δ can be calculated through the Kramers-Kronig relations as follows [27]:

$$\delta(\nu_0) = -\frac{2\nu_0}{\pi} P \int_0^\infty \frac{\ln\sqrt{R(\nu)}}{\nu^2 - \nu_0^2} \mathrm{d}\nu. \quad (14)$$

Having subsequently calculated the k, optical density is [27]:

$$D(\nu) = 2\pi k(\nu)\tilde{\nu} l, \quad (15)$$

here *l* is penetration depth.

Reliable analysis of specular reflectance spectra cannot be accomplished without performing the KKT. However, real life sample rarely yield ideal specular reflectance. Typically, many phenomena (such as scattering, diffuse reflectance, reflectance from back surfaces, etc.) influence the spectra [106]. In addition, the prerequisite to have an angle of incidence equal to 0^0 in order to obtain the Equation 11 is not satisfied in the Cassegranian optics used in the IR microscopes. For these reasons, use of the KKT has been episodic. Appropriate use of the KKT for pre-processing reflectance spectra of rough-surfaced samples – urinary stones – and obtaining reliable information about their morphochemistry is within the scope of this thesis and will be discussed in chapter 2.

Chapter 2 Vibrational spectroscopy analysis of urinary stones

2.1. Urinary stone disease

Urinary stone disease (urolithiasis) is a life-style related non-communicable disorder. Despite the fact that recent study in England showed a decrease in prevalence rates of urolithiasis [107], global literature still reports increasing numbers of patients with kidney stones [108–110]. A variety and complexity of processes influencing stone formation prevents from tracing a single explanation of etiology and pathogenesis of the disease which, in turn, causes lack of appropriate prevention measures [111–113]. The fact is confirmed by increasingly high recurrence rates of urolithiasis. As some studies have shown, 30% to 40% of untreated patients will form a new stone in 5 years' time [112,114,115]. This has a significant impact on a quality of life. Furthermore, the prevalence and incidence of kidney stone disease has been increasing across the world throughout the 20th century. For example, in the US the prevalence of the disease is approximately 10 % (13 % for men and 7 % for women) which is a drastic increase from 3 % recorded in the 1964-1972 time period [112]. Developed, industrialized European countries follow similar trends and urolithiasis is becoming a major health care problem worldwide.

2.1.1. Formation of urinary stones: crystallization, aggregation and growth

Urinary stones are mainly composed from calcium containing minerals: calcium oxalates (whewellite ($CaC_2O_4 \cdot H_2O$) or calcium oxalate monohydrate (COM) and weddelitte ($CaC_2O_4 \cdot 2H_2O$) or calcium oxalate dihydrate (COD)) and calcium phosphates (apatites ($Ca_5(PO_4)_3(F,Cl,OH)$) and brushite ($CaHPO_4 \cdot 2H_2O$)). These minerals account for approximately 80% of all cases. Ten percent of the stones are constituted from struvite ($NH_4MgPO_4 \cdot 6H_2O$, a mineral originating from infection by bacteria that

possess enzyme urease), 9% - from uric acid ($C_5H_4N_4O_3$) and the remainder 1% - from other substances such as cystine ($C_6H_{12}N_2O_4S_2$), ammonium acid urate ($C_5H_7N_5O_3$), drugs, etc. [116]. These rates vary according to geography, sex and age [117].

An essential condition for the stone formation is oversaturation of urine. It can be caused by some pathological conditions as well as dietary habits of the patient. For instance, increased calcium oxalate oversaturation may result from low urine volume or excessive excretion of calcium or oxalate, or combination of these factors [116]. The oversaturation may constantly vary in time and/or include several different components resulting in multi-component stones. For the urine to be oversaturated with the rare components, such as struvite, cystine or drugs, specific conditions are required, whereas, oversaturation with calcium oxalate, phosphates and uric acid can occur even in urine of healthy people. In these people, the development of the stones might be prevented by crystallization inhibitors, lack of crystallization centers or simply because the process is energetically disadvantageous [118]. Thus, the oversaturation is essential but insufficient condition to the stone formation.

There are three most important processes of urinary stone formation: nucleation, growth and aggregation. During the stage of nucleation, small crystals – crystallization centers – form. The nucleation can be divided into primary if new crystals form in the oversaturated solution and secondary if the nuclei form on the surface of pre-existing crystals. In turn, the primary nucleation can be further subdivided into homogeneous, when crystals are formed spontaneously in the volume of the solution, and heterogeneous, when crystals form on a surface. The latter form of nucleation is the most probable in urinary system [118].

During the stage of crystal growth molecules and ions in the urine are transported into vicinity of the pre-formed nuclei and incorporated into

their lattice. The aggregation of the formed crystals is a process of them clumping together during their constant collisions [118].

It is obvious that prohibiting the oversaturation of urine will, in turn, prevent the crystallization. External prohibitors and inhibitors, such as various urinary macromolecules affect the crystallization processes as well: they can either prevent or induce nucleation, crystallization and/or aggregation. For instance, albumin adsorbed on hydroxyapatite may induce nucleation of calcium oxalate [118].

The above described processes determine chemical composition, texture (shape and arrangement of crystal grains in the stone) and morphology of urinary stones. Accordingly, the stones have been classified into 7 main types and 22 subtypes [117], each relating to some specific pathology. Therefore, analysis of stones texture and morphology as well as determination of their chemical composition is of great importance for treatment and prevention of urolithiasis. In the multicomponent stones, an arrangement of areas of different chemical compositions could be a hint to the history of stones growth.

2.1.2. Urinary stone analysis

Comprehensive analysis of urinary stones is important for effective treatment and prevention of urolithiasis, especially in cases of residual and recurrent stones. Large number of various physical and chemical methods has been used for the analysis [119]. They are summarized in Table 2 [26,117,120–130]. None of the methods alone can provide full information about the morphology, texture, chemical and mineralogical composition of the stones. For instance, texture can only be determined by techniques such as scanning electron microscopy or polarization microscopy. While chemical methods provide information about atomic and molecular content of the stones, ability to determine their exact mineralogical composition is limited.

Table 2. Physical and chemical methods used for analysis of urinary stones and the information they provide [26,117,120–130].

Methods	Information extracted			
	Morphology/ structure/ texture	Chemical composition		Mineralogical composition
		Elemental composition	Non-crystal/organic components	
Optical microscopy (stereomicroscopy)	x			
Chemical analysis		x	x	x*
Thermal gravimetry			x*	x*
X-ray diffraction spectroscopy				x
Laser induced breakdown spectroscopy (LIBS)		x		x
Scanning electron microscopy	x			x*
Computer tomography	x			x
FT-IR (micro)spectroscopy/Raman spectroscopy	x*		x	x
Polarization microscopy	x			x

*only limited information can be obtained

Furthermore, in choosing a method for the urinary stone analysis one has to pay attention to its availability and price.

Recently, three methods became the most popular for the stone analysis: polarization microscopy, X-ray diffraction spectroscopy and IR absorption spectroscopy [119]. These methods are discussed below in more detail.

Polarization microscopy is a method based on interaction of polarized light with crystals. Depending of the crystalline structure of the analyzed material as many as 20 different properties such as color, shape, refraction or birefringence can be observed. In addition to the low cost and

rapidity, polarized microscopy has an advantage of capability to identify structures as small as 5 μm. However, experienced and skilled scientists are required to perform subjective analysis. Furthermore, while differentiation of COM from COD is relatively simple, some crystals such as calcium phosphates are difficult to identify [119,131]. Therefore, polarized microscopy is not used as a standalone technique for the urinary stone analysis, but rather as a complement to other methods [113,123].

X-ray diffraction spectroscopy is based on X-ray diffraction on crystal lattice. The diffraction pattern corresponds to reciprocal lattice of the crystal and is described by Bragg's equation:

$$2d \sin\Theta = m\lambda, \qquad (22)$$

here d is the distance between crystal planes, Θ – diffraction angle, m – positive integer, λ – wavelength. Powdered urinary stone samples are usually analyzed with this method [122]. Although the method provides precise quantitative information about crystalline composition of urinary stones, amorphous components cannot be detected. An important advantage of X-ray diffraction spectroscopy is that the analysis can be automated [131]. However, high price and long measurement time prevents this method from being used routinely.

For a more detailed analysis of urinary stones, synchrotron radiation based X-ray microtomography (SR-μCT) has been applied [132]. The method allowed determining texture, chemical composition and microstructure of urinary stones while keeping them intact. While this technique could not be used routinely, it allows reconstructing formation path of selected stones. It has been particularly useful for identification and characterization of Randall's plaques – subepithelial calcifications constituted from calcium apatite – which are known to be initial growth centers of the stones [133–136].

Dual energy CT has also been used to detect and characterize the urinary stones *in vivo* [126]. The types of the stones can be precisely determined by using this technique (except for the stones constituted from mixtures of uric acid and hydroxyapatite). However, this technique is still to be validated and its clinical impact determined.

Vibrational spectroscopy, infrared absorption spectroscopy in particular, has become one of the most popular methods for urinary stone analysis due to its availability, rapid and precise identification of constituents, possible automation and low costs [119]. Since application of vibrational spectroscopy methods for urinary stone analysis is within the scope of this thesis, they will be described in more detail in the next chapter.

2.2. Vibrational spectroscopy applications to urinary stone analysis

2.2.1. IR absorption spectroscopy of urinary stones

Infrared absorption spectroscopy has become one of the most popular methods for urinary stone analysis due to its availability, rapid and precise identification of constituents, possible automation and low costs [119]. It has been used both as a stand-alone method [137–139] and as a complementary technique to X-ray spectroscopy, thermogravimetry, SEM, etc. [127,128,140]. The method has been shown to provide reliable information about chemical composition of both crystalline and amorphous constituents of the stones. Crystalline phases, such as COM and COD, can be distinguished. Moreover, in frequent cases of multicomponent stones quantitative analysis can be performed. However, a rather time consuming sample preparation for transmission measurements has prevented the method from becoming routine.

To solve the problem of complex sample preparation, there have been several attempts to apply ATR IR spectroscopy both for qualitative and quantitative analysis of urinary stones [141–143]. In these studies pulverized stone samples are pressed to the ATR element to record IR spectra. Their analysis provides similar or superior qualitative and quantitative information as the spectra recorded using KBr pellet technique. Since less sample preparation is required for the ATR IR spectroscopic method, it has been concluded to be favorable for urinary stone analysis. However, more investment is needed as ATR accessories for IR spectrometers are costly.

Major disadvantage of both KBr pellet and ATR techniques is that the stone is pulverized during sample preparation. For complete description of urinary stone type, full information about its morphology, structure and chemical composition is required [117,144,145]. Infrared spectroscopic imaging (mapping) of cross-sectioned urinary stones is capable of

simultaneously providing information about both their chemical composition and structure. IR spectroscopic imaging studies of rigid biological samples such as bones or calcified inclusions in biological tissues are performed in transmission mode [146]. Thin (less than 10 μm) sections of the samples were obtained by using a microtome. However, this technique is not very well suited for the urinary stones due to their brittleness. Some later studies were devoted to applying reflectance mode of the IR microscope for the imaging of calcium oxalate stones [26,132,147]. The authors of these papers showed that spectral information from specularly reflected infrared light can be used for qualitative analysis with the same success as KBr pellet (transmission) or ATR techniques. However, distortions of spectral bands (Reststrahlen bands) of specular reflectance spectra were neglected in the former studies which may introduce error to the images. The Reststrahlen bands in the specular reflectance spectrum resemble first derivative of the absorption spectrum and they are shifted towards lower wavenumbers. Such distortions can introduce serious errors when integral intensities of the Reststrahlen bands are used for estimation of concentration of some chemical compound in particular spot of the imaged surface. This is particularly true in case of the band overlapping. Contour of the overlapped Reststrahlen bands due to the first derivative feature is complicated and the bands are hardly distinguishable. Intensity of the adjacent bands is also influenced by the first-derivative effect. The prerequisites of having pure specular reflection signal recorded at 0^0 angle of incidence prevents standard Kramers–Kronig transform from being used to correct the spectra.

2.2.2. Raman scattering spectroscopy of urinary stones

Raman scattering spectroscopy is not nearly as much used for the urinary stone analysis as IR absorption spectroscopy. In most of the studies it has been used solely as a complementary technique to the latter [128,148].

The main reason for that is the fluorescence signal from the stones usually obscuring the Raman scattering signal. On the other hand, Raman scattering spectroscopy has several advantages over IR absorption spectroscopy: it does not require any sample preparation to obtain the spectra, there are commercial hand-held Raman scattering spectrometers that can be used for routine analysis, fiber optics could be used for analysis *in vivo* [149]. For this reason, there is now an increasing number of studies that propose Raman scattering spectroscopy as a method of choice for the urinary stone analysis [150,151,129].

Raman scattering microscopy with He-Ne laser excitation (632.8 nm) was used for identification of urinary stone composition from urine powder after the stone was broken by ureteroscopic lithotripsy [150]. The stone samples were photobleached to avoid fluorescence and the main components of the stones could be qualitatively identified. Although reliable quantitative analysis was not feasible due to limited sampling, the method was demonstrated to be useful for immediate stone analysis after their removal procedures.

Similar results were obtained and automated analysis of urinary stones was developed by A. Miernik et al. [151]. In this study, 532 nm and 785 nm excitation were used and the fluorescent background was mathematically removed prior analysis. Both major and minor components could be identified which shows the potential of the technique. In the subsequent paper the author tested the possibility of using a commercial fiber optics used for endoscopic treatment of urolithiasis for urinary stone analysis *in vivo* [149]. Although the results showed that the currently used fibers are unsuitable for such purpose, the study provided useful information for further development of such systems.

2.3. Urinary stone analysis: experimental details

2.3.1. Sample preparation of urinary stones

Urinary stones were obtained from Vilnius University hospital Santariskes clinics Urology Centre (authorization from Vilnius Regional Biomedical Research Ethics Committee for biomedical research No. 158200-5-053-056LP1). Firstly, they were inspected by using optical stereomicroscopy (Stemi 2000C with AxioCam ERcSs video camera, Carl Zeiss, Oberkochen, Germany) and, according to morphological features, pre-assigned to one of the possible types and subtypes [117]. The stones which were intact during their removal procedure were checked for specific features which were then analyzed by recording Raman scattering spectra. No sample preparation was necessary for Raman scattering spectroscopy experiments of urinary stones. Then, the intact stones were cross-sectioned. The direction of the section was chosen according to the stone's morphology. For example, papillary stones with a visible Randall's plaque were sectioned perpendicularly to the plaque. One half of the stone was used to perform IR/Raman/CARS chemical imaging. For the measurements, it was fixed on a glass microscope slide using two-component epoxy and polished gently in order to obtain flat surface. Sand paper of various roughnesses (P220, P240 or P400) and/or polishing glass (originally intended to polish optical windows for infrared spectroscopy) was used for the polishing. After the polishing, the stones we cleaned with acetone using a cotton swab. Unless displaying any exclusive morphological features, both halves of the stone were assumed to have identical chemical composition; thus, the second half was used to perform qualitative and quantitative analysis by means of IR absorption spectroscopy. The samples for the latter were prepared by using KBr (potassium bromide) pellet technique: the stone sample is grinded using an agate mortar and pestle and mixed with

a KBr powder in ratio 1:100 (2 mg:200 mg) and the mixture is pressed into a pellet with a manual hydraulic press (Specac, Orpington, England) under 740 MPa pressure. The stones which were broken during their removal procedure were also checked for the distinct features (which were the analyzed by Raman spectroscopy) and subsequently grounded to prepare the KBr pellets.

Samples for the FIR absorption measurements were prepared by polyethylene (PE) pellet technique: the stone sample is grinded using an agate mortar and pestle and mixed with a PE powder in ratio 1:50 (2 mg:100 mg) and the mixture is then placed into the die of manual hydraulic press (Specac, Orpington, England). The stainless steel parts of the die were pre-heated to approx. 150^0 C. The die with the sample were placed in an oven (pre-heated to approx. 200^0 C) and kept until the temperature of its outer surface reached 150^0 C again. At this point, the inner temperature of the die had reached the melting temperature of the PE (approx. 136^0 C). The die was then placed under the press and the sample pressed into a pellet under 370 MPa pressure.

2.3.2. FTIR absorption spectroscopy of urinary stones

Infrared absorption spectra were recorded by using FTIR spectrometer Vertex 70 (Bruker Optik GmbH, Ettlingen, Germany) equipped with globar light source, KBr beamsplitter and liquid nitrogen cooled MCT detector. The spectra were recorded in 3900-650 cm^{-1} spectral range with spectral resolution of 6 cm^{-1}. For the resultant spectrum, 128 interferograms were averaged and Fourier transformed into a spectrum applying Blackmann-Harris 3 apodization function and zero filling factor 2.

2.3.3. FTIR reflection microspectroscopy of urinary stones

Infrared reflectance spectra were obtained using infrared microscope 'Hyperion 3000' (Bruker Optik GmbH, Ettlingen, Germany) equipped with a single element MCT detector and combined with Vertex 70 spectrometer (Bruker Optik GmbH, Ettlingen, Germany). A 15x/0.4 objective was used. Knife edge aperture was fully open when collecting the spectra. Over 1500 spectra were collected from one stone while mapping the surface of the cross-section by means of motorized micrometer stage. The step size between the scanned points was set to approximately 100 μm (for the rare cases of large stones, the step was increased in order to adjust the measurement time to the working time of the detector (approx. 9 h)). The spectra were recorded in 3500-650 cm^{-1} spectral range with spectral resolution of 6 cm^{-1}. Thirty two interferograms were averaged for one resultant spectrum of each point and the result Fourier transformed into a spectrum applying Blackmann-Harris 3 apodization function and zero filling factor 2.

2.3.4. FIR absorption spectroscopy of urinary stones

FIR absorption spectra were recorded by using FT-IR spectrometer Vertex 70 (Bruker Optik GmbH, Ettlingen, Germany) equipped with globar light source, wide range MIR-FIR beamspliter and DTGS detector. The spectra were recorded in 680-30 cm^{-1} spectral range with spectral resolution of 8 cm^{-1}. For the resultant spectrum, 128 interferograms were averaged and Fourier transformed into a spectrum applying Blackmann-Harris 3 apodization function and zero filling factor 4.

2.3.5. FIR reflection microspectroscopy of urinary stones

FIR microspectroscopy experiments were carried out at the MAX-IV laboratory in Lund, Sweden. Sets of reflectance spectra for the chemical

imaging in the FIR spectral region were obtained using FTIR microscope 'Hyperion 3000' (Bruker Optik GmbH, Ettlingen, Germany) connected to the IFS 66v FT-IR spectrometer equipped with multi-layer Mylar 6 µm beamsplitter. Synchrotron radiation was used for the FIR microspectroscopy experiments. A general Purpose 4.2K Si Bolometer System (Infrared Laboratories, Tucson, USA) was used to record the spectra. The microscope is equipped with plastic chamber purged with nitrogen gas to avoid the influence of atmospheric water absorptions to the spectra. The mapping parameters were selected the same as for the MIR microscopy measurements. The spectral acquisition parameters were as follows: the spectra were recorded in 700 – 150 cm^{-1} spectral range, 128 interferograms were averaged and the result was Fourier transformed into a spectrum applying Blackman-Harris 3-Term apodization function and zero filling factor of 4. Spectra were recorded with 8 cm^{-1} spectral resolution. It took approximately 14 hours to perform the mapping in the FIR spectral region (the time varies depending on the size of the stone, i.e., on the number of measurement points).

2.3.6. Raman scattering spectroscopy of urinary stones

The Raman spectra were recorded with FT-Raman spectrometer 'MultiRAM' (Bruker Optik GmbH, Ettlingen, Germany) equipped with Nd:YAG laser source (λ=1064 nm, P_{max}=1 W) and liquid nitrogen cooled Ge (germanium) diode detector Gold plated mirror objective (focal length – 33 mm) was used. Diameter of the laser beam at its focal point is 100 µm. For the mapping of the stones, the parameters were selected the same as for the MIR microscopy measurements. To obtain each Raman spectrum, 128 interferograms were averaged and the result was Fourier transformed by applying Blackman-Harris 3-Term apodization function and zero filling factor of 2. The 4 cm^{-1} spectral resolution was used. Laser power was adjusted

according each sample to avoid burning. The time needed to perform Raman imaging is approximately 40 hours. For this reason, images of few stones were only used as reference for FTIR imaging results.

2.3.7. Nonlinear optical microscopy of urinary stones

Nonlinear optical microspectroscopy experiments were carried out in Dresden University of Technology, Dresden, Germany. Two erbium fiber laser sources were used for the nonlinear optical imaging. They were spatially and temporally overlapped by using a dichroic beam combiner and a delay line, respectively. The "pump" laser (Femto Fiber pro NIR from Toptica Photonics AG, Gräfelfing, Germany) emits NIR radiation at 781.5 nm with pulse duration of 1.2 ps and maximum power of 100 mW. The "Stokes" laser (Femto Fiber pro TNIR, also from Toptica Photonics AG) which is tunable and has pulse duration of 0.8 ps was set to 1005 nm or 857 nm resonantly addressing the symmetric stretching vibration of methylene at 2850 cm^{-1} or mixed C-O, C-N, C-C vibrations of uric acid at 1121 cm^{-1}, respectively. The emitted power is 1.5 mW at 1005 nm and 12 mW at 857 nm. Multiphoton images were acquired by an upright microscope Axio Examiner Z.1 equipped with scanning module LSM 7 (all from Carl Zeiss AG, Jena, Germany) and non-descanned detectors. The nonlinear signals were acquired in reflection mode using band-pass filters. A band-pass filter with band 633-647 nm was used to select the CARS signal corresponding to the Raman band at 2850 cm^{-1}, and one with band 670-754 nm was used for acquisition of the CARS signal corresponding to the Raman band at 1121 cm^{-1}. A band-pass filter with band 381-399 nm was used to acquire SHG. Green TPEF was acquired in the range 500 – 550 nm. A W Plan – Apochromat water immersion objective of 20x and NA=1.0 was used. The laser power in the focus is 50% of the nominal laser power. Tile scan mode was used for acquisition of large images. Z stacks

followed by a maximum intensity projection were used to compensate for lack of planarity of sample surface.

2.3.8. Spectral analysis of urinary stones

Assignment of the recorded IR absorption spectra was performed by comparing them with reference spectra of pure components (COM (*Fluka*), uric acid (*Fluka*), hydroxyapatite (*Sigma Aldrich*) and l-cystine (*Sigma Aldrich*)). The reference spectra were obtained by using the same experimental conditions as spectra of the urinary stone samples. Reference spectra of struvite, fluorapatite, COD and other rare components were obtained from online spectral libraries [152,153].

When possible, relative concentrations urinary stones' constituents were determined by calculating integral intensities of characteristic spectral bands and dividing them by corresponding integral intensities of spectral bands in the reference spectra of synthetic components.

The KKT of the reflectance spectra of urinary stones was performed using MATLAB package (Version 7.9, The MathWorks, Inc., USA). When performing the KKT of spectra, an offset was added to all the intensity values if necessary. This is reasoned by the fact that if the reflectance is close to zero, due to the $\ln\sqrt{R(\nu)}$ term in the Equation 14, the integral becomes singular [27]. The spectra which were collected beyond the borders of the stone's surface and which carry no information about the sample were not corrected. Subsequently to the KKT, baseline correction (rubber-band method) was applied to the spectra.

The prerequisite to obtain the Equation 11 is for the angle of incidence to be 0^0. The IR microscope objective used in this work yields a solid angle of incidence of approximately 23^0. However, the use of the Kramers-Kronig relations is still valid for the urinary stone samples which have refractive index Re(*n*) that varies between 1.2-1.6 and extinction coefficient

Im(*n*) that varies between 0.01-0.3. For these values, reflectance of non-polarized radiation remain nearly constant in the angle range between $0 – 30^0$ [154].

2.3.9. IR and Raman chemical imaging of urinary stones

IR and Raman chemical images of urinary stones were obtained by calculating integral intensity of spectral band, characteristic to a chemical component of interest. A specific color was then assigned according to the numerical value of the integral intensity. The procedure is repeated for all the spectra of the cross-section and a map, representing the distribution of integral intensities across the surface, is constructed. The procedure was performed using MATLAB package (Version 7.9, The MathWorks, Inc., USA).

The chemical images were also obtained by using HCA. It was applied to the vector normalized reflectance spectra in the 1800-650 cm^{-1} spectral region ("fingerprint" region). Euclidean distances between the spectra were calculated, and then Ward's algorithm was used to group the data. The number of clusters was selected in advance according to the *a priori* knowledge about chemical composition of the stone acquired from the transmission measurements. In some cases, the analysis of the reflectance spectra allowed identifying additional components in the stone, not predicted by the transmission measurements due to their minor amounts. The number of classes for the HCA was then varied accordingly. Each cluster was assigned with some specific color and chemical maps were formed. The HCA analysis was performed and corresponding chemical maps were constructed using OPUS software (Bruker Optik GmbH, Ettlingen, Germany).

2.4. Urinary stone analysis: results and discussion

Comprehensive analysis of urinary stones is important for effective treatment and prevention of urolithiasis, especially in cases of residual and recurrent stones. For this reason, in this work we applied and evaluated potential of various vibrational spectroscopy methods (IR (microspectroscopy in MIR and FIR spectral regions, Raman scattering spectroscopy and multimodal CARS microscopy imaging) for morphochemical analysis of human urinary stones.

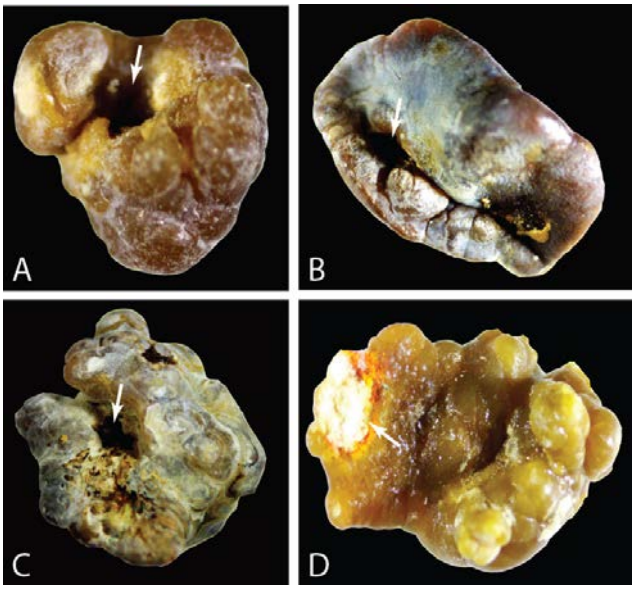

Fig. 5. Typical pappilary urinary stones constituted from COM.

Urinary stones were firstly analyzed by optical stereomicroscopy. The stones were classified according to their morphology and subsequent analysis routine was ascribed. The stones obtained in this work were either intact (single or multiple stones) or broken during their removal procedure. Morphology of the intact stones provides information about whether the stone grew attached or loose in the urinary system. Signs of papillary umbilication possibly hosting a Randall‘s plaque suggest the former while uniform smooth surface – the latter. In Figure 5 A-C, typical papillary COM

stones are presented. The apatite plugs are, however, missing from the surface dip (marked by arrows). In the Figure 5 D, the apatite deposition (marked by arrow) is visible on the tip of the COM stone with depressed surface typical to papillary stones. The reddish layer around the deposit is bilirubin.

Fig. 6. Urinary stones with smooth surface constituted from (A) uric acid and COM, (B, C).

The stones in Figure 6 have smooth and glossy surface with color varying according to their chemical composition: yellow to orange is typical to uric acid while beige to dark brown – to COM. The smooth and glossy surface is a result of rubbing between multiple stones confined in the same anatomical site in urinary tract [117].

Information about latest stages of urinary stones' growth can be obtained by analyzing distinct features on their surface (such as shown in Figure 7 and Figure 8) by Raman scattering spectroscopy. For this, laser radiation was directed to the selected ROI and the scattering signal was recorded. The white sharp crystals on the surface of the stones presented in Figure 7, were identified as COD by Raman scattering spectroscopy (Fig. 7 D). Presence of such crystals suggests that the stones were in a phase of active formation before their removal from the patients' organisms [145,155]. Small translucent crystals on the surface of another COM stone (Fig. 8) were determined to be sucrose. It has been shown that increased amounts of sucrose in human organism can increase calcium concentration which in turn causes stone formation [116]. The whitish surface of this stone also suggests recent depositions of COM [117]. In the latter case, the use of Raman

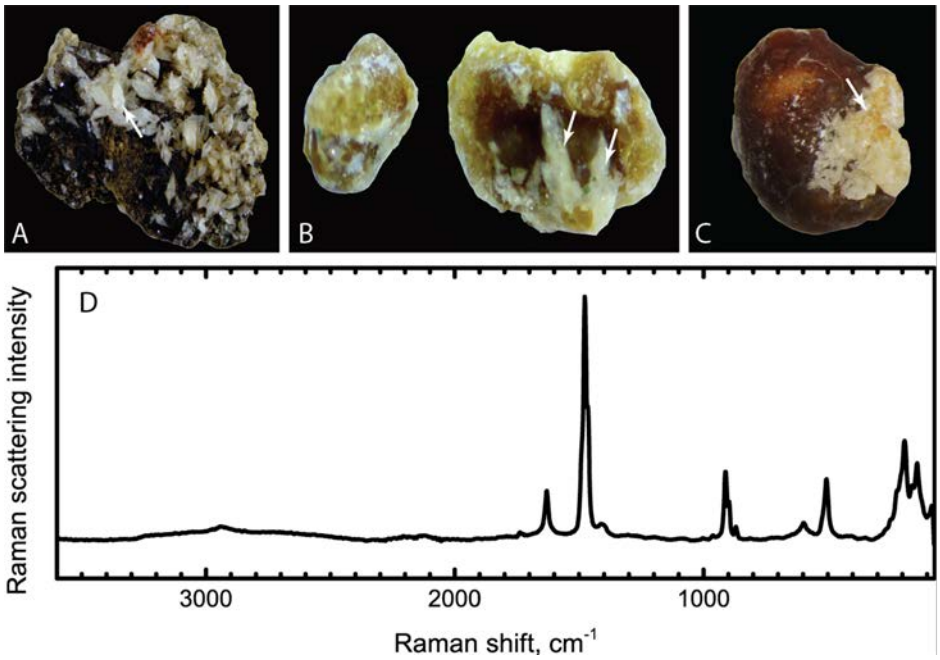

Fig. 7. Urinary stones constituted from COM and sharp crystals of COD deposited on their surface (marked by arrows). Raman scattering spectrum of COD in D was recorded from the area marked by arrow in C.

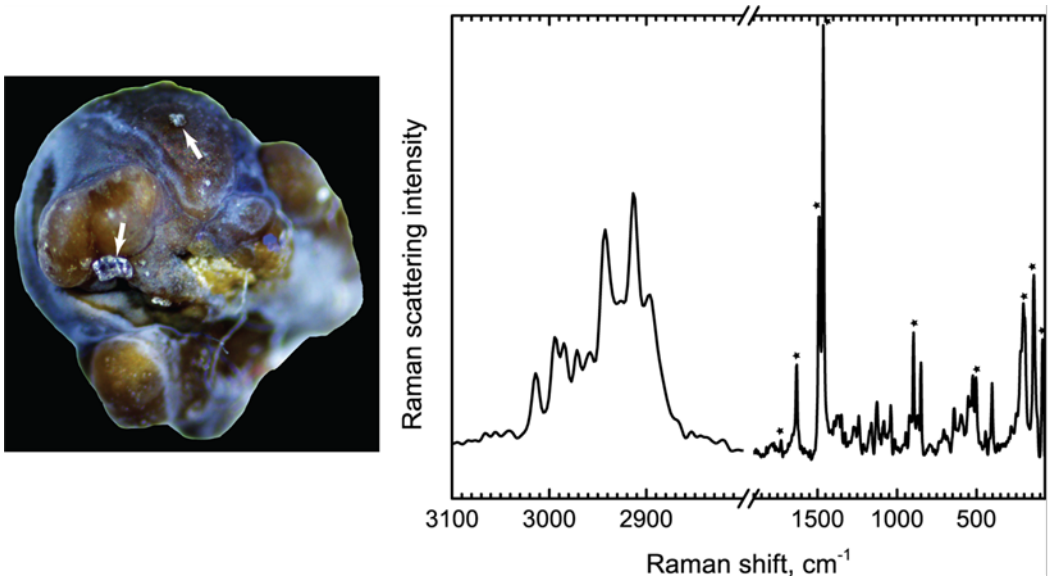

Fig. 8. Urinary stone constituted from COM; on its surface, small crystals of sucrose are visible (marked by arrows). In the Raman scattering spectrum of the crystals (on the right) both spectral bands of sucrose and COM are visible; the latter are marked by asterisk.

spectroscopy subsequent to the visual investigation is fundamental. If the stone was ground, the small amounts of sucrose could not be detected as the absorption of COM would be overwhelming.

Most of the information that can be extracted from inspecting morphology of urinary stones is lost when they are broken during their removal procedure. However, they can still be attributed to a certain type according to their color and other features such as packing of crystals. Figure 9 A and B shows two types of COM stones. The stone in A is lighter brown and has an unorganized crystal structure as compared to the stone in B. Differences in color and crystal organization is suggestive of the environment the stone was growing in, growth rate and, most importantly, underlying disorders [117,145]. Therefore, morphological examination of urinary stones is of great importance not only for planning further course of study but for predicting diagnosis as well. Uric acid stone of yellow-orange color is presented in Figure 9 C. Debris of the broken stones may still contain some distinct features that can be separately analyzed by Raman scattering spectroscopy. For instance, a clot of blood could be identified in the COM stone presented in Figure 9 D (marked by arrow). Since minerals constituting urinary stones typically have strong absorbance, even larger amounts of organic substances (such as blood) may remain unidentified if the stone is ground. Thus, the use of Raman scattering spectroscopy is of great

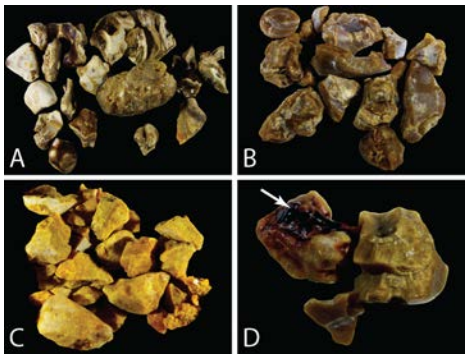

Fig. 9. Urinary stones that were broken during their removal procedure. The stones are constituted from: (A, B and D) COM, (C) uric acid.

importance for identification of all constituents of both intact and broken urinary stones.

The visually inspected urinary stones were further investigated by FTIR absorption spectroscopy. One half of the intact stones or whole broken stones were analyzed. The results of the 403 stones analysis are presented in Figure 10. The graph summarizes prevalence of different types of urinary stones in Lithuania. Calcium oxalate stones include all stones the major constituent of which is COM, COD or their mixture. Minor amounts of phosphates – various apatites or amorphous calcium phosphates (ACP) – might be present in these stones as well. In accordance with the literature results [156], it can be seen that calcium oxalate urinary stones are the most common type of stones with prevalence value of 61 %. However, this percentage is lower as compared to the 70-80 % observed in countries such as USA or Germany [156–158]. Major component in uric acid stones is uric acid,

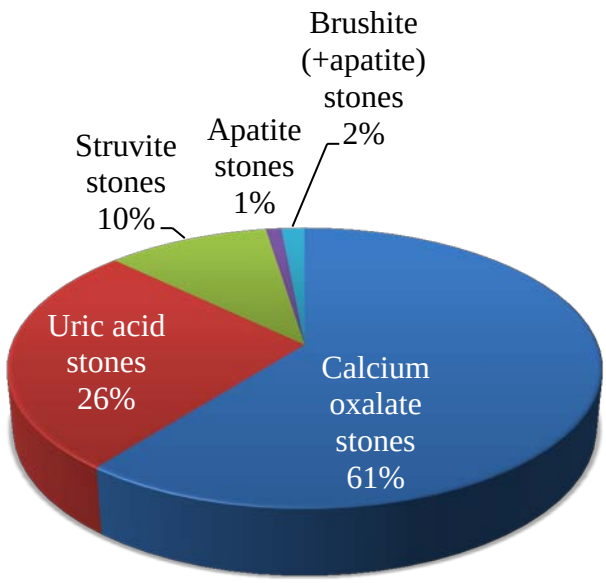

Fig. 10. Chemical composition of human urinary stones as determined by means of IR absorption spectroscopy of 403 stone samples; the graph represents prevalence of calcium oxalate, uric acid, struvite, apatite and brushite stones in Lithuania.

possibly with COM or other minerals as minor constituents. They are less common and comprise 26 % of all urinary stones. This percentage is unexpectedly high as compared to the literature values of 10-15 %. The prevalence of struvite (10 %), brushite (2 %) and apatite (1 %) stones are in accordance with the literature [156].

In many cases minor components remain unidentified by FTIR absorption spectroscopy unless they are mechanically separated from the major components during the visual investigation. This is particularly true for uric acid stones mixed with minor amounts of other components since uric acid has strong absorbance and many spectral bands in the MIR spectral region. Therefore, we expanded the spectral region used for analysis to FIR. Spectral bands in the FIR spectral region provide information about low frequency vibrations of heavy atoms as well as phonon modes of crystal lattices [159].

The recorded FIR absorption spectra of COM, COD, uric acid, hydroxyapatite, struvite, ACP and brushite are presented in Figure 11. Characteristic spectral bands can be observed for all crystalline minerals. Some of them (marked by arrows) could be assigned to characteristic molecular vibrations according to the literature [160–166]. Most bands below 400 cm^{-1}, however, remain unassigned. In crystals, spectral bands of lattice vibrations are found in this spectral region.

In the FIR spectral region, two hydration states of calcium oxalate – COM and COD – can be discriminated from each other by spectral bands at 395 cm^{-1} and 152 cm^{-1} observed in the COD spectrum. On the other hand, struvite and ACP have very similar spectral bands; thus it is difficult to differentiate between the two components.

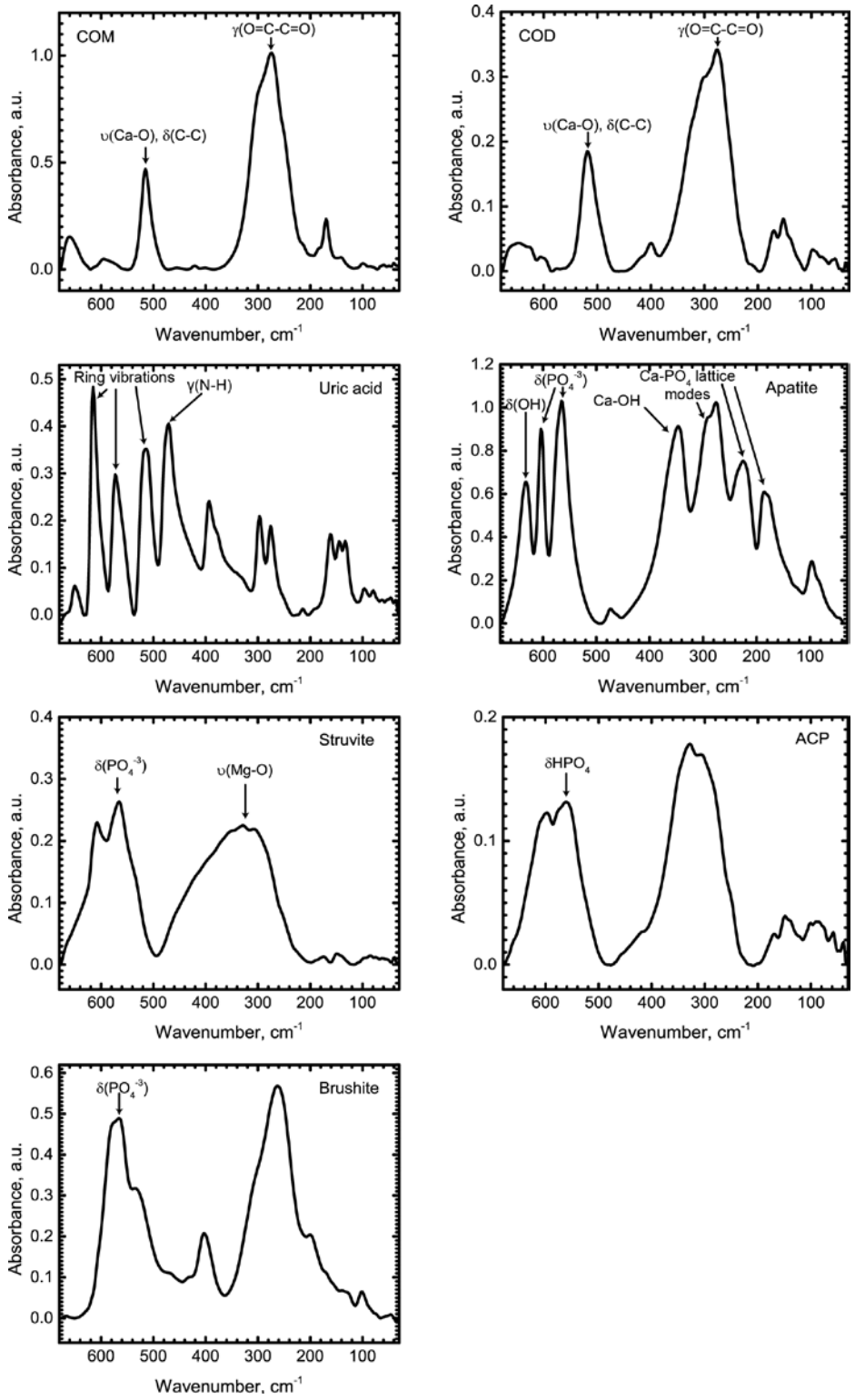

Fig. 11. FIR absorption spectra of mineral components the most frequently found in urinary stones. Some of the spectral bands in the spectra (marked by arrows) could be assigned to molecular vibrations as described in the literature [160-166].

Normalized MIR and FIR absorption spectra of urinary stone constituted from uric acid and COM are compared in Figure 12. Spectral bands which are characteristic to each chemical component and which were later used to produce chemical images are denoted by dotted lines. In the spectra of the stone (Fig. 12 A, B (top)), spectral bands of the stone's constituents are much better separated in the FIR spectral region than they are in the MIR spectral region. In the latter, bands of COM (ν(C=O) at 1625 cm^{-1}, ν(C-O) at 1318 cm^{-1}, δ(O-C=O) at 782 cm^{-1} [167]) and uric acid (ν(C=O) at 1673 cm-^{1}, δ(O-H) at 1301 cm^{-1}, ring vibration at 1121 cm^{-1},

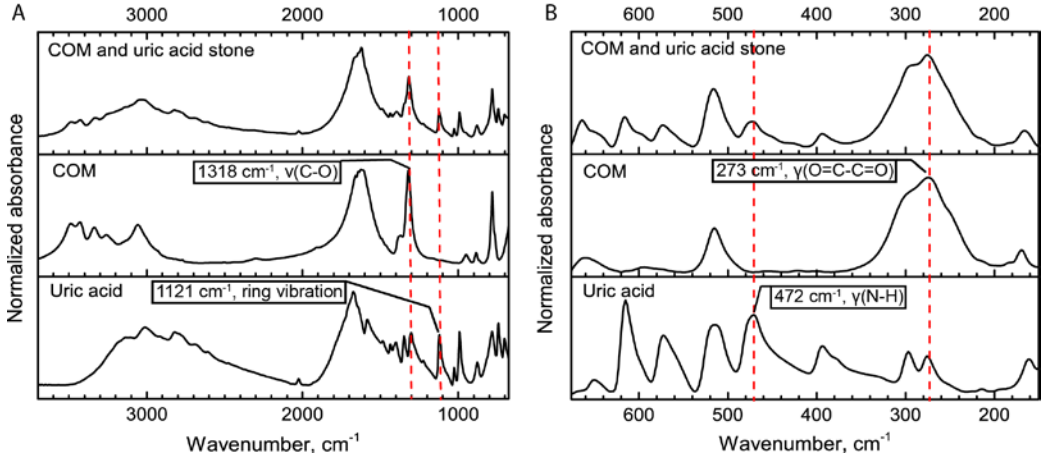

Fig. 12. MIR (A) and FIR (B) absorption spectra of urinary stone constituted from COM and uric acid (top) and spectra of corresponding synthetic components (middle and bottom); red dotted lines mark spectral bands characteristic to COM and uric acid.

δ(N-H) at 783 cm^{-1} [161]) are of similar intensities and are highly overlapped. For this reason, small amounts (approximately $c_{\text{uric acid}} > 4 \cdot c_{\text{calcium oxalate}}$) of COM could hardly be identified from the MIR spectra. Meanwhile, in the FIR spectral region, the band at 274 cm^{-1} assigned to γ(O=C-C=O) of COM [160] can be clearly distinguished as the spectral bands of uric acid absorption in this region are weak. Similarly, the presence of uric acid is determined by distinctive absorption bands in the 700 – 550 cm^{-1} spectral region.

Quantitative analysis of urinary stones could only be performed for urinary stones, constituted from those chemical components which had their

synthetic counterparts the spectra of which could be recorded in our laboratory. The analysis was performed as described in section 2.3.8. The accuracy of the quantitative analysis in both MIR and FIR spectral regions is defined by the accuracy of the calculations of the integral intensities. It is approximately 5 % as determined by performing quantitative analysis of mixtures of synthetic minerals – COM and uric acid – in various concentrations.

2.4.1. IR chemical imaging of urinary stones: modified KKT correction of reflectance spectra

In the external reflectance measurements, the spectral band shapes are affected by the dispersion of refractive index. The dispersion affected spectral bands, or Reststrahlen bands, appear as first derivative of absorbance spectral bands: they acquire negative values at the high frequency side and their peak position is red shifted. Such distortions introduce error into the chemical images formed by calculating integral intensities of the Reststrahlen bands. When the recorded reflection signal is a sum of both specular and diffuse reflections standard KKT procedure cannot be used to correct the distortions due to assumption made during derivation of the relations. In this work, we firstly made an attempt to modify the KKT correction procedure by subtracting the diffuse reflection component from the reflectance spectra of cross-sectioned calculi prior the transform. The correction procedure was applied to the relevant spectral bands in the spectra (the bands specific to a particular chemical component in the stone, not overlapping with spectral bands of other components in the spectra of mixed stones) only. Corresponding bands from the IR absorption spectra of the pure components, obtained employing KBr pellet technique, were used for the subtraction. The remaining specular reflection component was then corrected by applying the KKT. Finally, in order to retain spectral information,

the corrected specular reflection component was combined with the subtracted diffuse reflection component. The amount of diffuse reflection that had to be subtracted was determined iteratively: the diffuse reflection contour was multiplied by a constant which was varied until the peak position and the contour symmetry after the KKT resembled those of the spectral band in the absorption spectrum. Such constant was found for each spectrum in the data set. The outliers were omitted from the correction and their integral intensities were automatically assigned to zero (block scheme of the procedure is presented in the Appendix I Fig. AI-1).

Spectral band at 1318 cm^{-1} (symmetric C-O stretch in COM [167]) taken from the reflectance spectrum of the urinary stone constituted from COM and uric acid recorded in the area of COM is presented in Figure 13. The spectrum in A shows the band in the raw reflectance spectrum while the

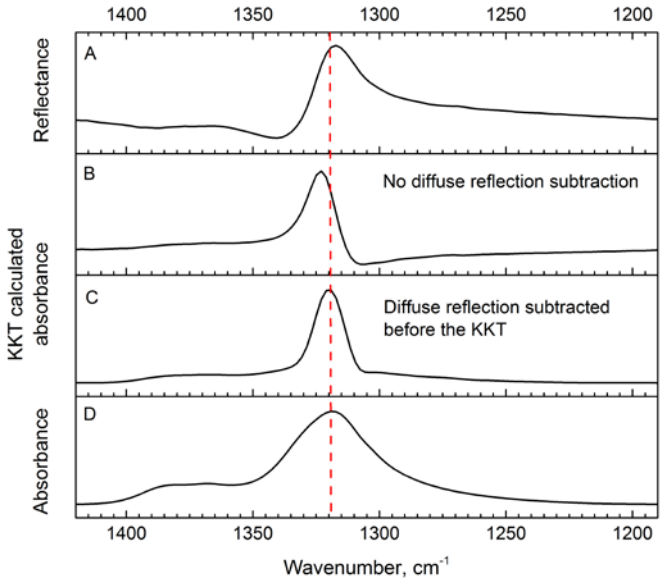

Fig. 13. Reflectance (A), KKT calculated absorbance without (B) and with (C) prior diffuse reflection subtraction and absorbance (D) spectral bands of COM at 1318 cm^{-1}. Reflectance spectrum in (A) was recorded in the area of COM in the cross-section of urinary stone constituted from COM and uric acid. Absorbance spectrum is recorded by preparing synthetic COM powder for transmission measurements by KBr pellet technique.

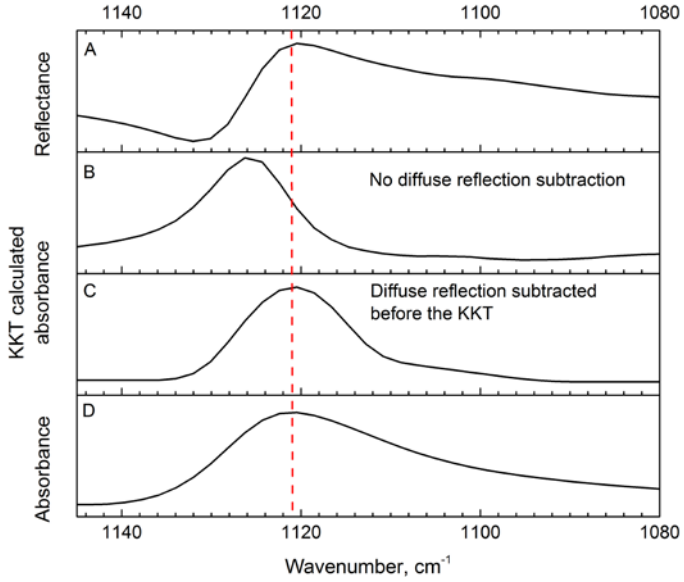

Fig. 14. Reflectance (A), KKT calculated absorbance without (B) and with (C) prior diffuse reflection subtraction and absorbance (D) spectral bands of uric acid at 1121 cm^{-1}. Reflectance spectrum in (A) was recorded in the area of uric acid in the cross-section of urinary stone constituted from COM and uric acid. Absorbance spectrum is recorded by preparing synthetic uric acid powder for transmission measurements by KBr pellet technique.

curve in B represents the band corrected by applying the KKT without any pre-processing. It can be seen that the band shape and the peak position does not match the COM absorption band (Fig. 13 D). The difference and the blue shift of the band could be explained by the influence of the diffuse reflection [31].

Normally, Reststrahlen spectral bands are red shifted comparing them to the absorption spectral bands. The KKT restores the peak positions. However, in this case, the influence of the diffuse reflection blue shifts the Reststrahlen bands causing the KKT to overestimate the peak position. As a result, the calculated band appears blue shifted comparing it with the absorption spectral bands. The same band corrected by applying the modified KKT method when the diffuse reflection component is subtracted from the recorded reflectance spectrum is presented in Figure 13 C. In this case, the peak position is restored and the first-derivative like dispersion contour

corrected to correspond with the absorption band (Fig. 13 D). The same results were obtained for the spectral band of uric acid at 1121 cm^{-1} assigned to ring vibrations (Fig. 14) [161].

The optical and IR chemical images of the urinary stone are presented in Figure 15. Characteristic spectral bands were selected to be used for the chemical imaging: the band at 1318 cm^{-1} for COM and the band at 1121 cm^{-1} for uric acid. The area of the cross-section is approximately 9×8 mm and it was mapped using ~300×300 µm step of the microscope xyz-stage. By comparing the images obtained by calculating the integral intensity of spectral bands in the raw spectra (Fig. 15 B, C) and in the corrected spectra (Fig. 15 D, E) it can be seen that the latter corresponds better with the optical image than the former. In addition, the contrast is higher and the boundaries between layers of uric acid and COM can be separated more precisely. As it

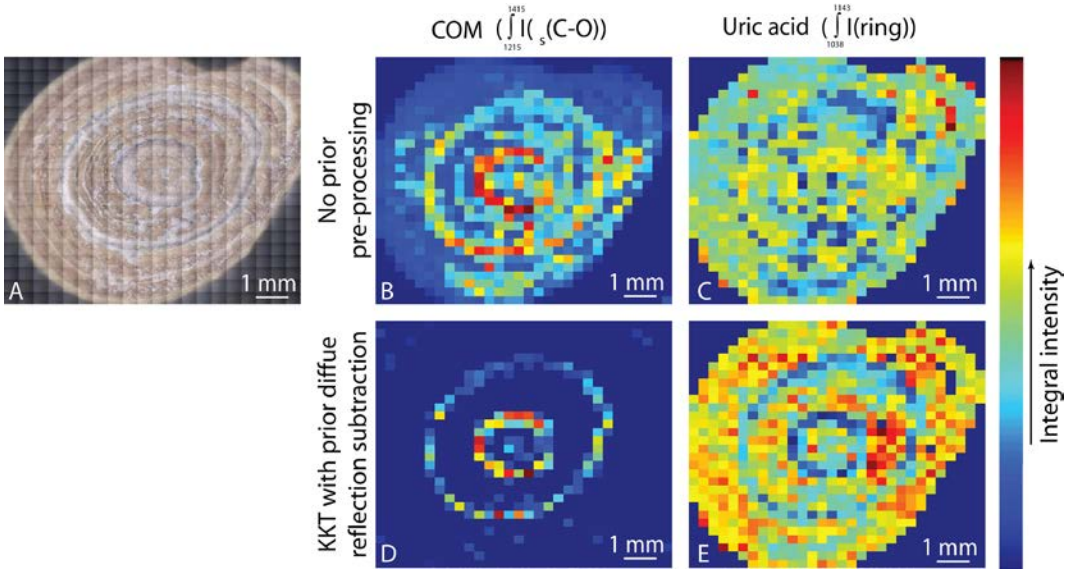

Fig. 15. Optical (A) and IR chemical (B-E) images of urinary stone constituted from COM and uric acid. (B) and (C) shows distribution of COM and uric acid respectively as determined by calculating integral intensity of characteristic spectral bands in the raw spectra; (D) and (E) shows distribution of COM and uric acid respectively as determined by calculating integral intensity of characteristic spectral bands in the KKT corrected spectra after the subtraction of diffuse reflection.

was found that applying the KKT to the raw reflectance spectra without the subtraction procedure yielded asymmetric bands, corresponding chemical images were not constructed.

Similar results were obtained for urinary stones with different chemical compositions (refer to Fig. AI-2 – AI-7 in the Appendix I). Contrast of chemical images of COM and uric acid in the cross-sectioned stones were improved in the most of cases. However, applying the correction procedure to spectral bands of apatite did not provide the expected results. Chemical images obtained by calculating the integral intensity of spectral bands in the corrected spectra were highly distorted. This could be explained by the fact that the shape of the contour of the characteristic spectral band assigned to PO_4^{-3} vibrations in apatite is different in the IR absorption spectra of synthetic mineral and in the stones. This is due to the fact that the synthetic mineral is highly crystalline which gives rise to sharper spectral bands. On the other hand, apatite in urinary stones is less structured or even amorphous which gives rise to broader spectral bands. Subtraction of such differently shaped contours in order to account for the diffuse reflection signal in the reflectance spectra is not appropriate and causes distortions in the chemical images of apatite. The one exception to this is presented in Fig. AI-4 (Appendix I). Apatite spectral bands in this particular stone were of similar shape as the band of the synthetic mineral; thus contrast in the corrected image of apatite in the cross-section of this stone is improved. Apatite can be well distinguished in the other chemical images obtained by calculating the integral intensity of spectral bands in the raw spectra. This is reasoned by the fact that the characteristic spectral band of apatite is broad and less influenced by the diffuse reflection as it lies in the spectral region of lower wavenumbers (1036 cm^{-1}, PO_4^{-3} stretch) as compared to the characteristic spectral bands of COM and uric acid.

2.4.2. IR chemical imaging of urinary stones: MIR vs. FIR

Despite the fact that the diffuse reflection subtraction procedure followed by the KKT provided improved chemical images of urinary stones as compared to the images created from the raw reflectance spectra, this modification requires performing complex mathematical operations and data pre-processing. Further we show that expanding the wavelength region which is used fo r the chemical imaging to FIR can simplify the spectral analysis. Standard KKT procedure implemented in most of spectral analysis software packages can be used to correct the Reststrahlen bands in the FIR spectra. The KKT corrected spectra can then be used for the chemical imaging.

Firstly, cross-sectioned urinary stone constituted from uric acid and COM (the same as presented in section 2.4.1.) was studied by means of confocal optical profilometer in order to determine the dimensions of

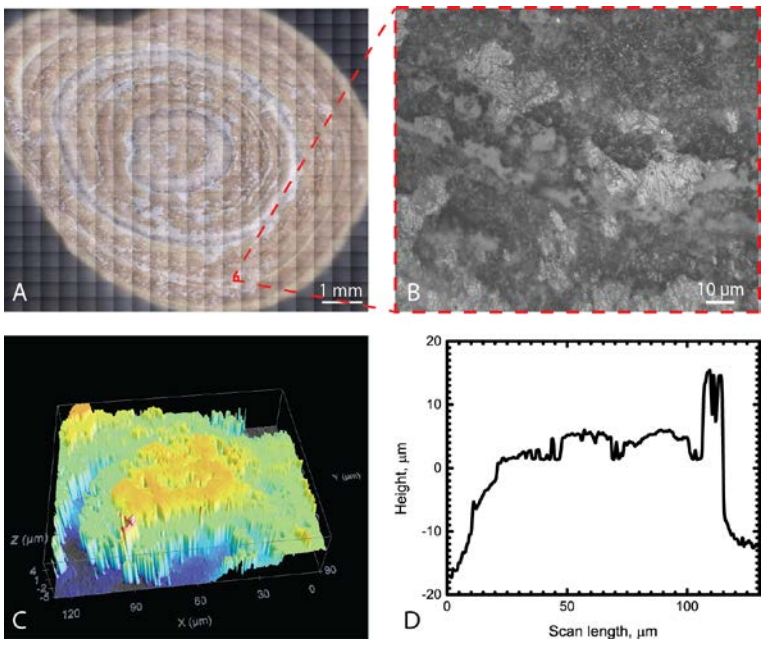

Fig. 16. (A) Optical image of urinary stone constituted from COM and uric acid; the red box in the image indicates a ROI which was analyzed by optical profilometer. (B) Enhanced optical image of the ROI indicated in (A). (C) 3-D topology of the ROI as obtained by the optical profilometer. (D) One dimensional profile of a diagonal section (from right upper corner to left down corner) in (C).

irregularities of its surface. Several regions of interest (ROI) were analyzed. For one of the selected ROI, the 3-D topology and one-dimensional profile of its diagonal section are presented in Figure 16 C, D. The size of the irregularities of the stone's surface was determined to vary in the range of 2 - 20 µm. It is notable, that the influence of surface roughness to the reflected light depends on the ratio between the size of the irregularities and the wavelength of the incident radiation [168]. In this context, the surface is considered rough and the diffuse reflection – strong, if the wavelength is close to the size of the irregularities, and vice versa - the surface is "mirror like" and the diffuse reflection is weak, if the wavelength is much larger than the size of the surface roughness. In case of the investigated stone, the

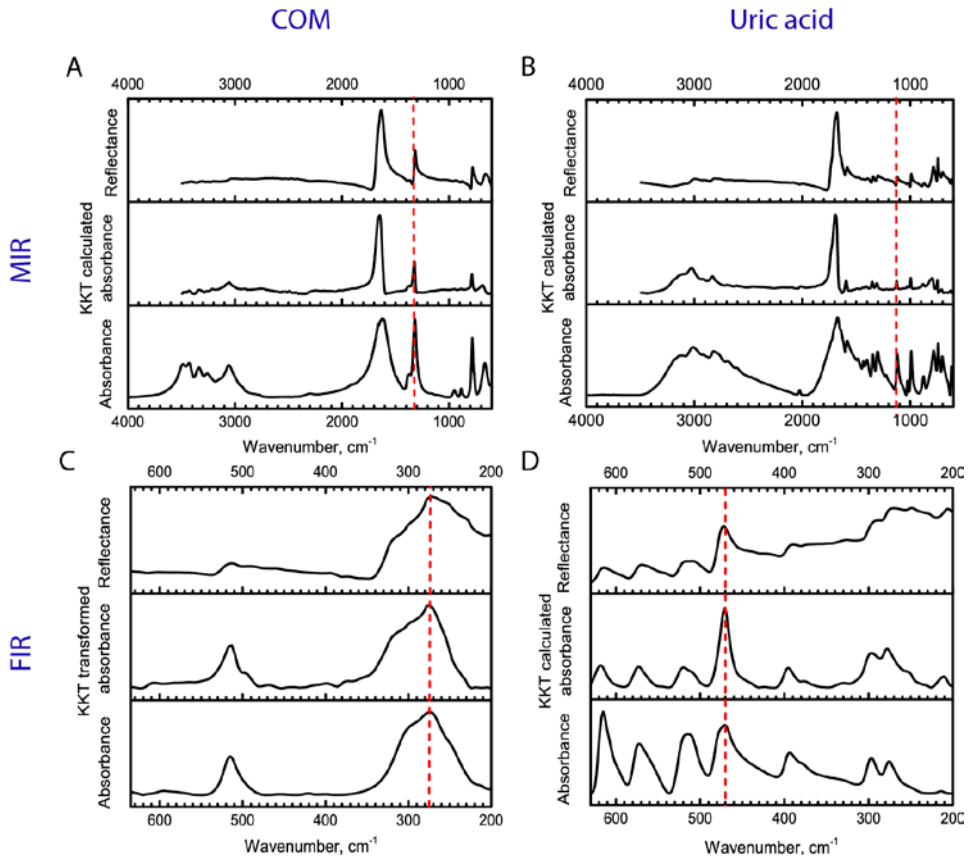

Fig. 17. Reflectance (top), KKT transformed reflectance (middle) and absorbance (bottom) MIR (A, B) and FIR (C, D) spectra characteristic to COM (left) and uric acid (right). Characteristic spectral bands for the both components in both spectral regions (refer to the main text) are marked by red dotted lines.

wavelength of MIR radiation (2.5 – 25 μm) has the same order of magnitude as the irregularities of the surface of the stone. Because of that, the recorded reflection signal contains a considerable part of diffuse reflection which should be subtracted from the data prior further analysis. On the other hand, the wavelength of FIR radiation (25 – 1000 μm) is larger than the roughness of the surface. Therefore, the contribution of the diffuse reflection to the specular reflection signal is then significantly lower and negligible.

To obtain the chemical images by calculating integral intensities, characteristic spectral bands (in both MIR and FIR spectral regions) were selected as follows: ν_s(C-O) vibration band at 1318 cm^{-1} for COM (integration limits 1215 - 1415 cm^{-1}), ring vibrations' band at 1121 cm^{-1} for uric acid (integration limits 1038 - 1143 cm^{-1}), γ(O=C-C=O) band at 274 cm^{-1} for COM (integration limits 195 - 360 cm^{-1}) [160] and γ(N-H) - at 472 cm^{-1} for uric acid (integration limits 411 - 490 cm^{-1}) [169]. KKT transformed reflectance and absorbance MIR and FIR spectra characteristic to COM and uric acid are presented in Figure 17. As already discussed in the previous section, due to influence of the diffuse reflection, the KKT transformed bands in the MIR spectral region (Fig. 17 A, B (middle)) are asymmetric and different from the bands in the absorption spectrum (Fig. 17 A, B (bottom)). On the other hand, the spectral bands in the FIR spectrum are restored correctly by the KKT (Fig. 17 C, D (middle)) and reproduce the bands in the reference spectrum obtained by PE pellet technique (Fig. 17 C, D (bottom)). Of note, in the FIR reflection spectrum of uric acid, the relative intensities of spectral bands in the 700 – 550 cm^{-1} spectral region are changed as compared to the FIR absorption spectrum. This can be explained by the fact that negative part of each of the Reststrahlen bands diminishes intensity of an adjacent spectral band on the larger wavenumbers' side. Therefore, the band at 474 cm^{-1} appears as the most intense. Despite the fact that the KKT restores the

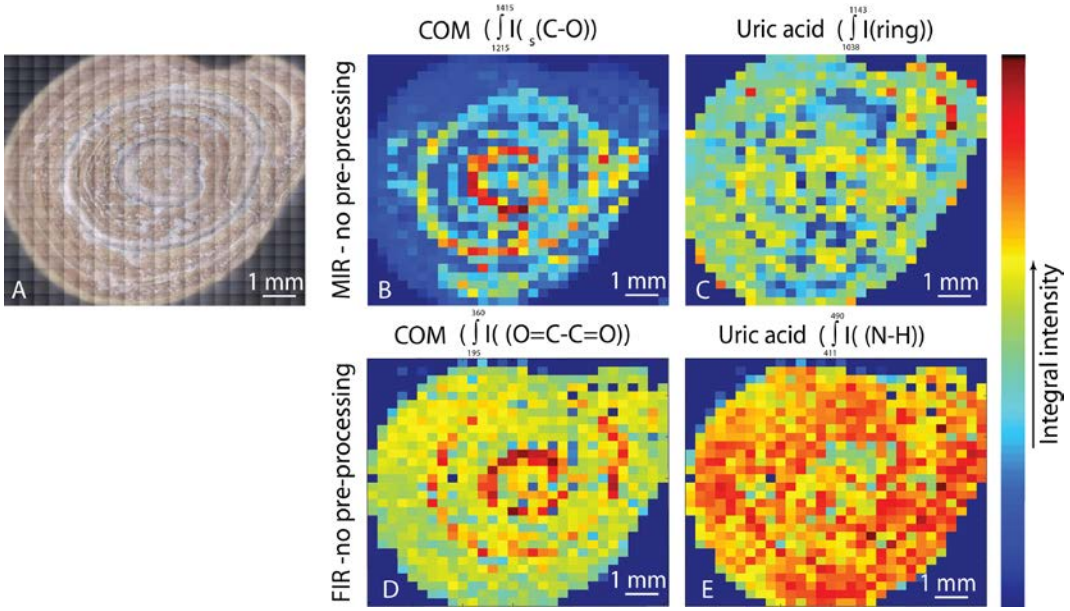

Fig. 18. Optical (A) and IR chemical (B-E) images of urinary stone constituted from COM and uric acid. (B) and (C) shows distribution of COM and uric acid respectively as determined by calculating integral intensity of characteristic spectral bands in the raw spectra in MIR spectral region; (D) and (E) shows distribution of COM and uric acid respectively as determined by calculating integral intensity of characteristic spectral bands in the raw spectra in FIR spectral region.

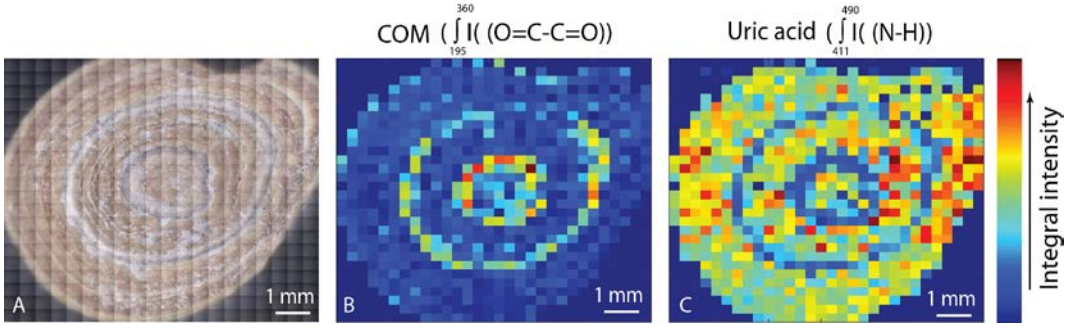

Fig. 19. Optical (A) and IR chemical (B, C) images of urinary stone constituted from COM and uric acid. (B) and (C) shows distribution of COM and uric acid respectively as determined by calculating integral intensity of characteristic spectral bands in the FIR spectral region after applying the KKT.

asymmetry of the spectral contours and shifts of the spectral bands, the relative intensities remain unaccounted for.

The optical and chemical images representing the analyzed urinary stone are shown in Figure 18. The chemical images were obtained from the raw MIR and FIR spectra. These chemical images represent the distribution of particular chemical component (in this case, COM (Fig. 18 B, D) and uric acid (Fig. 18 C, E)) throughout the cross-section of the stone. When raw reflectance spectra are used for the imaging, the information about the structure of the stone that can be obtained is similar both for MIR and FIR images: the boundaries between the components are not clear and the contrast of the images is low. The arrangement of the chemical components throughout the cross-section that can be seen in the optical image (Fig. 18 A) is hardly distinguishable in the corresponding chemical images. Further, we will show that in order to obtain more informative chemical images and better determine the structure of urinary stones, the FIR reflectance spectra should be KKT transformed prior the calculation of the integral intensities of the spectral bands.

Chemical images formed from the FIR reflectance spectra after applying the KKT are presented in Figure 19. The apparent differences can be seen between the images in Figure 18 and Figure 19. In the latter, the contrast of the chemical images is better; therefore, more structural details can be distinguished. In addition, the images correspond well with the optical image of the cross-section presented in Figure 19 A: the ring structure that can be seen in the optical image is confirmed to be layers of different chemical components – COM and uric acid. As mentioned in the previous section, it was found that applying the KKT to the MIR reflectance spectra yielded asymmetric bands and corresponding MIR chemical images were not constructed.

2.4.3. FT-Raman chemical imaging of urinary stones

So far, the results of the chemical imaging were compared with the optical image of the stone. However, obtaining a master image which would represent a true distribution of the chemical constituents would provide quantitative evaluation of the images' quality [170]. Therefore, FT-Raman imaging of the same cross-sectioned stone constituted from COM and uric acid was carried out. Raman spectral bands do not suffer from distortions caused by anomalous dispersion and their integral intensities can be used to form chemical images without any pre-processing; thus, the images obtained do not contain artefacts caused by calculation errors and can be considered to

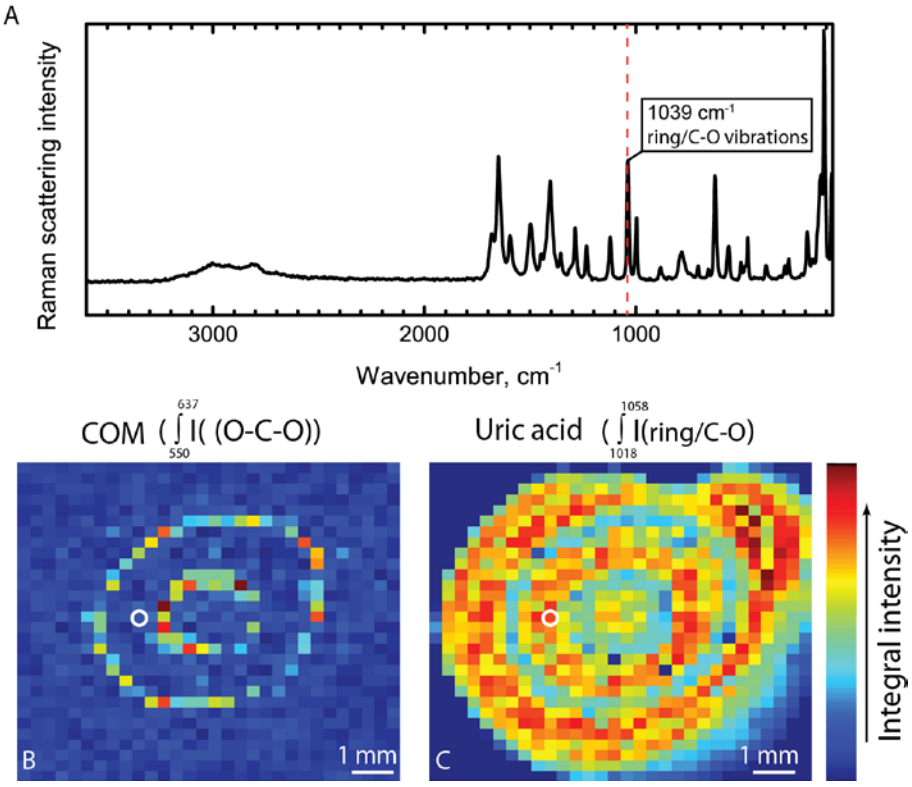

Fig. 20. Raman spectrum (A) and checmical images (B, C) of urinary stone constituted from COM and uric acid. (B) and (C) shows distribution of COM and uric acid respectively as determined by calculating integral intensity of characteristic spectral bands in the Raman spectra. The spectrum in (A) was recorded in an area of uric acid indicated by the white circles in the chemical images. The red dotted line marks spectral band characteristic to uric acid at 1039 cm^{-1} assigned to ring and C-O vibrations.

represent the real distribution of the chemical components. However, the time needed to collect the Raman spectra is much longer (approx. 40 hours) than the time needed to measure MIR or FIR reflectance spectra (approx. 8 – 15 hours). Therefore, IR imaging is a preferable technique for the chemical and structural analysis.

The same step between mapping points was used in the FT-Raman experiment as in the FTIR microscopy. The bands at 1039 cm^{-1} of normal vibrational mode which includes the ring and C-O vibrations in uric acid (integration limits 1018 - 1058 cm^{-1}) [42] and at 597 cm^{-1} of O-C-O deformation in COM (integration limits 550 - 637 cm^{-1}) [171] were respectively chosen for the integration in order to form the chemical images representing distribution of uric acid and COM.

In Figure 20 A, Raman spectrum collected in the area of the stone containing uric acid (designated in Fig. 20 B, C) is presented. The Raman images (Fig. 20 B (COM), C (uric acid)) lead us to similar conclusions concerning the distribution of the chemical components as the images obtained from the FIR spectra corrected by the KKT. In order to evaluate the quality of the MIR and FIR images, subtraction procedure was performed: Raman images were considered to be the master images (representing real distribution of the components) and they were subtracted from MIR and FIR images [170]. The images were normalized for pixels to have values between 0 and 1 before the procedure. The RMS (root-mean-square) error of the residual for the MIR image, constructed from the raw spectra, is 44.33, for the FIR image, constructed from the raw spectra – 36.98 and for the FIR image, constructed from the KKT corrected spectra – 13.42. This result confirms that FIR image, constructed from the KKT corrected spectra, has higher quality and that FIR microspectroscopy can be effectively used for the chemical imaging of urinary stones.

Considering the obtained results, FIR imaging seems to be superior to the MIR imaging in case of chemical imaging of rough (2 – 25 μm in the case of MIR radiation) surfaces by specular reflection mode. Therefore, before the multi-spectral IR analysis of urinary stones, one should evaluate the magnitude of the surface irregularities and choose the appropriate method.

2.4.4. IR chemical imaging of urinary stones: use of HCA

As shown above, chemical imaging is normally performed by calculating integral intensities of characteristic spectral bands and assigning colors to the obtained values. The color in the chemical image is then proportional to concentration of particular chemical component (or functional group) in a particular area of the sample. However, external reflectance spectra are complicated to analyze as the KKT has to be applied to the Reststrahlen spectral bands prior the integration procedure in order to obtain reliable chemical images. In addition, diffuse reflection contributing to the overall reflection signal obstructs the analysis in the MIR spectral region and has to be subtracted from the spectra prior applying the KKT. This requires performing complex data processing which introduces artefacts into the images. In the FIR spectral region, diffuse reflection has no or less influence and the KKT can be successfully performed. However, microspectroscopic measurements in the FIR spectral region requires sophisticated equipment which is currently difficult, if not impossible, to implement in routine analysis.

Due to reasons stated above, multivariate data analysis, namely HCA, was performed to construct chemical images of the urinary stones. The HCA chemical images constructed from the MIR (no KKT) and FIR (KKT transformed) reflectance spectra of urinary stone constituted from COM and uric acid (the same that was analyzed above) are presented in Fig. 21 B and C. Both images contain four groups identified by the HCA. The spectra of each group (excluding group No. 1 (dark blue) which corresponds to outliers) are

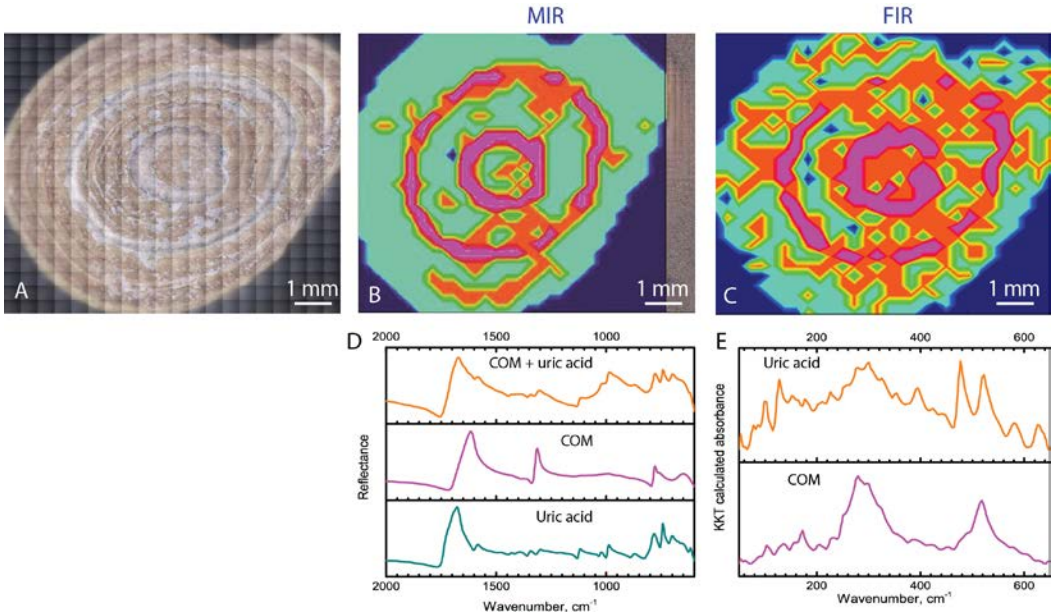

Fig. 21. Optical (A) and IR chemical (B, C) images of urinary stone constituted from COM and uric acid: (B) chemical image obtained by HCA analysis of MIR spectra, (C) chemical image obtained by HCA analysis of FIR spectra. IR reflectance spectra in (D) and (E) correspond to areas of different color (different chemical composition) in (B) and (C) respectively.

presented in Fig. 21 D and E. The group No. 2 (mint-green) corresponds to spectra of uric acid, group No. 3 (orange-red) – uric acid mixed with COM and group No.4 (pink) – COM. Both HCA chemical images provide similar information and corresponds well to the chemical images of the same stone presented in the previous sections (refer to Figure 18 (MIR), Figure 19 (FIR) and Figure 20 (FT-Raman)) obtained by calculating integral intensities of characteristic spectral bands. However, MIR spectra are of higher signal-to-noise ratio and the bands are narrower as compared to the FIR spectra; thus, groups containing different spectral features are separated better by the HCA. Subsequently, areas of different constituents are better defined in the HCA chemical image formed from the MIR spectra. In the HCA chemical image formed from the FIR spectra, areas of COM are well separated; however, due to broad spectral bands and higher noise level in the spectra the rest of the cross-section is recognized as mixture of COM and uric acid instead of pure uric acid. The fact that high quality chemical images can be obtained by HCA

of the MIR spectra without performing any band correction procedures or additional pre-processing makes the HCA chemical imaging of urinary stones an attractive option for routine analysis.

While chemical images obtained by performing HCA analysis provide qualitative information about the distribution of chemical components in the cross-section of the urinary stone, quantitative information is lost. Therefore, chemical imaging by calculating integral intensities of characteristic spectral bands should be performed when semi-quantification of the components is necessary. However, the HCA chemical imaging is less sensitive to the contour shape of Reststrahlen spectral bands and neglects the influence of the diffuse reflection providing superior qualitative information as long as correct number of groups is pre-selected. As HCA is a built-in function of many data analysis software, it does not require any complex algorithms of analysis to be written (as in the case of diffuse reflection influenced MIR reflectance spectra). Also, no changes in the custom measurement procedure are necessary (as in the case of FIR reflectance microspectroscopy).

***

So far, the effects of using MIR and FIR microspectroscopy and different data analysis methods have been demonstrated on a single stone. Of note, similar results were obtained for other urinary stones of various types as well (Appendix II). In all the cases when integral intensities were used for the chemical imaging, FIR images provided information about the chemical composition of the stone which correlated well with the results obtained by standard IR absorption spectroscopy. In addition, the information about the distribution of the constituents throughout the cross-section of the stone was obtained. When similar (or the same) amount of data points were recorded when performing the spectral mapping, FIR chemical imaging provided

superior results to the MIR chemical imaging. This is due to several reasons. Firstly, as discussed above, impact of diffuse reflection is suppressed when FIR radiation is used and KKT can be applied to the spectra. This means that calculation of integral intensities of characteristic spectral bands can be done more precisely. Secondly, recording external reflectance spectra in the FIR spectral region is less sensitive to slight variations in surface height (focus) appearing due to natural pores in the stone or brittleness of the mineral.

Use of HCA for constructing the chemical images both in MIR and FIR spectral regions provided similar or, in many cases, superior qualitative information about distribution of constituents in the stones' cross-sections than the usually used integration of characteristic spectral bands. To calculate the integral intensities, spectral bands have to be well separated. In the FIR spectral region, the bands are broad which makes selection of integration limits difficult. On the other hand, the HCA takes every point of the spectra into account, thus every spectral feature is used to separate spectra into groups. This is especially evident when imaging stones containing ACP in the FIR spectral region. Spectral features characteristic to the ACP (at 675-500 cm^{-1} and 475-225 cm^{-1}) are weak, very broad and overlapping with spectral bands of COM. Therefore, distribution of the ACP cannot be clearly determined by calculating the integral intensities. However, the HCA separates spectra containing spectral features characteristic to the ACP into separate groups which allows observing its distribution in the cross-sections of the stones.

Advantages of HCA over calculation of the integral intensities were also observed when imaging multi-component rather than two-component stones. The fact that characteristic spectral bands of all the constituents are at similar wavenumbers results in unreliable chemical images when the integral intensities are calculated. For instance, characteristic spectral band of uric acid at 1121 cm^{-1} is well separated in mixtures with COM. When calcium

phosphate (apatite) is present in the stone as well, integration of this spectral band provides non-zero results in the regions of the phosphate (characteristic spectral band at 1036 cm^{-1} assigned to asymmetric PO_4^{-3} stretch) in addition to the regions of uric acid. Other bands of uric acid are overlapping with spectral bands of COM and similar outcome is obtained. On the other hand, the HCA differentiates spectra to groups according to all spectral features rather than only one band and reliable information about distribution of all the constituents can be obtained. The fact that high quality chemical images can be obtained by HCA of the MIR spectra without performing any band correction procedures or additional pre-processing makes the HCA chemical imaging of urinary stones an attractive option for routine analysis.

One downside of the HCA is its sensitivity to noise in the spectra. This is particularly prominent in the FIR spectral region where the spectral bands are considerably weaker than in the MIR and water absorption is difficult to compensate for. The noisy spectra are often attributed to separate groups resulting in ambiguity of the imaging results.

2.4.5. Multimodal CARS chemical imaging of urinary stones

The drawback of the IR specular reflection microspectroscopic imaging is its limited lateral resolution which allows observing distribution of only major components in the cross-sections of urinary stones. For this reason, epi-detected nonlinear optical microscopy was used for imaging of the stones.

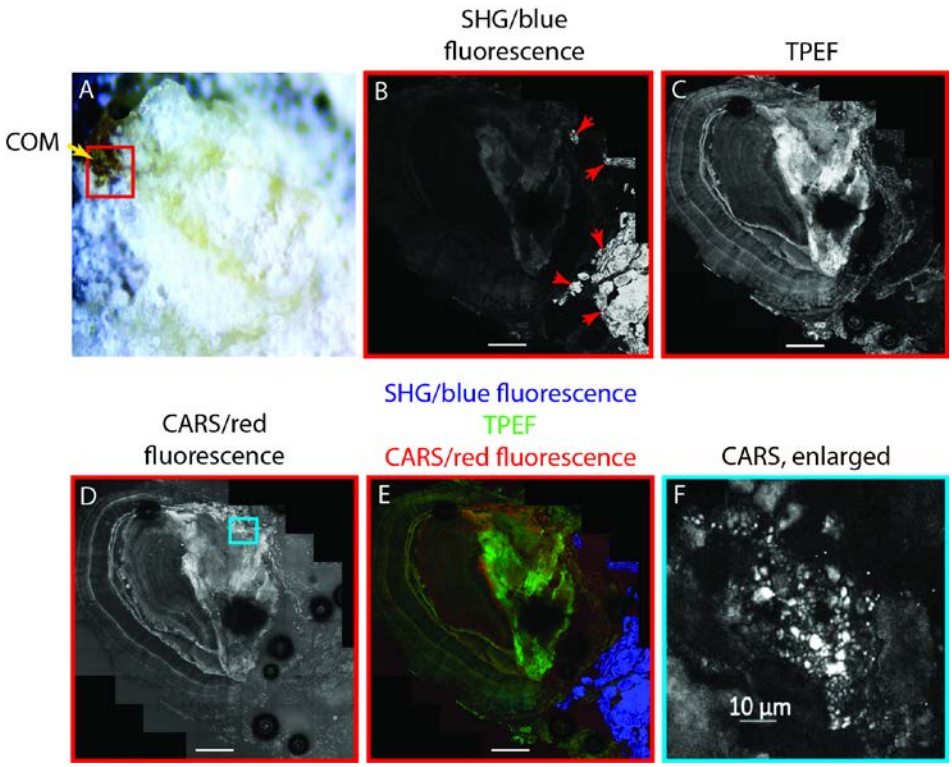

Fig. 22. Optical (A) and multimodal (B-F) images of urinary stone constituted from COM and struvite: (B) SHG(arrows)/blue fluorescence image, (C) TPEF image, (D) CARS/red fluorescence image, (E) merged SHG/blue fluorescence (blue), TPEF (green), CARS/red fluorescence (red) image. The box in A indicates an area images by the multimodal nonlinear optical microscopy. The box in (D) indicates the enlarged region which contains CARS-active structures represented in (F). The black circular spots in the images are due to bubbles in the immersion water. Scale bar (B-E): 200 µm.

Figure 22 shows optical and multimodal images of the surface of a halved urinary stone that is constituted from struvite and COM. The chemical composition of this stone was determined by performing infrared

transmission measurement of the other half of the stone prepared by KBr pellet technique as described in section 2.3.1. In the optical image (Fig. 22 A) segment of COM (dark brown, marked by arrow) is surrounded by the whitish mineral struvite. The area denoted by the red box in the image was analyzed by multimodal nonlinear optical imaging. Figure 22 B shows the SHG intensity image. It is expected that the SHG is generated by struvite (marked by arrows) as it belongs to a non-centrosymmetric orthorhombic space group ($Pmn2_1$ = = C_{2v}^7) [172]. Some signal at wavelength 390 nm is also generated by COM in all the analyzed stones. This signal is considerably weaker than that from struvite and is probably due to residual fluorescence emitted below 399 nm (further referred to as blue fluorescence) and therefore transmitted to the detector by the band-pass filter used for acquisition. To verify the origin of the signal from struvite in the stone, we compared the intensity of the signal acquired using the band-pass filter 381-399 nm and a broader filter transmitting all blue light below 480 nm to the detector. Intensity of the recorded signal was found to be the same with both filters, showing that the signal is emitted only at wavelengths very close to the half of wavelength of the pump beam and thus enabling us to conclude that it is SHG.

TPEF signal was observed in the region of COM (Fig. 22 C). Since no TPEF signal was recorded from synthetic COM powder (refer Fig. AIII-1 (Appendix III)), it is likely predominantly generated by pigments and organic macromolecules that are integrated into the COM lattice during the stone growth [144]. The origin of the blue fluorescence signal mentioned above can be explained in similar manner. Region of COM deposition also shows fluorescence in the 633-647 nm spectral region (further referred to as red fluorescence) and a weak CARS signal (Fig. 22 D). This was confirmed by turning the “Stokes” laser off – the intensity of the overall signal diminished slightly, but the fluorescence signal remained. However, the Raman spectrum of COM contains only weak spectral bands in the 3600-2800 cm^{-1} spectral

region that can be assigned to vibrations of water [173]; thus, the weak signal that is suppressed by turning off the Stokes laser is likely non-resonant background only, rather than a resonant CARS signal.

It has been shown by X. Sheng et al. that the adhesiveness of COM surface depends on its crystal face [174].Therefore, different layers of COM provide different fluorescence intensities which can be associated with changes in pigment/macromolecules density among the layers. In turn, the layers arranged in concentric circles are typical to COM stones (in this case, only segment of COM) and imply their intermittent and slow growth [144]. In the merged SHG/blue fluorescence, TPEF, CARS/red fluorescence image (Fig. 22 E) both COM and struvite segments of the stone can be clearly distinguished what demonstrates chemical sensitivity of the multimodal nonlinear optical imaging.

In addition to the weak signal generated by COM, strong CARS signal was observed localized in small crystal-like structures approx. 1-5 µm in size and randomly distributed across the cross-sections. The area denoted by the cyan box in Figure 22 D is shown enlarged in Figure 22 F for better visualization of the structures. The signal was verified to be CARS both by turning the “Stokes” laser off, which suppressed the signal and thus excluded presence of red fluorescence, and by detuning of the “Stokes” laser, which also strongly decreased the signal and thus ruled out the non-resonant background as main source of the signal. To the best of authors’ knowledge, such formations in the stones have never been reported before. They were found in most (8 out of 10) of the analyzed stones, independent of their type.

The strong CARS signal generated by these structures implies their organic origin for which the signal generated by addressing spectral band at 2850 cm^{-1} is normally intense due to CH_2 vibrations. Organic substances which are the most often found in urinary stones are purines (uric acid, ammonium hydrogen urate, xanthine, 2,8-dihydroxyadenine, etc.), l-cystine and proteins

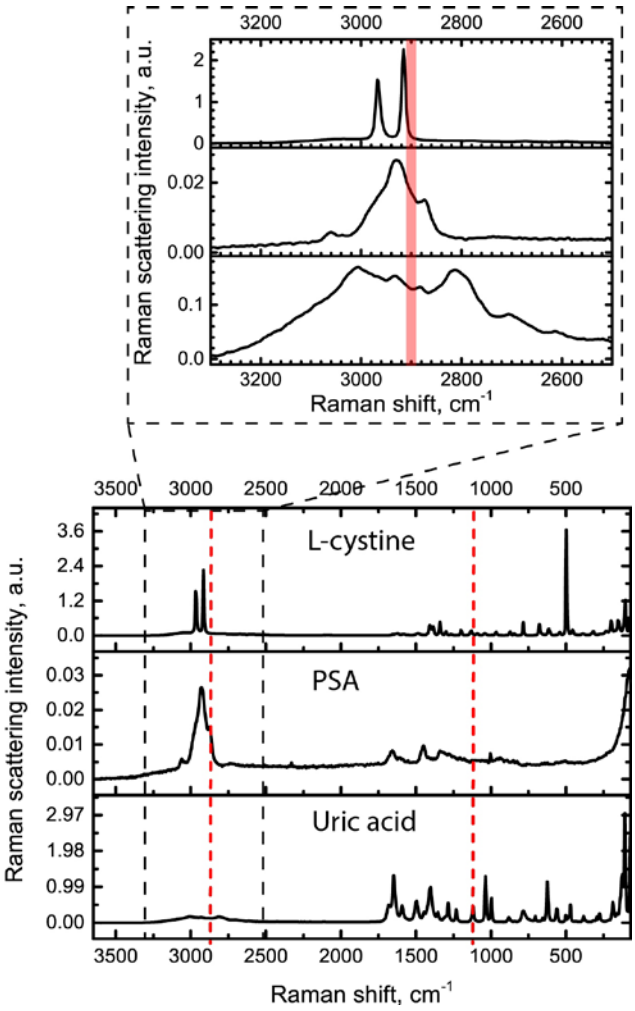

Fig. 23. FT–Raman spectra of uric acid, l-cystine and a protein representative – PSA; note the difference in Raman scattering intensity scale – uric acid bands are more intense than PSA at 2850 cm^{-1}.

[119]. FT-Raman spectra of pure uric acid (saturation of urine with other purines is relatively rare), l-cystine and a protein representative – PSA – are presented in Figure 23. They were all recorded under the same conditions and using the same excitation laser power. It can be seen that all the three substances have active spectral bands in the region between 3300 and 2600 cm^{-1}. In CARS microscopic imaging, the „Stokes" laser is set to address vibrations at 2850 cm^{-1} with full width at half maximum (FWHM) of 15 cm^{-1} (see the enlarged spectral region in Fig. 23) which means that either uric acid (N-H stretching vibrations) or proteins (CH_2 vibrations) could provide the CARS

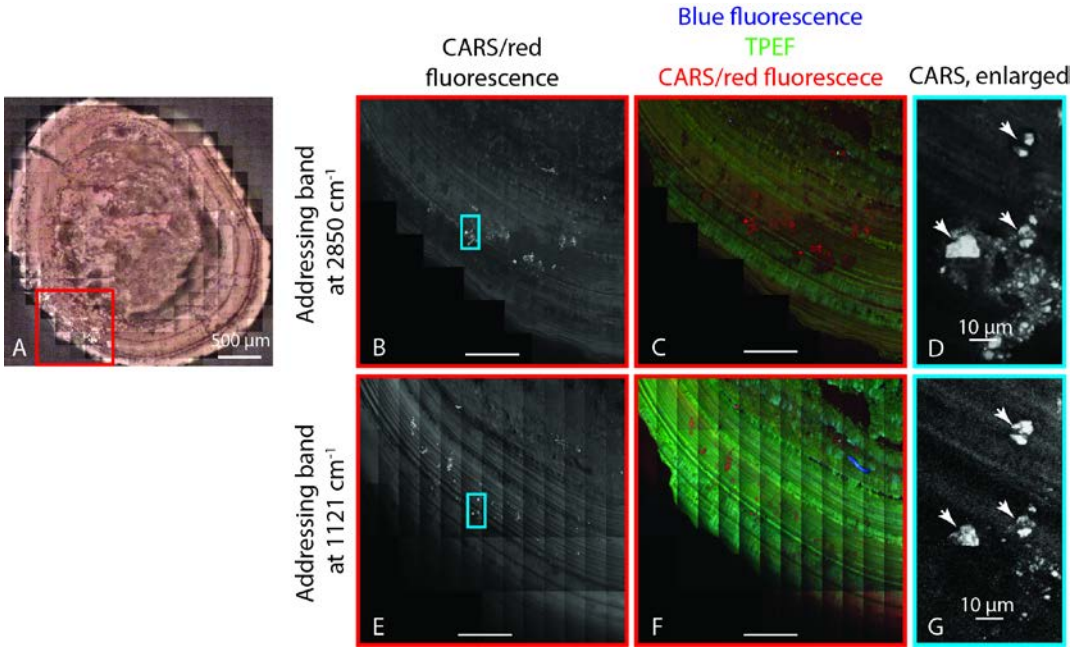

Fig. 24. Optical (A) and multimodal (B-G) images of urinary stone constituted from COM/COD and apatite. The box in (A) shows the areas imaged by the multimodal nonlinear optical microscopy. The CARS images were recorded at 2850 cm^{-1} (B-D) and 1121 cm^{-1} (E-G): (B, E) CARS/red fluorescence; (C, F) merged images: blue fluorescence (blue), TPEF (green) and CARS/red fluorescence (red). The boxes in (B) and (E) indicate the enlarged regions in (D) and (G) respectively, which contains CARS-active structures. Scale bar (B-C and E-F): 200 µm.

signal. Note, that the uric acid bands in this spectral region are more intense than the protein bands. In order to test which of the substances generates the CARS signal, we tuned the „Stokes" laser to 875 nm to resonantly address mixed C-O, C-N, C-C vibrations of uric acid at 1121 cm^{-1}. This band is specific to uric acid, but is lacking in the spectrum of proteins.

The CARS signal of these structures could be observed in the images of COM, COD and apatite stone obtained addressing both 2850 cm^{-1} and 1121 cm^{-1} vibrations (Fig. 24 B-G). An optical image of the stone's cross-section is presented in Figure 24 A. The red box in the image indicates the area imaged by multimodal nonlinear optical microscopy. In order to improve the contrast of the CARS image obtained addressing the band at 1121 cm^{-1}

(Fig. 24 E), an image with the „Stokes“ laser turned off was recorded and subtracted from the CARS image. This procedure allows removing the red fluorescence signal (at 670-745 nm in this case), which is more intense in this spectral region due to the broader band-pass filter used. Of note, the setting up of the multimodal imaging system after the laser tuning required sample to be removed from the sample stage. For this reason, the images addressing the band at 1121 cm^{-1} appear shifted as compared to the images at 2850 cm^{-1}. The enlarged view of areas indicated by cyan rectangles in the 2850 cm^{-1} CARS image and the subtracted 1121 cm^{-1} CARS image (Fig. 24 B and E) clearly shows that the same structures are observed in both images (marked by arrows). In accordance with the discussion above, this demonstrates that they are constituted from uric acid.

Of note, powder of synthetic uric acid was found to generate both CARS and weak TPEF signals (refer to Fig. AIII-2 (Appendix III)). Surprisingly, TPEF was not observed in the case of the small structures. It is possible that in the stones the TPEF signal of the small crystallites is not distinguished from the strong TPEF signal of the surrounding major constituents. The shape of the structures is also consistent with the usual monoclinic, pseudo-orthorhombic shapes of uric acid crystallites [175]. We also measured multimodal images of synthetic uric acid dihydrate (refer to Fig. AIII-3 (Appendix III)) – a possible uric acid hydration state in urinary stones. However, neither the shape of the crystallites nor the signal they generated was consistent with the structures found in the stones. While the uric acid dihydrate generated CARS signal is similar to that from uric acid, it also produced intense blue signal which was lacking in the crystallites found in the stones.

Hyperuricosuria (i.e., excessive amounts of uric acid in urine) has been related to formation of various types of calcium oxalate urinary stones [176]. It has been deduced that they can act as an inducer for formation of

unattached COM stones. On the other hand, random distribution of the uric acid crystallites observed in the CARS images in this work suggests that they were likely to be accidentally included from urine during the stone formation. Solubility of uric acid in water is low and, subsequently, uric acid micro-crystallites may be present in urine of even healthy people [177]. During formation of stones in urinary tract, the crystallites might be incorporated into the stones' structure. This could also explain the fact that the small structures were found present in almost all the analyzed stones of various types (calcium oxalate (COM/COD, possibly mixed with phosphates), uric acid

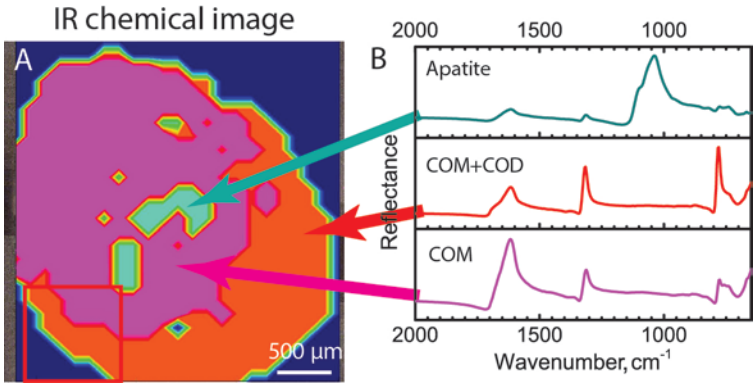

Fig. 25. IR chemical image (A) of urinary stone constituted from COM/COD and apatite. The box in (A) shows the area imaged by the multimodal nonlinear optical microscopy. IR reflectance spectra in (B) correspond to areas of different color (different chemical composition) in (A) as identified by the HCA.

(mixed with COM) and struvite (mixed with COM)).

In this case, both optical (Fig. 24 A) and IR chemical images (Fig. 25 A) were used for interpretation of the multimodal images. In the IR chemical image (Fig. 25 A), areas of different chemical composition were identified by HCA and color-coded so that the green color corresponds to areas of apatite, red – to mixture of COM and COD, magenta – to COM. Corresponding IR reflectance spectra are presented in Figure 25 B. It is noticeable that the microstructure and the layering of the stone can only be distinguished in the multimodal images (Fig. 24 B-G). The IR chemical image

presents a rough arrangement of the major constituents and allows discriminating regions of COM and COM+COD. These two hydrates of calcium oxalate could not be distinguished in the multimodal images.

Optical and multimodal images of a urinary stone constituted from uric acid and COM are presented in Figure 26. An optical image of the stone's cross-section is presented in Figure 26 A. The red box in the image denotes the area imaged by multimodal nonlinear optical microscopy. The CARS signal at 2850 cm^{-1} (Fig. 26 B) is predominantly generated by uric acid and was not observed with the "Stokes" laser off (only weak red fluorescence in this case). As CARS and TPEF (Fig. 26 C) signals were generated from the same structures arranged in direction perpendicular to the edge of the stone, we conclude, that TPEF signal was also predominantly generated by uric acid. However, the TPEF signal generated by synthetic uric acid powder was considerably weaker than the signal observed in the stones. Therefore, it is likely that the TPEF signal is additionally generated by macromolecules and pigments (such as uricine) incorporated into the structure of the stone. The small crystalline structures of uric acid could be discriminated in the CARS image as well. The area denoted by cyan box in Figure 26 B is enlarged and presented in Figure

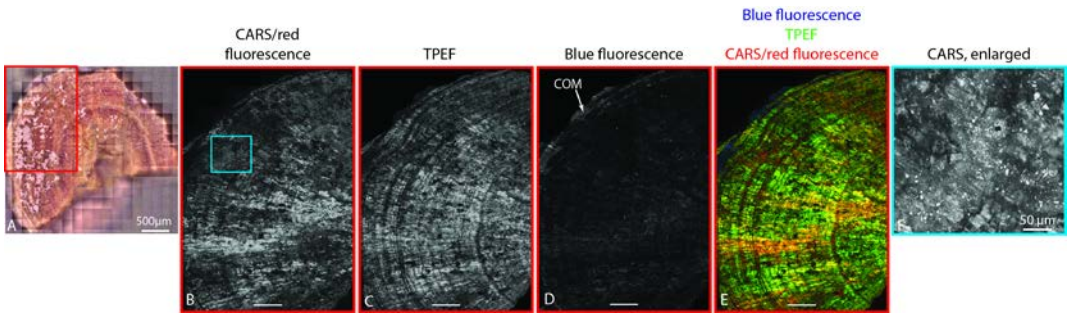

Fig. 26. Optical (A) and multimodal (B-F) images of urinary stone constituted from uric acid and COM. The box in (A) shows the area imaged by the multimodal nonlinear optical microscopy: (B) CARS/red fluorescence intensity image; (C) TPEF signal intensity image; (D) blue fluorescence signal intensity image; (E) merged image: blue fluorescence (blue), TPEF (green) and CARS/red fluorescence (red). The box in (B) indicates the enlarged region represented in (F), which contains CARS active-structures. Scale bar (B-E): 200 µm.

26 F. The crystallites are clearly visible as the CARS signal they generate is somewhat stronger than the bulk uric acid. The reason for this is not known. The COM in the stone can be discriminated as well (arrow in Fig. 26 D) since, in addition to the TPEF signal, it gives rise to weak blue fluorescence signal.

As in the case of the previously described urinary stone, microstructure and layering of the stone in Figure 26 can only be distinguished in the multimodal images while only arrangement of major constituents is revealed in the IR chemical image (Fig. 27). This is exceptionally relevant in the case of determining presence of COM in the stone: its layer can be well discriminated in the multimodal images while the chemical image only suggests presence of COM in the outer layer of the stone (green color).

In total, 10 stones of five different types were analyzed in this work (refer to Fig. AIII-4 – Fig. AIII-10 (Appendix III)): 4 stones were constituted from calcium oxalate, possibly with impurities of amorphous calcium phosphate (ACP), 2 stones of calcium oxalate and apatite, 3 stones of COM and uric acid, one stone of COM and struvite. TPEF, blue and red fluorescence, as well as weak CARS signal were generated by COM in all the stones. Since no

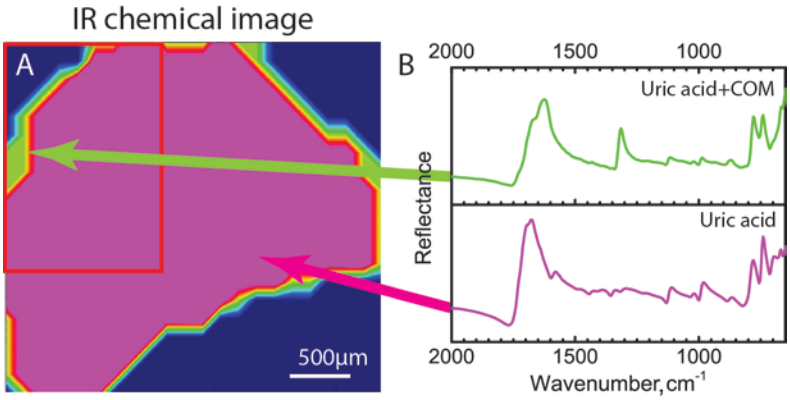

Fig. 27. IR chemical (A) image of urinary stone constituted from COM/COD and apatite. The box in (A) shows the area imaged by the multimodal nonlinear optical microscopy. IR reflectance spectra in (B) correspond to areas of different color (different chemical composition) in (A) as identified by the HCA.

fluorescence signal was generated by synthetic powder of COM, we deduced that it is likely predominantly generated by pigments and organic macromolecules that are integrated into the COM lattice during the stone growth. Neither COD nor ACP could be discriminated from COM in the multimodal images (Fig. 24, Fig. AIII-4 – Fig. AIII-7, Fig. AIII-10 (Appendix III)). Apatite, on the other hand, generated both red fluorescence and blue fluorescence, as well as and green TPEF signal (Fig. AIII-8 (Appendix III)). These signals were more intense than those generated by COM and thus clearly distinguishable. Uric acid in the stones generated intense CARS (at 2850 cm^{-1}) and TPEF signal. The latter was considerably weaker in synthetic powder of uric acid, thus, the TPEF signal is likely generated predominantly by macromolecules and pigments (uricine), which also give a yellow to orange color to the component. Finally, intense SHG signal was generated by struvite due to its non-centrosymmetric orthorhombic crystal structure. These five chemical components constitute the majority (93.5 %) of human urinary stones [131]. The results presented in this work show that four of them can be clearly discriminated in the multimodal images. The CARS active microcrystallites were observed in 8 out of 10 analyzed stones. They appeared of similar shapes and sizes and were randomly distributed in all types of the stones.

Given that nonlinear optical microscopy is mostly used for detection of lipids in biological samples, we expected to record CARS signal generated by organic matrix in the urinary stones as well. However, no such signal was observed in the multimodal images. It has been shown that organic matrix (mainly lipids and proteins) may constitute at least 5 % of urinary stones' mass [178]. They have been identified by chemical methods and observed in stone cross-sections by immunohistochemical staining [179,180]. There might be two reasons why the organic matrix was not observed in the multimodal images: (I) the particles of organic matrix are too small and/or (II)

signal generated by the matrix is too weak to be recorded when epi-detection is used.

The results presented here confirm that different chemical constituents of urinary stones can be well discriminated in the multimodal images. One advantage of the method over the previously proposed FTIR microspectroscopy [26,181,182] is its speed - the images can be captured in less than an hour. In addition, high lateral resolution allows revealing hidden information about the microstructure of the stones. However, expensive and not widely commercialized equipment is at present required for the nonlinear optical microscopy and, therefore, this technique could hardly be immediately applied for routine analysis of urinary stones. On the other hand, imaging of selected stones can be performed in order to obtain relevant information about their growth and deliver useful insights in etiology and pathogenesis of urolithiasis.

2.4.6. Final remarks on vibrational spectroscopy of urinary stones

In this work, 403 human urinary stones were analyzed by vibrational spectroscopy methods. As presented in the results, different methods provide different information about the stones and complement each other. However, using all of them on all of the stones would be complicated and time consuming. Therefore, standardization, or a protocol, is necessary for adapting the multistage approach for each individual stone sample in such a way that questions related to the causes of urolithiasis and lithogenesis of the stone could be best answered. Based on the results obtained in this work, we describe such protocol (Fig. 28). It includes stone inspection by stereomicroscopy, choice of one or several vibrational

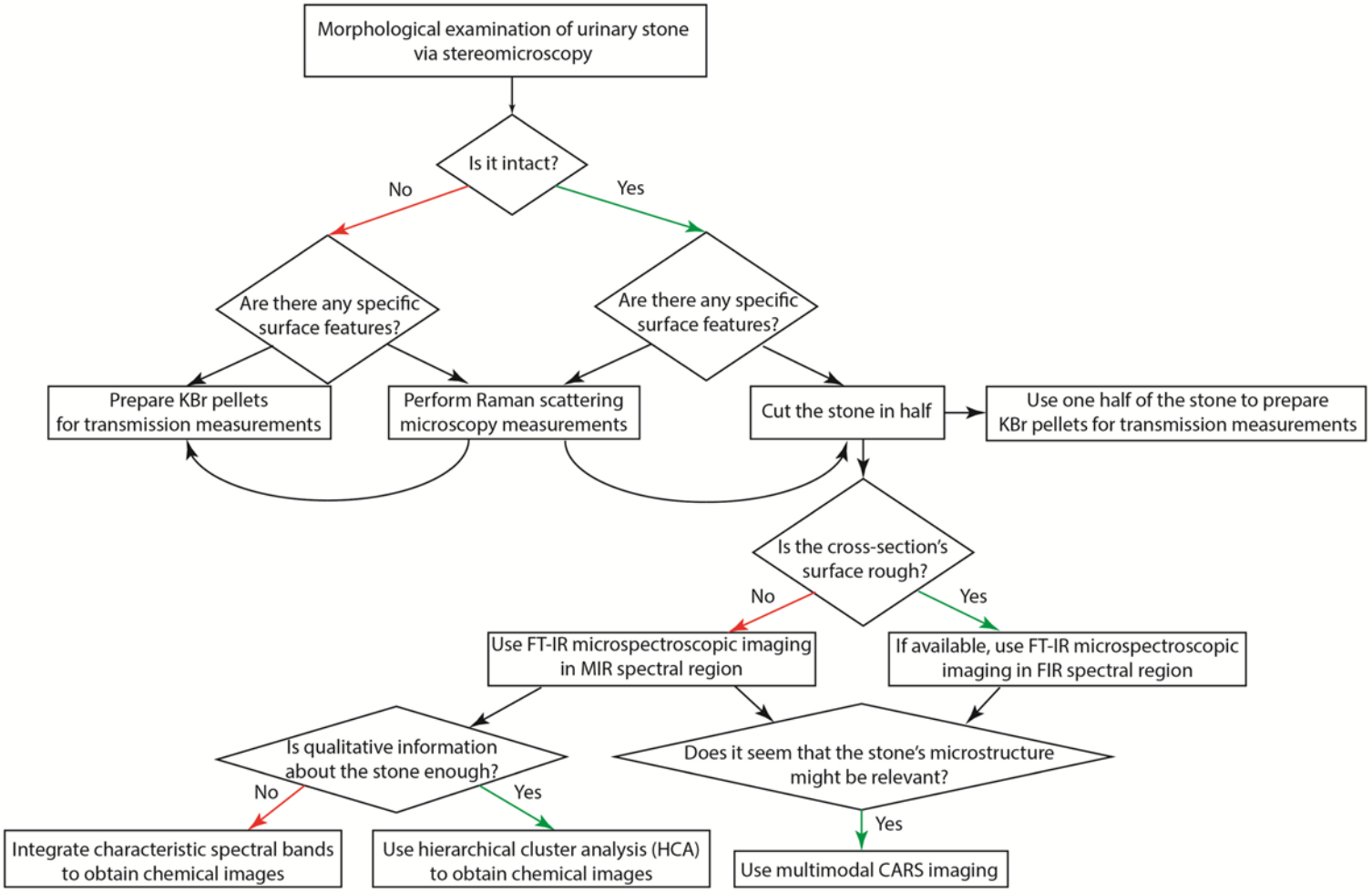

Fig. 28. Block scheme of a protocol for comprehensive urinary stone analysis

spectroscopy methods, spectral pre-processing and data analysis which finally allows collecting comprehensive data about the stone and deducing its etiology and lithogenesis.

Visual inspection of urinary stones provides valuable information about the type of the stone [117,144,145]. Moreover, it gives some clue on what path further analysis should take:

- If the stone is intact, its structure can be determined which can lead to lithogenesis hypothesis.
- If the surface of the stone has some specific features or domains of different morphology their chemical composition is determined by recording Raman scattering spectra.
- The stone is cross-sectioned. One half is used for IR chemical imaging while the second half is grinded and KBr/PE pellet samples are prepared for IR transmission analysis.
- Either MIR or FIR (if available) spectral region can be chosen for the imaging according to the size of the surface roughness of the stone.
- Chemical imaging according to the HCA results is easier to accomplish and should be used for high signal-to-noise spectra when no quantitative information is required; otherwise, chemical imaging should be done according to the integral intensities of characteristic spectral bands.
- If the IR chemical imaging is not sufficient to characterize the stone, nonlinear optical microscopy imaging is used for microstructural analysis.
- If the stone is broken during its removal procedure and its visual analysis reveals no distinct morphological features, the stone is grinded and KBr/PE pellet samples are prepared for IR transmission analysis. However, if debris of the stone has some specific features or domains of different morphology their chemical composition is determined by recording Raman scattering spectra prior the grinding.

This protocol allows obtaining comprehensive information about urinary stones. Assigning a stone to a specific type according to its morphology and chemical composition alone suggests an underlying disorder causing urolithiasis and aids in prescribing appropriate treatment to prevent recurrences [117]. Further information about the structure of the stone obtained from IR, Raman or nonlinear optical microscopy measurements provides hypothesis about the stone lithogenesis. Information obtained by use the methods can aid medics in understanding the urinary stone disease.

2.5. Urinary deposits: a hint of the stone formation

As mentioned above, an essential condition for the stone formation is oversaturation of urine – a condition which can subsequently lead to nucleation, crystal growth and aggregation. Examination of the small crystallites excreted with the urine is used as a diagnostic method for urolithiasis and can indicate formation of the urinary stone in the urinary tract. On the other hand, the crystallites are found both in healthy and lithogenic patients. The factors that help identify the latter are crystal size, shape and chemical composition. It has been shown that urinary crystals of lithogenic patients are relatively large, contain sharp edges rather than blunt edges and are more likely to aggregate [177,183]. In addition, the higher amount of, for instance, COM in respect to COD can also suggest the stone formation.

Early discovery and identification of the formed urinary crystals in the urine of high risk urolithiasis patients could be crucial for taking appropriate preventive measures that inhibit further urinary stone formation. This is particularly true in cases of recurrent stones. Optical microscopy is currently the only method used to analyze the urinary crystals routinely [184]. They are identified by their morphology, crystal birefringence (the microscope must be equipped with polarizers) and prior knowledge of urine pH. However, this method is not reliable to determine chemical composition of “atypical” (crystallites of varied crystalline appearance or materials rarely found in urinary deposits), amorphous deposits and/or crystal clusters.

As already mentioned above, optical microscopy is currently the only method used to analyze the urinary crystals routinely [184]. FT-IR microscopy was first shown to be suitable for chemical composition analysis of urinary crystals in 1991 by Daudon et al. [185]. It was demonstrated that

the technique is suitable to differentiate the crystals and identify deposits of heterogeneous or unusual (e.g., drug metabolites) composition. In the subsequent paper, they proposed combining IR absorption spectroscopy with KBr pellet technique instead of using IR microscopy [186]. Combining the spectral results obtained from analysis of urinary deposits and kidney stones with the results obtained by optical microscopy of the deposits, the researchers found 97.3 % correlation between stone type and urinary crystals type. These studies were limited by the amount of sample required for the KBr pellet technique. Later on, the researchers' group published a paper where IR microscopy was used to analyze "atypical" urinary crystals which could not be identified by combined approach of morphological, crystal birefringence and urine pH analysis [187]; thus, IR microscopy was proposed as a complementary technique to the existing routine analysis methods.

The mentioned IR absorption spectroscopy methods have not yet become routine. This is mainly reasoned by the fact, that IR microscopy used for the analysis requires sophisticated and expensive equipment while IR absorption spectroscopy combined with KBr pellet technique for sample preparation – a considerable amount of sample.

2.6. Infrared spectroscopic analysis of urinary deposits: experimental details

2.6.1. Sample preparation of urinary deposits

Urine samples from 68 healthy individuals (reference group), 151 patients in risk of urolithiasis group and 76 urolithiasis patients were collected at Vilnius University Hospital Santariskiu Clinics or Faculty of Medicine, Vilnius University. Urine samples from the urolithiasis patients were collected just before the kidney stone removal procedure. Morning urine was collected from the rest of the patients. The samples were centrifuged to separate the urinary deposits from the whole urine volume. The centrifuged urine was placed on an ashless paper filter (Whatman 542) and left for 24 hours to dry. We chose filters with 2.7 μm particle retention to separate the crystals suitable for investigation. The urinary crystals were collected from the surface of the filter and transferred onto an optical window transparent in the IR spectral region (CaF_2 or ZnSe). Most of deposits, crystals or crystal clusters were too thick to record appropriate transmission spectra for qualitative analysis. For this reason, they were squeezed between two IR transparent optical windows and crushed until suitable sample thickness (approx. 10–20 μm) was obtained. One of the optical windows was then removed for the IR radiation to reach the sample directly. The damage of the crushing to the optical windows was either not observed or minor.

2.6.2. FTIR transmission microspectroscopy of urinary deposits

IR absorption spectra were obtained using IR microscope 'Hyperion 3000' (Bruker Optik GmbH, Ettlingen, Germany) equipped with a single element MCT detector and combined with Vertex 70 spectrometer (Bruker Optik GmbH, Ettlingen, Germany). A 15x/0.4 objective was used. Knife edge aperture was set according to the sample size in order to avoid stray light. The

spectra of crystals smaller than 10×10 μm could not be recorded due to too low signal reaching the detector. The spectra were recorded in 4000-650 cm^{-1} spectral range with spectral resolution of 4 cm^{-1}. One hundred and twenty eight interferograms were averaged for one resultant spectrum of each point and the result Fourier transformed into a spectrum applying Blackmann-Harris 3 apodization function and zero filling factor 2.

Either the visible mode of the IR microscope or stereo microscope (Stemi 2000C with AxioCam ERcSs video camera, Carl Zeiss, Oberkochen, Germany) was used for the morphological investigation of the urinary deposits before the crushing.

2.6.3. FTIR ATR spectroscopy of urinary deposits

IR ATR spectra were recorded using either a Ge ATR 20× objective of the IR microscope described previously (’Hyperion 3000’ from Bruker Optik GmbH, Ettlingen, Germany) or a small (22×30 cm) portable IR spectrometer Alpha with diamond ATR accessory (Bruker Optik GmbH, Ettlingen, Germany). All the ATR spectra were recorded in 600-4000 cm^{-1} spectral range with spectral resolution of 4 cm^{-1}. One hundred and twenty eight interferograms were averaged for one resultant spectrum of each point and the result Fourier transformed into a spectrum applying Blackmann-Harris 3 apodization function and zero filling factor 2.

2.7. Analysis of urinary deposits: results and discussion

Thus far, prospects of applying vibrational spectroscopy methods for determining underlying disorders of urolithiasis and lithogenesis of urinary stones after they have formed and been removed from human organism were discussed. However, urolithiasis is a painful disorder in many cases requiring invasive treatment which significantly affects patient's quality of life. Therefore, early discovery and identification of urinary crystals in urine could be crucial for taking appropriate preventive measures and inhibiting further urinary stone formation in high risk urolithiasis patients. In addition, it could aid medics in prescribing non-invasive treatment for the already formed stones. Currently used optical microscopy is unreliable to determine chemical composition of "atypical" (crystallites of varied crystalline appearance or materials rarely found in urinary deposits), amorphous deposits and/or crystal

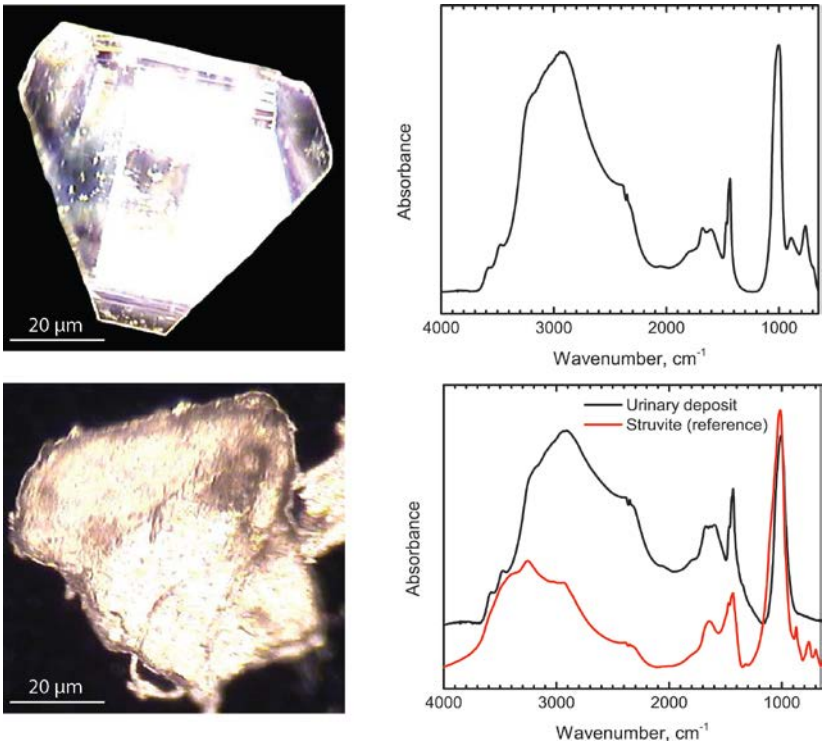

Fig. 29. Optical images and corresponding IR absorption spectra of urinary deposits constituted from struvite.

clusters. For these reasons, urinary deposits from healthy individuals (reference group), risk of urolithiasis group and urolithiasis patients were analyzed in this work by means of IR (micro)spectroscopy.

When observed in the visible light mode of the IR microscope, urinary deposits were found either as crystals having a regular morphological structure, polycrystalline clusters or amorphous formations. Optical images of urinary deposits of two different patients and their IR absorption spectra are presented in Figure 29. While one of the samples has a crystalline structure, the other is irregularly shaped. However, both of them are constituted from struvite as deduced from the spectra. This confirms the fact that visual inspection is not a reliable method for urinary deposit analysis and other methods for this purpose should be sought.

Three different approaches to record IR absorption spectra were applied for the urinary deposit analysis: IR transmission microspectroscopy, IR ATR microspectroscopy (further referred to as micro-ATR) and IR ATR

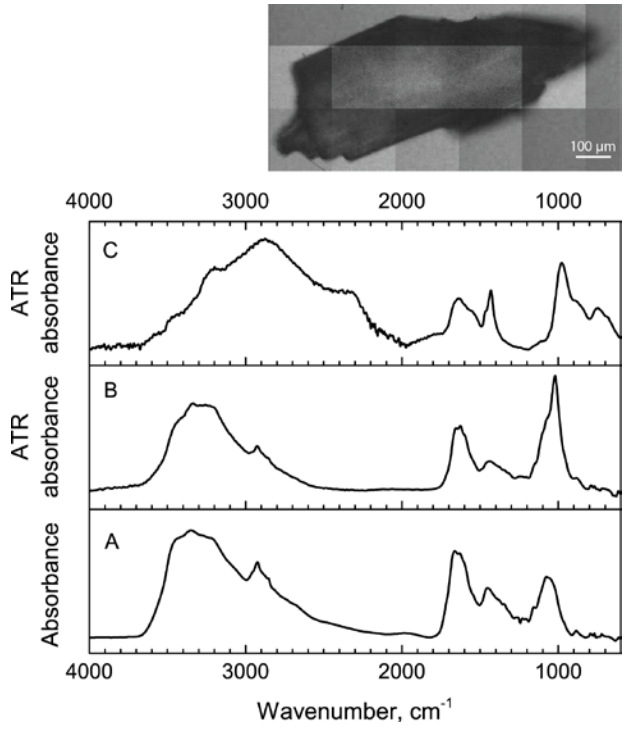

Fig. 30. Optical image of urinary deposit constituted from struvite and organic matrix and corresponding IR absorption (A), micro-ATR (B) and macro-ATR (C) spectra.

spectroscopy (further referred to as macro-ATR). Qualitative analysis of the urinary deposits was performed by comparing the spectra of the samples and synthetic components. Whichever IR spectroscopic method was used, chemical composition of both single- and multi-component samples could be determined from the recorded spectra. Typical (crystalline deposits constituted of minerals usually found in urinary stones) and “atypical” (agglomerations of crystallites, amorphous formations and deposits constituted from substances rarely found in urinary stones) deposits could be identified as well. Figure 30 shows optical image and IR transmission, IR macro-ATR and IR micro-ATR spectra of urinary deposit constituted from struvite and organic matrix. To obtain the transmission spectrum (Fig. 30 A), sample thickness should not exceed 10 μm. This was accomplished by crushing the urinary deposit between two optical windows. The spectrum of the crushed deposit has a high signal-to-noise ratio and is suitable for spectral analysis. However, desirable thickness of the deposits is not always obtained through crushing and their absorbance is saturated (Fig. 31). Note that the transmittance scale may not reach value of 0 even if the spectrum is clearly saturated. This is reasoned by the stray light reaching the detector. Spectral

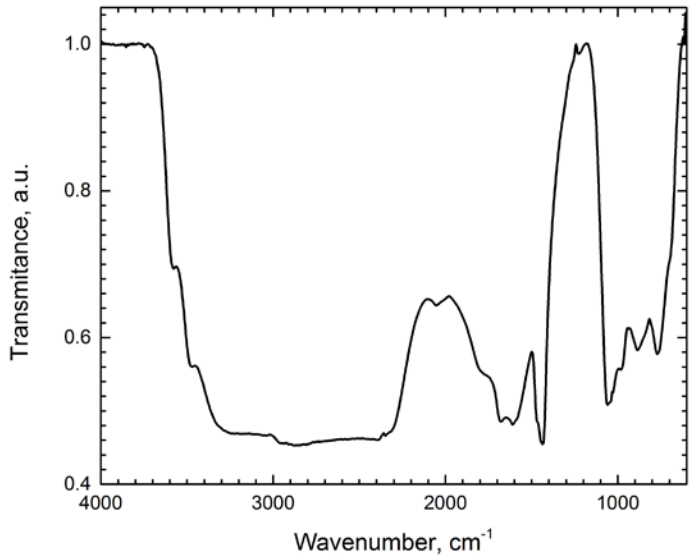

Fig. 31. Saturated IR transmission spectrum of urinary deposit constituted from struvite.

analysis of such samples is difficult or impossible. In addition, crushing the deposits causes damage to the soft ZnSe. Use of harder materials such as CaF_2 is impossible due to its strong absorption below 900 cm^{-1}. Spectral bands in this spectral region often allow identifying the chemical composition of urinary deposits. Moving the crushed deposits from one optical window to the other might cause sample loss.

Using ATR technique eliminates the requirement of sample thickness. In turn, additional treatment is not needed for the urinary deposits prior the measurements. Figure 30 B, C shows macro- and micro-ATR spectra of the deposits. They are mostly consistent with the IR absorption spectrum (Fig. 30 A) and allow deducing chemical composition of the deposits. However, some differences between the spectra are observed: the macro-ATR spectrum (measured first) can be assigned to pure struvite; no spectral bands characteristic to the organic matrix are visible. During the measurement of the macro-ATR spectrum, the deposit was pressed to the diamond ATR element with a stainless steel handle and crushed. Subsequently, the crushed deposit was transferred from the element onto CaF_2 optical window for the micro-ATR and transmission measurements. Some sample was inevitably lost during the transfer which caused changes observed in the micro-ATR and IR absorption spectra, where spectral bands characteristic to the organic matrix are visible and overlap with the bands of struvite. Signal-to-noise ratio of the macro-ATR spectrum is lower as compared to the one recorded by the micro-ATR. This is due to stray light reaching the detector as the small deposits do not cover the whole surface of the macro-ATR element (2×2 mm). The coverage would require large amount of the deposits which was rarely observed even in the urine samples of urolithiasis patients. Despite the lower signal-to noise ratio, however, the spectra are of sufficient quality for qualitative analysis.

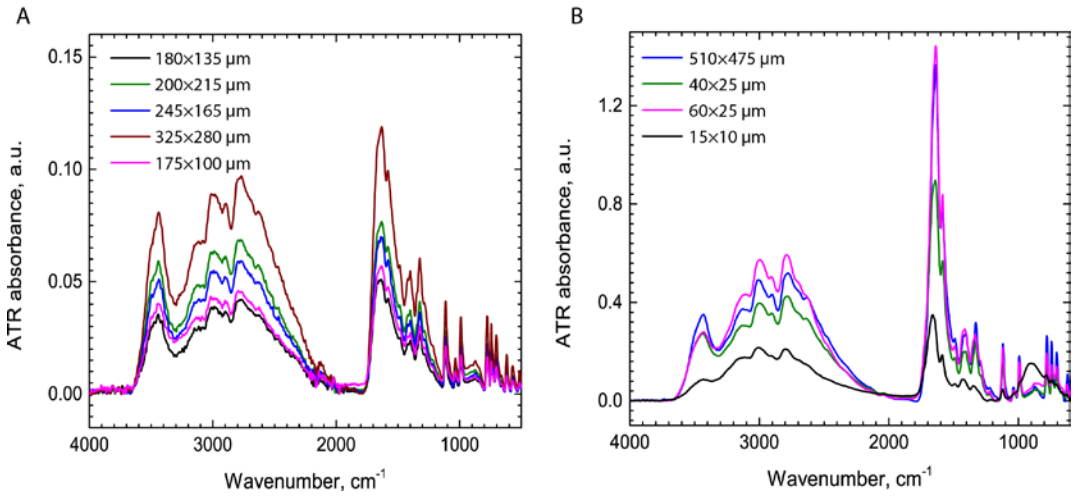

Fig. 32. Macro-ATR (A) and micro-ATR (B) spectra of urinary deposits of various sizes constituted from uric acid dihydrate.

The urinary deposits found in the urine samples varied in size with the smallest ones being less than 10 µm (smaller ones could not be picked up from the filter or were filtered through it) and the largest ones – more than 300 µm in size. ATR spectra of urinary deposits of various sizes and constituted from uric acid are presented in Figure 32. It can be seen again that superior results are provided by the micro-ATR (Fig. 32 B) which allows recording high signal-to noise spectra of deposits as small as 15×10 µm in size. However, this method requires sophisticated and expensive equipment and a trained spectroscopist to measure the spectra. It could hardly be implemented in a clinical laboratory for routine analysis. On the other hand, portable IR spectrometer Alpha with macro-ATR unit could be used for this purpose. As long as the deposits are larger than 100×100 µm, their spectra can be recorded by means of macro-ATR (Fig. 32 A). It has been shown that urinary deposits of urolithiasis patients are both larger and have wider size distribution than healthy controls [177,183]. In addition, they are more likely to aggregate.

In this work, 68 samples of healthy controls were investigated. Spectra of only 23 samples were recorded as others did not contain any

deposits or they were too small to be removed from the filter. The analyzed deposits were mainly (18 samples) constituted from uric acid dihydrate (an unstable phase of uric acid) and proteins. COM was also identified in 3 of these samples. Surprisingly, struvite was found in 4 of the urine samples of healthy controls. Growth of struvite crystals in urinary tract is related to bacterial infection and, therefore, was unexpected to be found in these samples. One sample was found to be constituted from calcite. The urinary deposits in this group were found to be small and did not exceed size of 270 μm.

The risk for urolithiasis group included 151 urine samples. Only 24 of them did not contain any deposits or they were too small to be removed from the filter. Similarly as in the case of healthy controls, chemical composition of most of the analyzed samples was deduced to be either uric acid dihydrate or proteins or mixture of these two components. Struvite, brushite and COM were also found. However, the main difference between these samples and the samples of healthy controls was the size of the deposits. Formations of up to 800 μm in size were found in the risk for urolithiasis group samples. It is possible, that these formations aggregated in the test-tubes after the samples were taken from the patients. Either way, increased rate of aggregation of urinary deposits in urine suggests increased risk for urolithiasis.

Finally, we compared chemical composition of urinary deposits and urinary stones obtained from the same urolithiasis patients. In 73 % of the cases of the 76 patients investigated, at least one common component was found both in the deposits and in the stones. In 41 % of those cases, a complete match of chemical composition was observed. For calcium oxalate stones, however, the samples exhibited absolute match only in 27 % of the cases. Protein formations were mostly found instead. In addition, a miss-match of phosphate types found in the calcium oxalate stones and the

corresponding deposits was observed. This can be explained by the fact that different phosphates form from other phosphatic precursors in urine when different pH or ion concentration conditions are met [188].

For uric acid stones, absolute correlation of chemical composition of the stones and deposits was observed for 71 % of samples. This implies that presence of uric acid deposits in urine is a precursor of a urinary stone formation. Of note, small uric acid crystallites have been found in urine of healthy people as well [189]. This is due to low solubility of uric acid in aqueous solutions, particularly under conditions of increased acidity. Therefore, determining size of urinary deposits might be extremely relevant in case of uric acid.

Phosphate (struvite, apatite and brushite) urinary stones are rare and only 6 of them were included in this study of urinary deposits. In 4 of the cases, correlation between the chemical composition of the deposits and the stones was found. As in the case of uric acid stones, presence of phosphate deposits could signal the phosphate stone formation in the urinary tract. However, more phosphate stones should be investigated for reliable results.

Some of the components, for example, uric acid dihydrate, found in the urinary deposits were not found in any of the stones. This can be explained by the fact that dihydrate form of uric acid is highly unstable and turns to uric acid (anhydrous) during formation of the stones [190]. In addition, components rarely found in urinary stones such as drug metabolites or calcite could be identified in the urinary deposits. While these components rarely constitute urinary stones themselves, they can influence the processes of stone formation; thus, their identification is relevant and may provide additional information about underlying causes of urolithiasis.

2.8. Vibrational spectroscopy analysis of urinary stones and urinary deposits: conclusions

1. Morphological examination of urinary stones provided both valuable information about their growth processes and some clue on what path further vibrational spectroscopic analysis should take. Specific morphological features suggesting last stages of stones' growth were additionally analyzed by Raman scattering microscopy which revealed chemical composition of minor components in urinary stones such as COD, sucrose or blood.

2. Comprehensive chemical analysis of urinary stones by means of IR spectroscopy is only possible when both MIR and FIR radiation is used. After performing IR spectroscopic analysis of 403 urinary stones, distribution according to their type was determined: calcium oxalate stones – 61 %, uric acid stones – 26 %, struvite stones – 10 %, brushite stones - 2 % and apatite stones - 1 %.

3. Specular reflection microspectroscopic imaging of urinary stones in MIR spectral region can be effectively used only if (I) modification of the experimental spectra – the subtraction of the diffuse reflection component – is performed prior application of KKT to convert Reststrahlen spectral bands to absorbance bands or (II) HCA is used to group the spectra and create the chemical images.

4. Specular reflection microspectroscopic imaging of urinary stones in FIR spectral region allows suppressing influence of diffuse reflection. KKT can

be directly used to convert Reststrahlen spectral bands to absorbance bands without any additional pre-processing.

5. Epi-detected nonlinear optical microscopy, when CARS, TPEF and SHG signals are recorded, can be used to determine chemical composition and microstructure of urinary stones. Different constituents of urinary stones can be well discriminated according to the optical signal they generate.

6. IR transmission microspectroscopy, macro-ATR and micro-ATR spectroscopic methods were shown to be suitable to determine chemical composition of atypical crystal, poly-crystal and amorphous urinary deposits and are superior to the conventional optical microscopy. The fact that high quality macro-ATR spectra of urinary deposits larger than 100 μm could be recorded and that the method does not require sophisticated equipment, makes it attractive for applications in clinical practice.

7. High correlation between chemical composition of urinary deposits and urinary stones obtained from the same urolithiasis patients was observed. At least one common component was found both in the deposits and in the stones in 73 % of the cases of the 76 patients investigated. In 41 % of those cases, a complete match of chemical composition was observed.

Chapter 3 Vibrational spectroscopy analysis of biological fluids

3.1. Analysis of biological fluids for disease diagnosis

Bodily fluids, such as blood, urine, saliva, tears or extracellular fluid, are biological fluids produced in human organism. They are aqueous solutions of proteins, lipids, various metabolites, electrolytes and other compounds. Bodily fluids are often used for diagnostic purposes as they contain important biomarkers specific to particular disorders. As compared to analysis of tissue biopsies, such testing is minimally or non-invasive, sample collection, processing and storage is simple and its cost is low. Microscopic examination, proteomic, chemical or microbiological analysis can be performed once fluid samples are obtained [191].

3.1.1. Detection of metabolites in bodily fluids

The main disadvantage of testing bodily fluids is relatively low concentrations of analytes which leads to poor sensitivity. Moreover, detection of specific biomarkers is often complicated due to interference of all the constituents present in the bodily fluids. Despite these shortcomings, blood and urine screening is a routine procedure in diagnostics. Biomarkers of various infections, genetic disorders or organ dysfunction are well known [192]. For example, creatinine levels in blood serum and plasma are indicative of impaired kidney function; glucose – of diabetes; prostate-specific antigen – of prostate cancer, etc. [15]. Still, discovery of new biomarkers remain to be challenging, mostly, due to normally occurring variations of concentrations and molecular structures of the same compound from individual to individual. New and improved methods for the more precise biomarker detection are continuously sought as well.

Vibrational spectroscopy methods have been extensively applied for analysis of bodily fluids [15,193,11,34,194]. While both IR absorption and Raman scattering spectroscopy provide useful information about presence of

certain metabolites, proteins and drugs and their concentrations, they also have disadvantages that prevent them from being used as routine diagnostic methods. For the IR absorption spectroscopy it is contribution of water absorption to the spectra; for the Raman scattering spectroscopy – poor signal-to-noise ratio caused by low sample concentrations and fluorescence background frequently occurring in bio-samples. To overcome these disadvantages, ways to develop and improve data analysis and to find new approaches to sample preparation have been sought [23,24,195,196].

SERS spectroscopy has been increasingly proposed as a method of choice for disease diagnosis and prevention as well [65–68]. Advantages of SERS over conventional Raman scattering spectroscopy includes significantly increased signal which allows detection of trace amounts of substances in samples and fluorescence quenching [197,198]. In addition, high sensitivity of the method and ease of use provided by emergence of portable hand-held Raman scattering spectrometers would allow development of point-of-care analysis systems. However, for SERS to be used routinely, further studies of selectivity and reproducibility are still required.

3.1.2. Uric acid

Uric acid ($C_5H_4N_4O_3$) is an end product of purine metabolism in human organism. Most of it (approx. 70 %) is disposed through the kidneys as a constituent of urine; the other part is recirculated into the blood system and acts as an antioxidant together with vitamin C [199–201]. Normally, uric acid concentration in blood ranges from 20 mM to 45 mM [202]; in urine - from 100 mM to 600 mM per 24 h [203]. Its elevated or decreased levels in either of the bodily fluids can suggest disorders such as gout, pre-eclamsia or cardiovascular disease [204–206]. Uric acid analysis in urine is also performed in order to evaluate kidney function [207].

Various methods have been used for detection of uric acid: enzymatic method, differential spectrophotometry, liquid chromatography, etc. [204,208–210]. However, these methods either lack sensitivity when low concentrations of the sample molecules need to be detected or require sophisticated, bulky and expensive equipment.

Electrochemical SERS (e-SERS) was proposed for detection of uric acid in aqueous solutions as well as in urine stimulant [162,211]. The method was capable of detecting uric acid concentrations down to 0.1 mM and little interference from other components was observed in the urine stimulant. However, the use of metal nanoparticle (NP) colloids remains the most common approach for obtaining the Raman signal enhancement. That is mainly due to simplicity of preparation, low costs and high enhancement factor (EF) of the colloidal SERS substrates. In addition, different techniques can be used for colloid preparation in order to obtain NPs of specific shapes and sizes. This allows shifting the surface plasmon resonance (SPR) maximum and adapting it to the particular excitation frequency. It has been shown that adsorption of the analyte molecules also depends on the shape of the NPs [212]. To the best of our knowledge, colloidal SERS approach has not been used for uric acid detection yet.

Several types of colloidal suspensions of gold (Au) and silver (Ag) NPs were used in a study of blood serum and plasma in search of a sensing method for metabolic profiling [213]. It was discovered, that, once the proteins were eliminated from serum, and when employing NIR (785 nm) excitation in combination with Ag NPs, intense and repeatable SERS spectra could be recorded. However, the spectra were dominated by only two metabolite species, namely, uric acid and hypoxanthine. Although the study demonstrated that SERS spectroscopy is hardly suitable for the metabolic profiling, it also showed that selective adsorption and intense SERS spectra of uric acid can be obtained in the analyzed biofluids.

The results of the earlier studies imply that colloidal SERS has potential to be employed as an efficient method for detection of uric acid in various bodily fluids.

3.2. Uric acid detection in solution by means of SERS: experimental details

3.2.1. Preparation and characterization of Ag NPs colloids

Three types of Ag NPs colloids were used in this study: (I) citrate reduced (mainly spherical), (II) hydroxylamine hydrochloride reduced (spherical) and (III) Ag seed-catalyzed ascorbic acid reduced (prisms). Trisodium citrate (Merck), silver nitrate (Merck), hydroxylamine hydrochloride (Thermo Scientific), PSSS (Sigma-Aldrich), ascorbic acid (Sigma-Aldrich) and 2% sodium hydroxide solution (Thermo Scientific) were purchased and used as received.

Citrate reduced Ag NPs colloid was prepared by using Lee-Meisel method [214]. Briefly, 9 mg of silver nitrate is added to 50 ml of DI water heated to 45-50^0 C. The solution is then brought up to boiling point and 1 ml of 1 % sodium citrate tribasic dihydrate solution is added to stabilize the NPs. The colloid is left boiling for one hour (the vial is covered with Al foil to prevent water from evaporating) and then is placed in an ice bath for rapid cooling. Vigorous stirring was kept during the whole process.

For preparation of hydroxylamine hydrochloride reduced Ag NPs colloid a method described by Leopold-Lendl was used [215]. While stirring, silver nitrate solution (17 mg of $AgNO_3$ diluted in 10 ml of H_2O) was rapidly added into hydroxylamine hydrochloride solution (9.4 mg of $NH_2OH{\cdot}HCl$ diluted in 90 ml of H_2O) containing 0.5 ml of 2 % NaOH solution. The reaction was completed in several seconds and yellowish-grayish solution was obtained.

The preparation of Ag nanoprism colloid is described by Aherne et al. [216]. For seed solution, 5 ml of 2.5 mM sodium citrate tribasic dihydrate, 0.25 mL of 500 mg/l PSSS and 0.3 ml of 10 mM sodium borohydrate were mixed while stirring. Then, 5 ml of 0.5 mM silver nitrate solution is dropwise

added to the mixture. Under formation of the seed particles, yellow color of the solution is obtained. For growth of the Ag nanoprism NPs, 75 µl of 10 mM ascorbic acid solution is added to 5 ml of DI water. Then, 25 µl of the seed solution is introduced. Three ml of 0.5 mM silver nitrate solution is dropwise added to the mixture which causes change in the color of the solution from colorless to dark blue. To stabilize the NPs, 0.5 ml of 25 mM sodium citrate tribasic dihydrate solution is added. Vigorous stirring was kept during the whole process.

The prepared colloids were centrifuged for 30 min. (RCF=10400×g) in order to achieve higher concentration of the Ag NPs. For each 100 ml of colloidal solution approximately 20 ml of the concentrate was obtained.

For characterization of the colloidal suspensions, UV-VIS spectra (spectral range 250-800 nm (250-1300 nm for the Ag nanoprism colloid), spectral resolution 5 nm) were recorded by Lambda 1050 spectrometer (Perkin-Elmer) equipped with two light sources (deuterium lamp and halogen lamp) and three detectors (photomultiplier tube, InGaAs and PbS). The spectra were recorded prior and after the centrifugation in order to ensure that the properties of the colloids remained unaltered. The spectra were normalized for analysis. Additionally, transmission electron micrographs of the dried colloids were recorded with transmission electron microscope Libra 200 (Carl Zeiss, Oberkochen, Germany) in Leibniz Institute for Polymer Research, Dresden, Germany.

3.2.2. Uric acid sample preparation for SERS measurements

Uric acid powder was purchased from Sigma-Aldrich and used as received. Its aqueous solutions of various concentrations were prepared by diluting a 1×10^{-3} M stock solution with DI water. The latter was prepared by adding 16,8 mg of uric acid into 98 ml of DI water. Two ml of 2 % NaOH solution was added in order to dissolve the uric acid completely. Uric acid

solution of 65 mM concentration was prepared as well by adding 1 mg of uric acid powder into mixture of 98 ml of DI water and 2 ml 2 % NaOH. Raman spectrum of this sample was used in enhancement factor calculations.

The substrates for the SERS measurements were prepared by dropping 23 µl of Ag NP colloid onto Al_2O_3 surface. The latter was obtained by vacuum deposition of 150 nm Al layer on glass slides (pre-cleaned in an ultrasonic bath by subsequent immersion into water, acetone, isopropanol and methanol for 5 min. each). To form the oxide layer, the slides were kept in an atmosphere for 24 h. Nine colloidal drops were dried in a closed environment (chamber of 23 cm × 8 cm × 9 cm dimensions) at room temperature (23^0 C). A hygrometer was placed in the box to read out humidity data. Subsequently, 23 µl of uric acid solution was dropped onto the prepared substrate and left to dry under the same conditions. The prepared samples were rinsed with DI water and dried.

3.2.3. Raman and SERS measurements of uric acid aqueous solutions

Raman and SERS spectra (4000-70 cm^{-1}) were recorded using Fourier transform (FT) Raman spectrometer MultiRAM (Bruker Optik GmbH, Ettlingen, Germany) equipped with Nd:YAG laser (1064 nm) and liquid-nitrogen-cooled Ge diode detector. Gold plated mirror objective (focal length – 33 mm) was used. Diameter of the laser beam at its focal point is 100 µm. To obtain the spectra, 128 interferograms were averaged and the result was Fourier transformed by applying Blackman-Harris 3-Term apodization function and zero filling factor of 2. Spectral resolution of 4 cm^{-1} was used. Laser power was set to 100 mW. The uniformity of the NPs films was checked for by recording SERS spectra in 19 positions (approximately every 300 µm) across the diameter of the dried samples. Otherwise, five to seven spectra were recorded in randomly chosen points of each dried droplet. The recorded SERS spectra were cut at 1750 cm^{-1} as the large wavenumber region did not contain

significant spectral information. Both SERS and Raman spectra were baseline corrected (rubber band baseline correction).

3.2.4. Theoretical calculations of uric acid molecule

All DFT calculations were performed using Gaussian 09 software [217]. Visualization of the molecules was performed with GaussView [218]. The geometries and normal vibrational modes of three most stabile tautomers of uric acid, and three most stable anions [219] adsorbed on five-atom silver cluster were calculated using B3LYP functional and LANL2DZ basis set. Two different environments - vacuum and aqueous solvent -were considered in the calculations. The geometry of the Ag cluster was pre-optimized using the same conditions and kept "frozen" during the further calculations. Various orientations of the molecules in respect to the silver structure were considered and only the most stable structures are presented herein. In order to achieve agreement between the calculated harmonic frequencies and the experimental data, scaling factor was applied for the calculated bands' positions.

3.3. SERS spectroscopy of metabolites in solution: results and discussion

In this study we applied FT-Raman system with 1064 nm excitation for detection of uric acid in aqueous solutions by means of colloidal SERS. The NIR excitation ensured low or even absent fluorescence background in the SERS spectra. However, due to strong water absorption in this spectral region (third overtone of OH stretching vibration), the ability to measure wet samples was limited and the sample drying procedure was applied. Normally, drying a drop of colloidal solution leaves a ring-like structure of the colloidal particles – a "coffee ring" [220,221]. In SERS, high signal enhancement can be reached in the "coffee-ring" area; however, no reproducibility of the enhancement factor can be expected [222]. Recently, many studies have been carried out in order to understand and avoid formation of the ring [220,223–227]. For example, Y. Xie et al. described a method which allows reproducibly obtaining self-assembled monolayers of Au nanorods by controlling humidity and temperature of the drying environment [228]. Furthermore, it has been determined that wettability and temperature of the substrate on which the colloid drop is casted has great influence on how the NPs settle [229–231]. All of these factors should be considered when preparing SERS substrates by drying the metal NPs colloids.

In this work we compared enhancement effects of various drop-dried colloidal substrates with differently shaped silver nanoparticles and found optimal experimental conditions for detection of uric acid in aqueous solutions by means of SERS. Assignment of the SERS spectral bands was performed by means of density functional theory (DFT) calculations.

3.3.1. Evaluation of the prepared SERS substrates

Normalized UV-VIS spectra of the three Ag NPs colloids are presented in Figure 33. The absorption peaks arising from surface plasmon resonance of the NPs in the Lee-Meisel, Leopold-Lendl and Aherne *et al*. colloids are located at 428 nm (HWHM=188 nm), 411 nm (HWHM=84 nm) and 788 nm (HWHM=301 nm) respectively. The positions of the bands are determined both by the shape and size of the nanoparticles while the widths – by their size distribution [214–216,232]. In this case, diameter of the spherical Ag nanoparticles in the Lee-Meisel and Leopold-Lendl colloids was predicted to be approximately 30 - 80 nm while the edge length of the Ag nanoprisms in the Aherne *et al.* colloid – 40 - 60 nm. This was confirmed by recording and inspecting transmission electron micrographs of the dried colloids (refer to Fig. AIV-1 (Appendix IV)). The normalized UV-VIS spectra of the concentrated colloids remain the same implying that the centrifugation does not affect the properties of the nanoparticles (refer to Fig. AIV-2 (Appendix IV)). When preparing different batches of the colloids, 12-20 nm

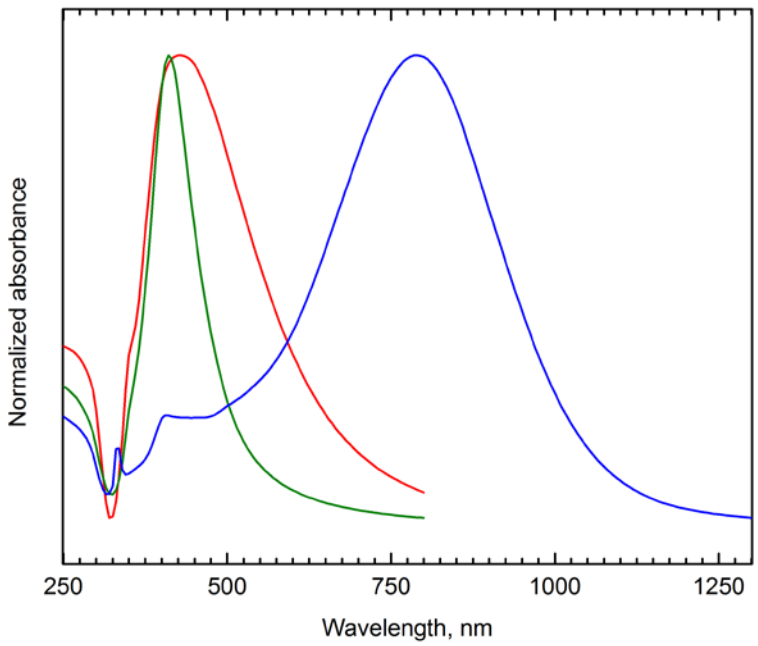

Fig. 33. UV-VIS spectra of Lee-Meisel (red), Leopold-Lendl (green) and Aherne et al. (blue) colloids.

(up to 107 nm for the Aherne *et al*. colloids) deviation of the SPR peak position was observed.

The colloids were drop-dried in order to prepare SERS substrates suitable for the measurements with NIR (1064 nm) excitation. In preparing of the substrates much effort was put to avoid the “coffee-ring” formation and achieve uniform layering of the NPs. Aluminum oxide was chosen as a surface to dry the colloids on. It has lower wettability than the commonly used glass which results in collecting of NPs in smaller area [229], however, initial pinning still takes place (pinning is generally not observed on highly hydrophobic surfaces) and no secondary rings of NPs aggregates form while drying [230]. In addition, the velocity of the flow that causes the NPs to migrate to the edge and form the “coffee-ring” is smaller in the drops with larger contact angles, i.e., drops on hydrophobic surfaces [233]. The drops were dried at room temperature in a closed chamber. The initial humidity of the chamber was 29 % as determined by the air conditioning in the laboratory room. Initially, fast evaporation of the drops takes place in the closed

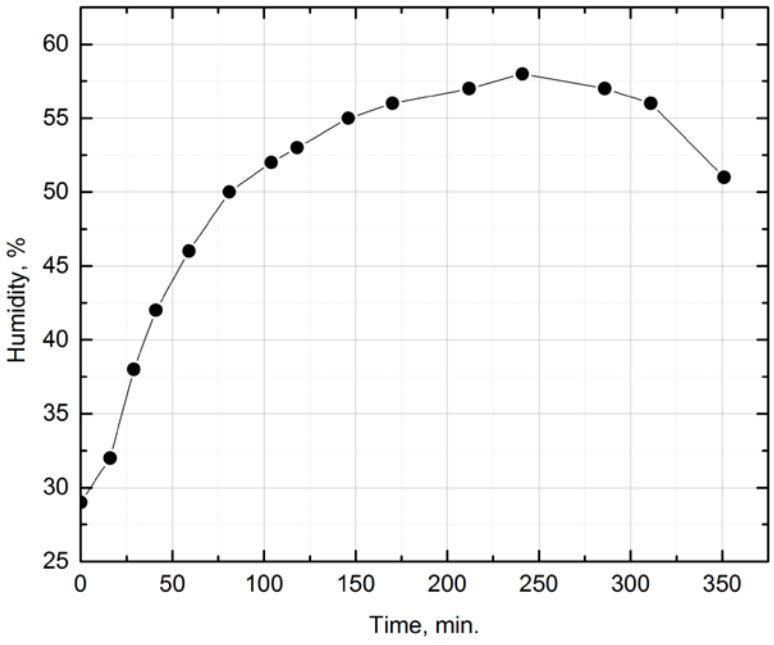

Fig. 34. Gradient of humidity during drying of 9 colloidal drops in a closed chamber of 23 cm × 8 cm × 9 cm dimensions.

chamber and causes pinning of the drops' edges [228]. Subsequently, the humidity rises and the rate of the evaporation decreases causing near-equilibrium evaporation processes [228]. Such slow evaporation prevents many of the NPs from migrating to the edge and agglomerating. The gradient of the humidity during the process is presented in Figure 34. Drying at room temperature also contributes to the formation of nearly uniform coverage of base area of the drops [231].

The images of the dried drops are presented in Figure 35 A. It can be seen that on the edge of the Lee-Meisel colloidal drop there is a thin ring

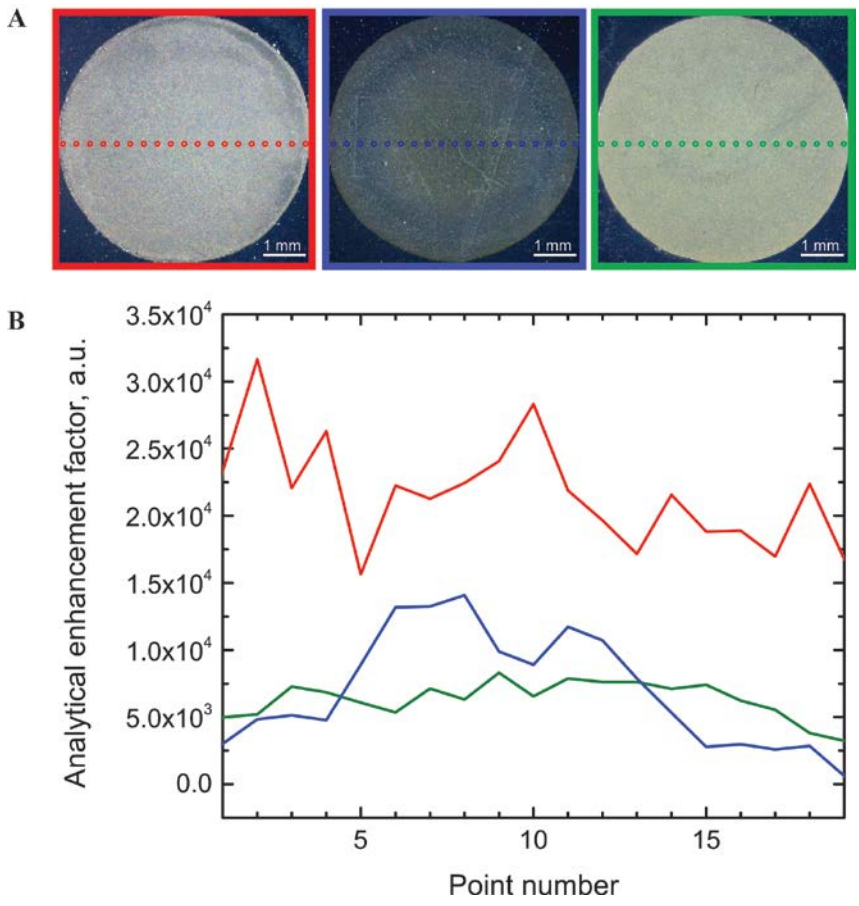

Fig. 35. (A) Images of the dried colloidal circularly shaped drops (from the left to right): Lee-Meisel, Aherne *et al*., Leopold-Lendl; (B) Profiles of SERS enhancement factor distribution across the drops: red – Lee-Meisel, blue – Aherne *et al*., green – Leopold-Lendl colloid.

of silver agglomerates. These agglomerates are already in micrometer scale which means that they are washed away during rinsing of the substrates with distilled water and/or provide no enhancement effect. The rest of the drop area appears nearly uniformly covered with the NPs, similarly as the Leopold-Lendl and the Aherne *et al*. dried colloidal drops. To check the uniformity of the NPs film, SERS spectra were recorded in 19 positions (approximately every 300 µm) across the diameter of the dried samples. It is expected that formation of the "coffee-ring" would reason stronger SERS signal on the edges of the samples. A graph of analytical enhancement factors (AEFs) of the SERS spectra in each measurement position is presented in Figure 35 B. They were calculated as described by E. C. Le Ru *et al.* [234] for the spectral band at 500 cm^{-1} representing CN bending/in-plane ring deformation vibrations in uric acid. Raman spectrum of 65 mM uric acid solution was used in the calculation (see Fig. AIV-3 (Appendix IV)). Analytical enhancement factor shows how much more signal can be recorded by SERS as compared to the normal Raman scattering spectroscopy and was calculated as follows:

$$AEF = \frac{I_{SERS}/c_{SERS}}{I_{RS}/c_{RS}},. \quad (16)$$

here I_{SERS} and I_{RS} are integral intensities of the characteristic spectral bands in the SERS and Raman scattering spectra respectively; c_{SERS} and c_{RS} are concentration of the analyzed solutions.

No increase in the AEF values was observed on the edges of the samples. For the samples prepared by using Lee-Meisel and Leopold-Lendl colloids, the AEF varies somewhat with the measurement positions (relative standard deviation for both samples was approx. 30 %). Therefore, the whole drop area can be exploited for the measurements. The variations could be accounted for by variations in the uniformity of the NPs' film. This is expected, as there is a distribution of shapes and sizes of NPs in the colloids. Similar profiles were obtained for different samples prepared by using different batches of colloids (refer to Fig. AIV-4 – Fig. AIV-6 (Appendix IV)). For the

sample prepared using Aherne *et al*. colloid, the AEF obtain the highest values between 4th and 15th measurement points of the dried drop. This result is in contrast with the one that would be expected if the "coffee-ring" had formed. This finding could be explained by the fact that the drying pattern of the colloidal solutions depends on the shape of the NPs in it [212,223]. However, the profile of the AEF values was irreproducible for samples prepared by using this colloid (refer to Fig. AIV-6 (Appendix IV)) and, therefore, further research on the sample preparation should be carried out.

3.3.2. Detection of uric acid in aqueous solution

SERS spectra of uric acid (c=10^{-3} M) recorded on the three different colloidal substrates are presented in Figure 36. The highest enhancements were achieved in the samples prepared by using Lee-Meisel colloid as can also be seen in Figure 35 B. For these samples, average analytical enhancement

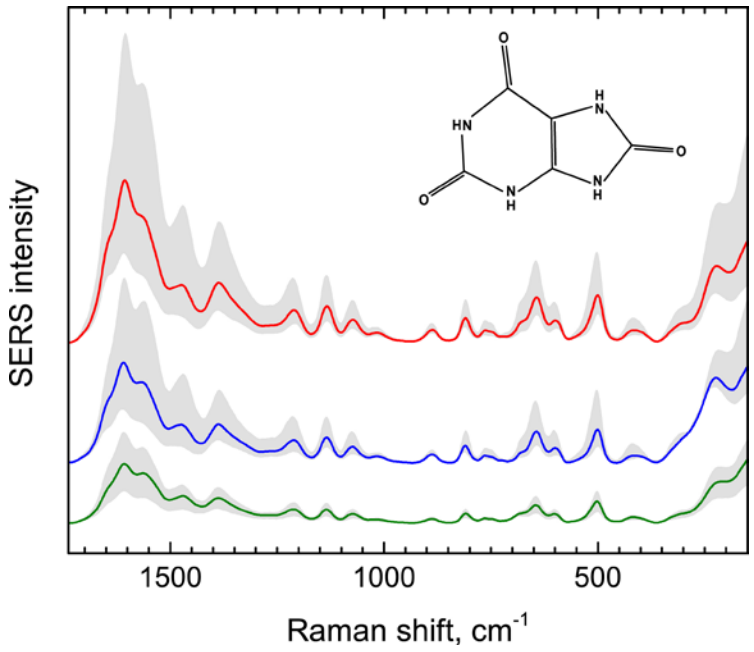

Fig. 36. SERS spectra of uric acid (c=10^{-3} M) recorded on the three different colloidal substrates: red – Lee-Meisel, green – Leopold-Lendl, blue – Aherne *et al*. colloid; the changes of the SERS intensities are observed from sample to sample.

factor (AEF) was calculated to be $2.63 \cdot 10^4$. For the samples prepared by using Leopold-Lendl and Aherne *et al*. colloids the average AEFs were $1.21 \cdot 10^4$ and $1.89 \cdot 10^4$ respectively.

Considering the reproducibility of the drop drying pattern and the enhancement obtained with each type of the colloidal substrates, we have chosen the Lee-Meisel colloid for further experiments.

SERS spectra of uric acid solutions of different concentrations are presented in Figure 37. Strong SERS signal of uric acid aqueous solution with concentrations down to 10^{-6} M (Fig. 37 C) was observed and SERS spectra could be recorded without any changes in experimental conditions (such as increasing number of scans or laser power). Medically relevant concentrations of uric acid range between 10^{-4} M and 10^{-3} M. The above results show that colloidal SERS is sensitive enough and could be used for detection of uric acid in biological fluids.

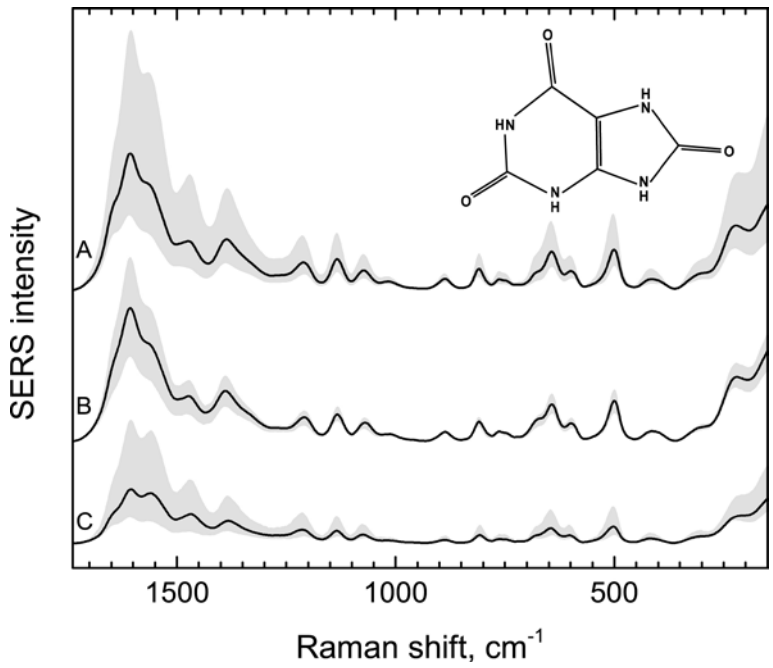

Fig. 37. SERS spectra of uric acid solutions obtained by using Lee-Meisel colloidal substrate: A – 10^{-3} M, B – 10^{-5} M, C – 10^{-6} M.

Table 3. Integral intensities of SERS spectral bands characteristic to uric acid, CN bending/in-plane ring deformation at 500 cm^{-1} and ring vibrations at 1121 cm^{-1}, at different concentration of uric acid aqueous solutions. The last column shows the ratios of the integral intensity values of the bands.

Concentration, μM	Integral intensity of spectral band at 500 cm^{-1} (δ(CN)/ring vibrations): I_{500}	Integral intensity of spectral band at 1135 cm^{-1} (ν(CN)/mixed): I_{1135}	I_{500}/I_{1135}
1	2.47	0.99	2.49
100	3.25	1.46	2.23
1000	5.86	2.78	2.11

Table 3 shows the relations between integral intensity of well separated SERS spectral bands characteristic to uric acid, CN bending/in-plane ring deformation at 500 cm^{-1} and CN stretching/mixed vibrations at 1135 cm^{-1}, and concentration of the sample solutions. The mean spectra represented as black lines in Figure 37 were used for the calculations. The integral intensity values increase linearly which suggests possibility of estimating concentration of uric acid. The ratio of the integral intensity values of the bands does not vary with concentration which suggests that the orientation of uric acid in respect to the metal nanoparticle surface does not depend on the amount of adjacent molecules. Considering the intensity variations from-sample-to-sample observed in Figure 37 (grey areas), only semi-quantitative analysis, when concentration is determined with precision within order of magnitude, is possible. This is a well-known issue and large effort is made to develop methods of sample preparation to obtain reproducible SERS enhancement [235–238]. In this work, the use of hydrophobic aluminum oxide surface as a substrate and a sealed chamber for drying of the colloidal drops allowed obtaining nearly uniform distribution of Ag NPs in the drops' area and avoid the "coffee-ring" formation. Despite the fact that high reproducibility was not yet achieved, this implies that strict control of sample preparation conditions could eventually lead to creation of reproducible self-assembled layers of NPs

which could then be used for reproducible SERS enhancement and quantitative analysis.

Another important issue in application of SERS spectroscopy for detection of uric acid in biological fluids is a fact that spectral band positions in the SERS spectrum of uric acid considerably differs from those in the conventional Raman spectra. This has been observed in this work (Fig. 38) and in some previous studies [162,239]. This makes traces of uric acid in biological fluids difficult to identify by means of SERS spectroscopy. For correct SERS signal interpretation, intricate reasons for the spectral differences should be analyzed in detail.

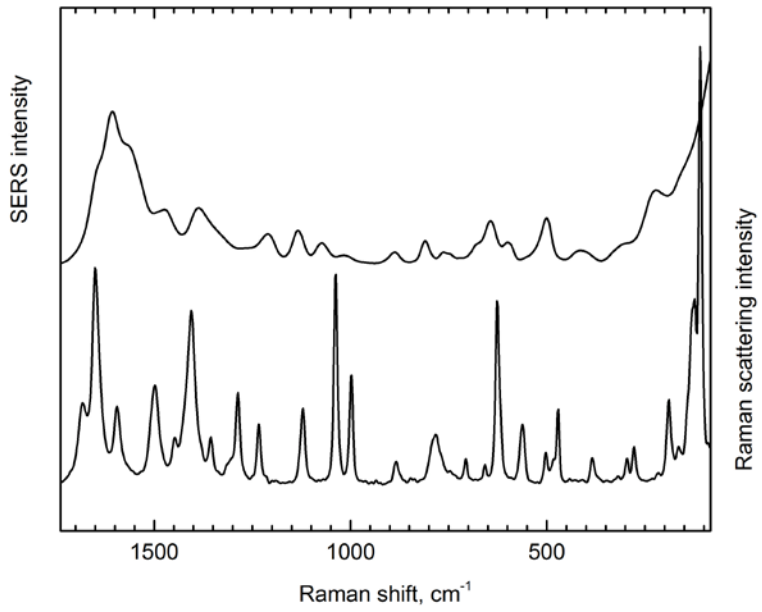

Fig. 38. Experimental Raman spectrum of uric acid powder (bottom) and SERS spectrum of 10^{-3} M uric acid solution (top).

The most significant spectral changes can be explained by tautomerization/deprotonation of uric acid molecules in aqueous solutions and while interacting with the silver surface [162]. In addition, SERS enhancement is subject to the surface selection rules and is different for each

vibrational mode [64]. We performed DFT calculations of monomeric uric acid molecule and its most stable tautomers and anions adsorbed on Ag cluster (refer to Fig. AIV-7 (Appendix IV)) in order to explain the observed spectral changes and to assign spectral bands in the SERS spectra.

The calculated structure of the most stabile uric acid tautomer - five-atom silver cluster complex in vacuum is presented in Figure 39 A. The scaled (Scaling Factor = 0.94) calculated Raman spectrum of this complex and the measured SERS spectrum in the 1740-150 cm^{-1} spectral region are depicted in Figure 39 B. The calculations where water as a solvent (uniform

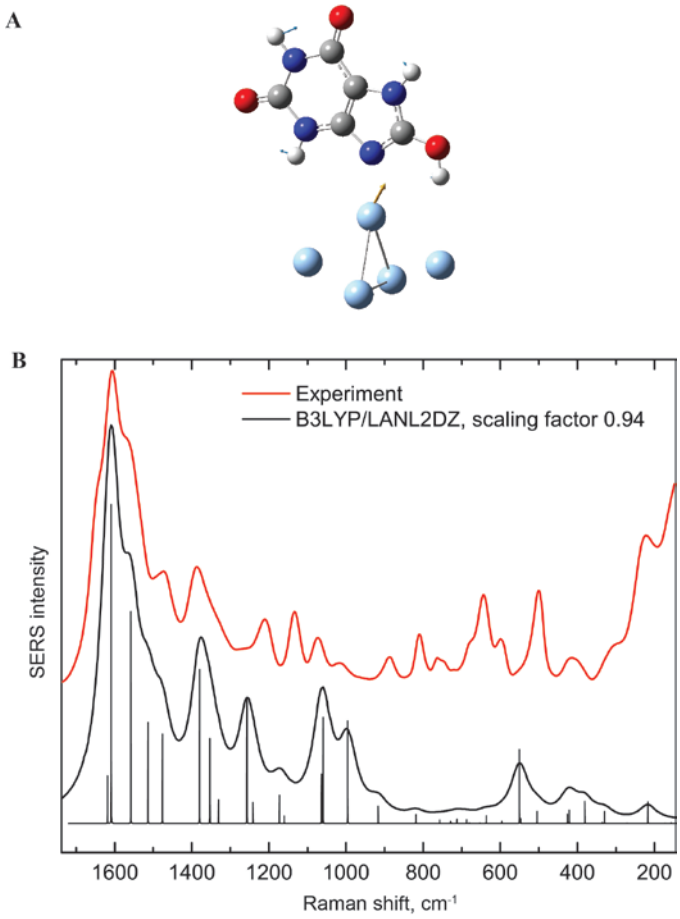

Fig. 39. (A) – The most stabile uric acid tautomer-Ag cluster complex (dark grey – carbon, dark blue – nitrogen, red – oxygen, light grey – hydrogen, light blue – silver); blue arrows depicts atoms' displacement vectors, yellow arrow – transition dipole moment vector; (B) - scaled calculated spectrum (bottom) and the measured SERS spectrum (top) in the 1740-150 cm^{-1} spectral region.

dielectric medium) was taken into account did not provide relevant changes in the structures or vibrational spectra of the complexes and will not be discussed separately.

In the 1740-900 cm^{-1} spectral region high correlation between the calculated and experimental spectrum is observed. This allows concluding that both tautomerization of the molecule and its adsorption to the metal influence the changes in the SERS spectra. The inconsistencies in the 900-300 cm^{-1} spectral region could be explained by the fact that electromagnetic enhancement effect was not included in the calculations. It can be seen in Figure 39 B that the spectral bands in the SERS spectrum can be assigned to certain modes in the calculated spectrum, but the relative intensities are in disagreement. Visualization of transition dipole moment vector (Fig. 39 A) of vibrations in this spectral region allowed predicting the role of the electromagnetic enhancement effect. The vector perpendicular to the surface of the silver cluster implies that the Raman scattering from that mode is highly enhanced and the corresponding spectral band appears much more intense in the experimental spectrum. The assignments of spectral bands are summarized in Table 4.

The obtained results on uric acid detection are important for reasoned selection of experimental conditions; also, for correct interpretation of SERS spectra and detection of uric acid in bodily fluids such as blood and urine. However, real clinical practice requires quantitative information to be feasible. In addition, biological fluids contain a wide variety of molecules that can adsorb on the metal surface and provide SERS signal. Therefore, in order to apply SERS spectroscopy as a diagnostic method in clinical practice further research on selectivity and quantification should be carried out.

Table 4. Experimental SERS (10^{-3} M uric acid solution) and calculated Raman vibrational modes and their assignment.

Experimental SERS mode (cm^{-1})	Calculated mode (cm^{-1})	Assignment
411	421	ip ring deformation *
501	550	CN bending/ip ring deformation
601	596	oop NH bending/oop ring deformation **
644	636	CO bending/skeletal ring deformation [207]
764	757	oop NH bending/ring vibration [207] **
809	821	CN bending/ip ring deformation [207]
887	916	CN stretching/NH bending [207]
1011	999	CN stretching/ring vibrations [207][1]
1074	1060	CN stretching/OH bending/mixed [207]
1135	1174	CN stretching/mixed [207]
1214	1257	ip NH bending/mixed [207] **
1386	1376	CN stretching/ip NH, OH bending ***
1502	1480	CN, CC stretching, NH, OH bending [207]
1567	1567	C=C, CN stretching, NH, OH bending
1607	1609	C=O stretching *

* strongly enhanced

** not enhanced

*** little enhanced

ip – in-plane

oop – out-of-plane

3.4. Analysis of extracellular fluid for kidney cancer diagnosis

3.4.1. Kidney cancer

Cancer (depending on its type) is one of the leading causes of morbidity and mortality worldwide. It refers to a group of diseases that can affect any part of human body and which are characterized by formation of abnormal, uncontrollably growing and proliferating tissue cells. These cells may form a mass – a tumor, disrupt tissue structure and obstruct normal body function which leads to serious ailment and/or death. They are also able to invade adjacent body parts and spread to other organs (metastasize). The number of recorded cancer cases is constantly increasing and is expected to rise up to 70 % in the next twenty years [240].

Cancer types are discriminated according to the organ the cancer starts in and the appearance of the cancer cells. It is further classified and graded according to its anatomical extent, size and abnormality of cancer cells [241]. One of the common classification systems is TNM (tumor, nodes, metastases) [242,243]. It describes whether the tumor is localized in the organ of origin (T), whether it has any involvement with lymph nodes (N) or metastases in distant organs (M). A number (1-4) next to the letter refers to the extent of the tumor: the higher the number the larger and the more spread is the cancer. Its size is further specified by letters A or B next to the number. Tumor grade is denoted by letter G and a number (1-4): the higher the number, the more abnormal are the cancer cells.

Kidneys have important functions in human body. They produce urine with which waste products are eliminated from the body. At the same time, they regulate fluid, acid-base and electrolyte balance. There are several types of kidney cancer that impair with these functions, however, renal cell carcinoma accounts for approximately 90 % of all cases [244]. According to histological examination malignant renal cell carcinoma is further divided into

five sub-types: clear cell (80 %), papillary (10%), chromophobe (5 %), collecting duct (5%) and unclassified (5 %) [244]. The earlier it is diagnosed and the more effective the treatment, the less problems it will cause. Partial, simple and radical nephrectomy (surgical kidney removal) is currently the main method for treating cancer [245]. Only partial nephrectomy (only the tumor and part of the kidney is removed) allows sparing some kidney function. On the other hand, it is extremely important that all the cancer cells are removed to prevent recurrences. Therefore, ability to determine exact borders between healthy and tumor tissues are vital. Currently, standard procedure for this purpose is histological examination of biopsied tissue [246]. Such procedure requires time for transferring the specimen to the histology lab, sample preparation (cryosectioning and staining) and examination. The waiting for the results can either prolong the surgery or require repeated surgical intervention. In addition, diagnosis made according to the histological examination is mostly based on subjective descriptors of tissue and cell structure. Therefore, there is a growing need for new intra-operative diagnostic methods which could provide reliable information about the tissue type and would allow indicating borders between healthy and cancerous tissue. Use of intrinsic biochemical cancer markers could provide information about pathological changes at their very early stage, thus making the determination of the borders more reliable.

3.4.2. Vibrational spectroscopy applications for cancer diagnostics

IR spectroscopy is a candidate method for analysis of biopsied tissue samples. IR absorption spectra can be recorded in fraction of a minute. Their analysis allows obtaining biochemical information about the sample, which could be further used to discriminate between healthy and cancerous tissues. In addition, compact modern FTIR spectrometers can be used directly in the operating room (OR) for *in situ* analysis. Such approach has been

already successfully implemented in brain surgery [247]. There is also a multitude of laboratory research carried out in this field and on various other tissue types [18,248–251]. Wider implementation of the method in clinical practice is limited by problematic sample preparation and complex data analysis. Since tissue contains water, which has strong absorbance in the IR spectral region (namely at 1400-1800 cm^{-1} and 2600-3800 cm^{-1}), it needs to be dried. Thin (10-50 μm) dried cryosections of tissues are usually used in IR spectroscopy [23]. Such sample preparation takes time and affects tissue structure (the cells are possibly damaged when the tissue is frozen, sectioned and thawed) [252]. In addition, tissue is built from large polyatomic molecules (proteins, lipids, carbohydrates, fatty acids, etc.) which all contribute to the IR absorption spectra. Thus, small differences in the chemistry of healthy and cancerous tissues may remain obscured or complex statistical analysis is needed to analyze the spectra.

The minor changes in biochemistry of cancer cells as compared with the healthy ones are difficult to detect by IR spectroscopy. However, the consequence of these changes – significantly increased metabolism [253] – could be easier to spot. Cancerous cells need more nutrition to sustain their fast growth and proliferation. The nutrients reach the cells from blood through extracellular fluid (ECF) [254]. Thus, it is expected that the chemical composition of the ECF around the cancerous cells is altered considerably with increased concentrations of glucose and lipids [255,256]. As the tumor grows, part of its cells appears far away from the blood vessels providing the nutrients and oxygen. For this reason, some types of cancer (kidney, uterus, bladder, ovary, skin and brain) accumulate glycogen – polysaccharide of glucose – to a great extent in order to survive under hypoxic conditions and in environment poor in nutrients [257]. The rapid metabolism also provides increased amounts of waste products (such as lactic acid) in the ECF. The first attempt to obtain infrared spectra of ECF surrounding healthy and cancerous

tissue cells was made by our group [258]. It was shown that the spectra of ECF differ, but no statistics was performed due to insufficient number of samples.

3.5. IR spectroscopic analysis of ECF: experimental details

3.5.1. ECF sample preparation

Tissue samples were obtained from Vilnius University hospital Santariskiu Klinikos during partial, simple or radical nephrectomy. The protocol of this study was approved by Vilnius regional bioethics committee (approval No. 158200-15-803-312). Thin films of ECF were prepared by pressing small piece of the freshly resected human kidney tissue against diamond ATR element of FTIR spectrometer Alpha (Bruker Optik GmbH, Ettlingen, Germany). The tissue was removed from the element after a few seconds and the remaining ECF was left to dry at room temperature.

3.5.2. FTIR spectroscopy measurements of ECF films

IR absorption spectra of the ECF samples were collected in ATR mode of FTIR spectrometer Alpha (Bruker Optik GmbH, Ettlingen, Germany) equipped with single reflection diamond ATR crystal and DTGS detector. From the moment the sample was placed on the ATR element, repeated measurements were performed collecting 4 scans for each spectrum until the ECF dried. The spectra were recorded in 4000-800 cm^{-1} spectral range with spectral resolution of 4 cm^{-1}. Interferograms were Fourier transformed into spectra applying Blackmann-Harris 3 apodization function and zero filling factor 2.

3.5.3. Spectral analysis of ECF films

Ten IR spectra of each of the dried ECF samples were averaged into one resultant spectrum. Baseline correction was applied to the spectra before qualitative spectral analysis. In order to evaluate whether spectral differences between spectra of healthy and cancerous tissue correspond to the tissue

type, multivariate analysis was used. Vector normalized, first derivative spectra were used in the HCA and PCA. MATLAB package (Version 7.14, The MathWorks, Inc., USA) was used for the analysis. For the HCA, Ward's algorithm was used to group the data according to Euclidean distances between the spectra in the 1200-890 cm^{-1} spectral region where lies the most significant differences between the samples obtained from healthy and cancerous tissue. Tree diagrams, or dendrograms, were constructed to represent the results of the clustering. An algorithm of optimal leaf ordering was applied for the adjacent clusters to have the highest similarity [259].

PCA was performed using MATLAB function *princomp*. PC score plots were constructed from the first two principal components (representing approx. 85 % of variance) in order to observe relationship between the data.

3.6. IR spectroscopic analysis of ECF: results and discussion

There is a growing need for new intra-operative diagnostic methods which could provide reliable information about the tissue type and would allow indicating borders between healthy and cancerous tissue. Here, ECF samples taken from healthy and cancerous tissue were analyzed by means of ATR FT-IR spectroscopy. HCA and PCA were applied to examine the spectral differences between normal tissue and various tumors and determine whether the method could be suitable for clinical practice.

Table 5. Grouping of tissue samples obtained after partial, simple or radical nephrectomy from patients with kidney tumors; this grouping is according to the tissue type and tumor grade as determined by histopathology.

Tissue type	Number of patients	Remarks
Normal tissue	84	
G1*	11	1 sample – chromophobe renal cell carcinoma
G2*	44	2 samples – papillary, 2 samples – multilocular cystic, 1 sample - chromophobe renal cell carcinoma
G3*	23	1 sample - mixed epithelial and stromal tumor, 1 sample – papillary renal cell carcinoma
Kidney angiomyolipoma	1	
Kidney oncocytoma	4	
Pyelonephritis	1	

*Unless stated otherwise under Remarks, all the tumors were diagnosed as clear cell renal cell carcinoma

The spectral measurements were performed directly in the OR during surgery of 84 patients. For each patient two tissue samples – normal and tumor were taken and used for preparation of thin ECF film on the diamond ATR crystal. Information from histopathological examination was later obtained and used to group the samples according to tumor type and grade (Table 5).

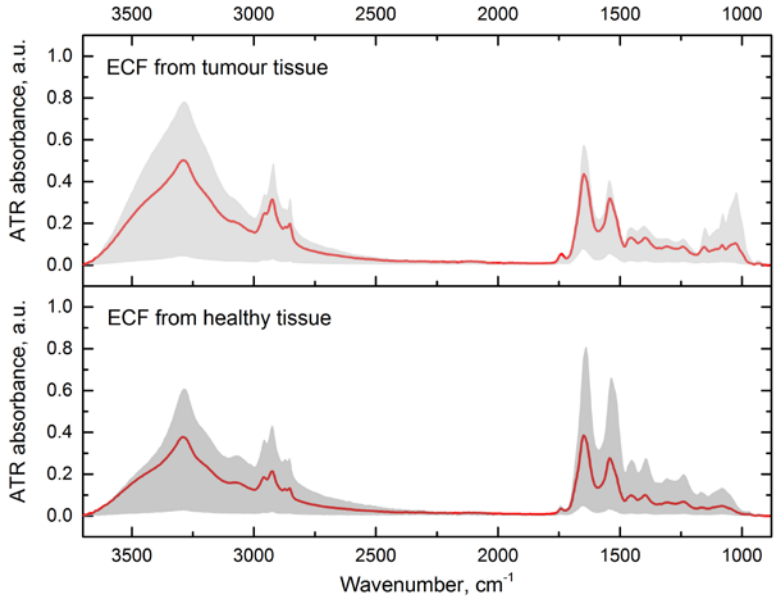

Fig. 40. Baseline corrected IR absorption spectra of the ECF films of healthy (top) and tumor (bottom) tissue. The gray areas represent variations of spectral intensity between different samples.

Baseline corrected IR absorption spectra of the ECF films of normal (healthy) and tumor tissue are presented in Figure 40. The red curves represent averages of the spectra while the grey areas show variations between the spectra in each group. In the 1700 – 1500 cm^{-1} spectral region the Amide I and Amide II protein bands are located. It has been shown that the structure of these bands is highly sensititve to protein structures [260]. However, it can be seen that the main spectral differences between the

normal and tumour ECFs are in the 1200 – 890 cm^{-1} spectral region. Carbohydrates and phospholipids give rise to the spectral bands in this region.

Three strong bands at 1152, 1080 and 1022 cm^{-1} in the spectra of ECF taken from cancerous tissue are assigned to δ(CHO) and υ(C-O) vibrations in glycogen and glucose [261]. Reference spectra of synthetic glucose, glycogen and lactic acid were recorded in order to clarify the assignment (Fig. 41). It can be seen that spectral bands of glucose and, in particular, glycogen correspond to the bands observed in the spectra of the ECF. According to Warburg effect, cancer cells predominantly produce energy by fast-rate glycolysis which allows them proliferating faster and adapting to anaerobic conditions when the tumor cells grow far away from blood vessels

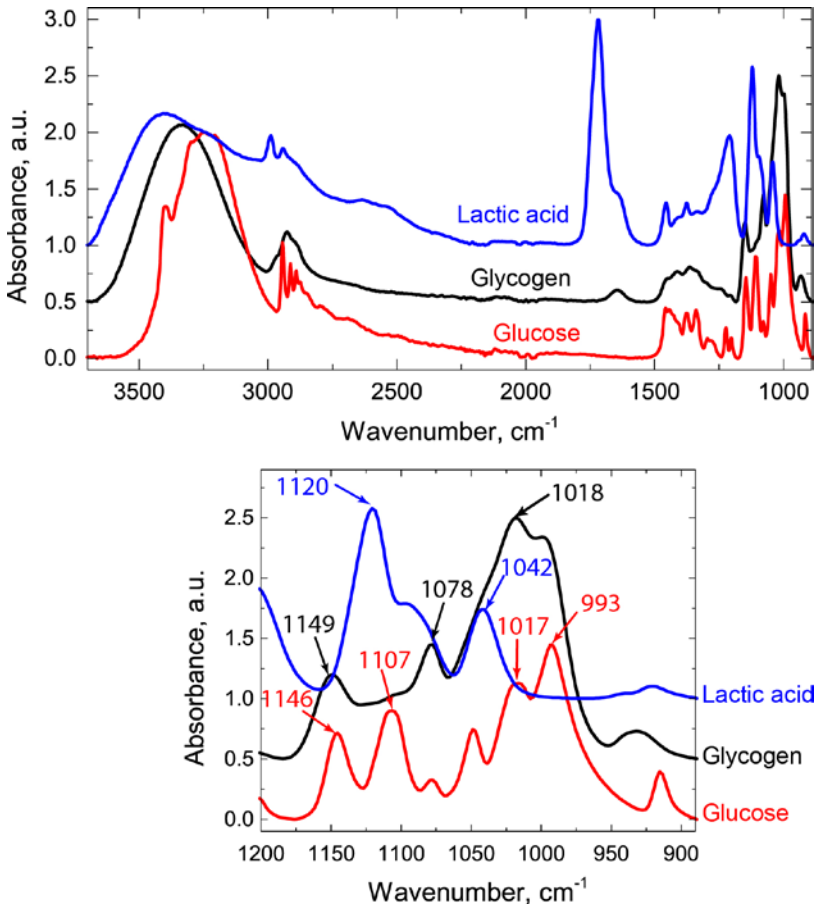

Fig. 41. IR absorption spectra of synthetic glucose, glycogen and lactic acid. The enlarged spectral region at 1200-890 cm^{-1} contains spectral bands assigned to δ(CHO) and υ(C-O) vibrations.

[262]. Additionally, it has been shown that glucose in kidney cancer cells (and the most frequent clear cell renal cell carcinoma in particular) is stored in cytosol in form of glycogen [257]. The fact that both glycogen and glucose spectral bands can be observed in the spectra suggests that the sample film contains not only the ECF but also detached cells and intracellular fluid from damaged cells in the tissue. Situation is different for normal cells. Low-rate glycolysis in normal cells serves as an efficient energy source and less glucose has to be supplied by ECF. Some glucose in such cells are converted to glycogen and stored in cytosol as fast energy source in case of urgent demand of energy. Low concentrations of glucose and glycogen in the fluid samples of normal tissue cause the absence of their characteristic infrared spectral bands.

We have also measured IR absorption spectra of dried tissue samples by means of ATR FTIR spectroscopy. The small tissue sections used to obtain ECF films were dried in vacuum and then pressed to the ATR crystal to record the spectra. Although not shown here, the spectral results are similar to those obtained for the ECF films – spectra of cancerous tissue contains glycogen/glucose spectral bands in the 1200 – 880 cm^{-1} spectral region whereas spectra of normal tissue – do not. This is in contrast to the results obtained from the spectra of cryosectioned tissue samples where the spectral differences are hardly visible and statistical analysis is required to differentiate the tissue type [51]. Possibly, in case of cryosectioned tissue sample preparation (snap-freezing, sectioning, thawing and drying) causes changes in the carbohydrate content of the sample [252].

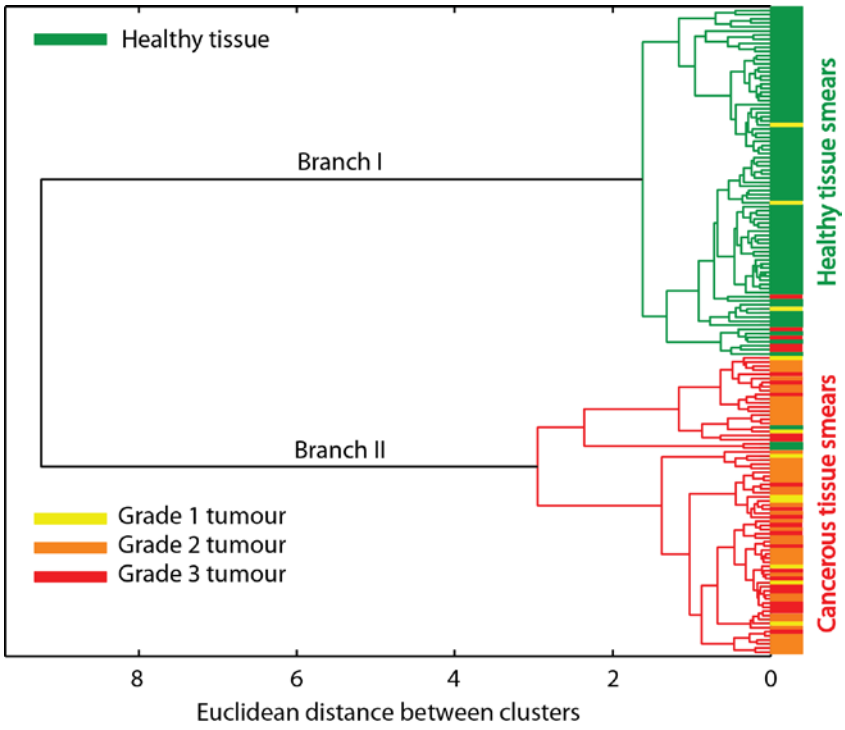

Fig. 42. Dendrogram representing results of HCA of IR spectra of ECF taken from healthy kidney tissue and cancerous kidney tissue of various tumor grades.

Multivariate data analysis allows better evaluation of relationship between samples. HCA was applied to the spectra of ECF films of healthy and grade G1 - G3 tumour tissue. Two main well separated clusters can be observed in the dendrogram in Figure 42. The first cluster – coloured in green (Branch I) – is mainly constituted from the spectra of healthy tissue films. The three spectra of cancerous tissue films (red and orange) infiltrated in this group under closer inspection were revieled to contain major lipid bands. This could be the reason for their clustering in the group of healthy tissue films. It can also be observed that there are several sub-clusters in this group. This shows that the spectra of healthy tissue films taken from different patients are not identical. The second major group – coloured in yellow, orange and red according to the tumour grade (Branch II) – is mainly consituted from the spectra of cancerous tissue films. Due to high variations between the spectra and the relative intensity of the glycogen/glucose bands as seen in Figure 40,

no significant grouping according to the tumour grade can be observed in this group. Similarily as in the group of healthy tissue films, the observed sub-clusters mainly represent differences between spectra recorded in the samples from different patients. They can be explained by several reasons. Firstly, when stamping the tissue to obtain films, only particular small area of the tumour or healthy tissue is sampled. Naturally, there might be variations in chemistry between different areas in the tissue which subsequently cause variations in the spectra. On the other hand, a concept of personalized medicine reasons that molecular content is changing from patient to patient. Subsequently, the variations in the spectra of tissue films taken from different patients are observed. However, the obvious clustering of spectra of healthy and tumour tissue films imply that they can be used to differentiate between the tissue types. Of note is that including the spectra of benign tumours into the analysis resulted them being clustered in the group of healthy tissue films.

According to the HCA results presented in Figure 42, sensitivity and specificity values were calculated. Sensitivity shows the ability of a method to correctly identify cancer and is calculated as follows [263]:

$$\text{Sensitivity} = \frac{\text{True positives}}{\text{True positives} + \text{False negatives}}, \quad (17)$$

here True positive is the number of cases when the result of analysis predicts cancer and the patient has the disease; False negative is the number of cases when the result of analysis does not predict cancer, but the patient has the disease. Similarly, specificity shows the ability of a method to corectly identify healthy tissue and is calculated as follows [263]:

$$\text{Specificity} = \frac{\text{True negatives}}{\text{True negatives} + \text{False positives}}, \quad (18)$$

here True negatives is a number of cases when the result of analysis correctly identifies healthy tissue; False positives is a number of cases when the result of analysis predict cancer, but the patient does not have the disease. The sensitivity and specificity values obtained for the HCA analysis of the IR

absorption spectra of the ECF samples were 91 % and 96 % respectively. This result means that spectra of ECF taken from healthy tissue can be better identified than spectra of ECF taken from cancerous tissue. This is reasoned by the fact that in the latter spectral variations from sample to sample and due to different tumour grades are larger. The relatively low sensitivity value shows that more samples have to be investigated and the spectral analysis

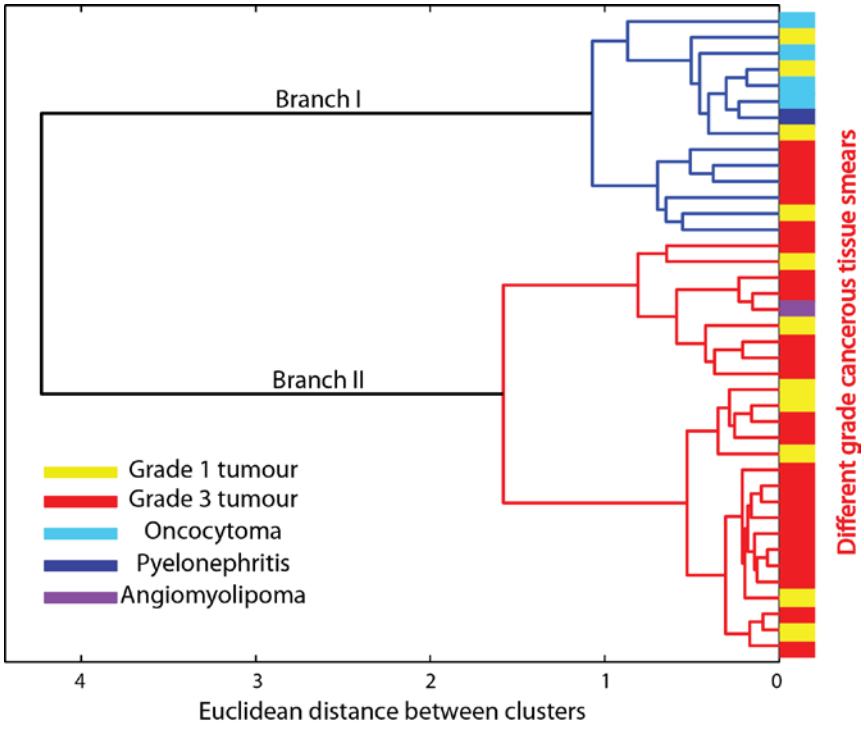

Fig. 43. Dendrogram representing results of HCA of IR spectra of ECF taken from benign kidney tumors (oncocytomas and angiomyolipoma), kidney tissue inflamation (pyelonephritis) and kidney tumors of grades G1 and G3.

methods improved before IR spectroscopy can be applied in clinical practice.

In order to test whether IR absorption spectra of tissue films from tumours of different malignancies could be differentiated, HCA was performed on the spectra of benign tumours and tumours of grades G1 and G3. The corresponding dendrogram is presented in Figure 43. Similarily as in the dendrogram in Figure 42, two major clusters (coloured in blue (Branch I) and red (Branch II)) can be observed. However, the grouping of the spectra is

not so distinct as in the case of healthy and tumour tissues. The first (I) cluster contains two sub-clusters one of which mainly contains spectra of begnin tumours. However, the second sub-cluster as well as the second cluster (II) contains spectra of G1 and G3 graded tumour films intermixed between themselves. Again, this can be reasoned by variations in chemistry between different areas in the tissue or variations in the spectra of tissue films taken from different patients. In addition, limited amount of samples could cause

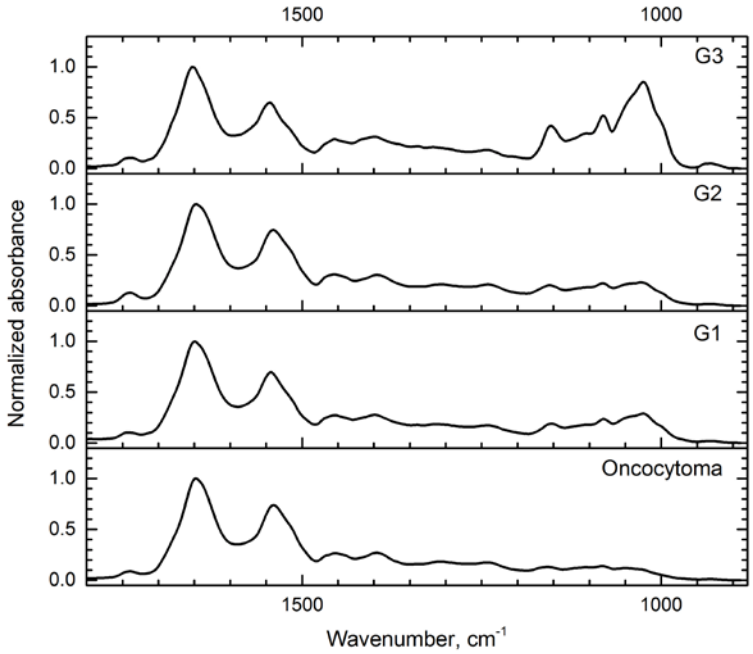

Fig. 44. Normalized (according to the Amide I band) averages of IR absorption spectra of ECF taken from cancerous kidney tissue of various grades and a benign tumor – oncocytoma.

the inconclusive results of the HCA.

Averaged IR absorption spectra of ECF taken from cancerous kidney tissue of various grades and a benign tumor – oncocytoma are presented in Figure 44. The spectra are normalized according to the Amide I spectral band at 1650 cm^{-1}. Differences in relative intensity of glycogen/glucose spectral bands for each type of tissue can be observed. The more malignant the tumour, the more pronounced the glycogen/glucose

bands are. On the other hand, due to the variations between the spectra (Fig. 40), the averaged spectra of G1 and G2 tumours are highly similar. The averaged spectrum of oncocytomas (Fig. 44) resemble spectra of healthy tissue ECF films (Fig. 40). This explains their clustering in the group of healthy tissue ECF films as mentioned above.

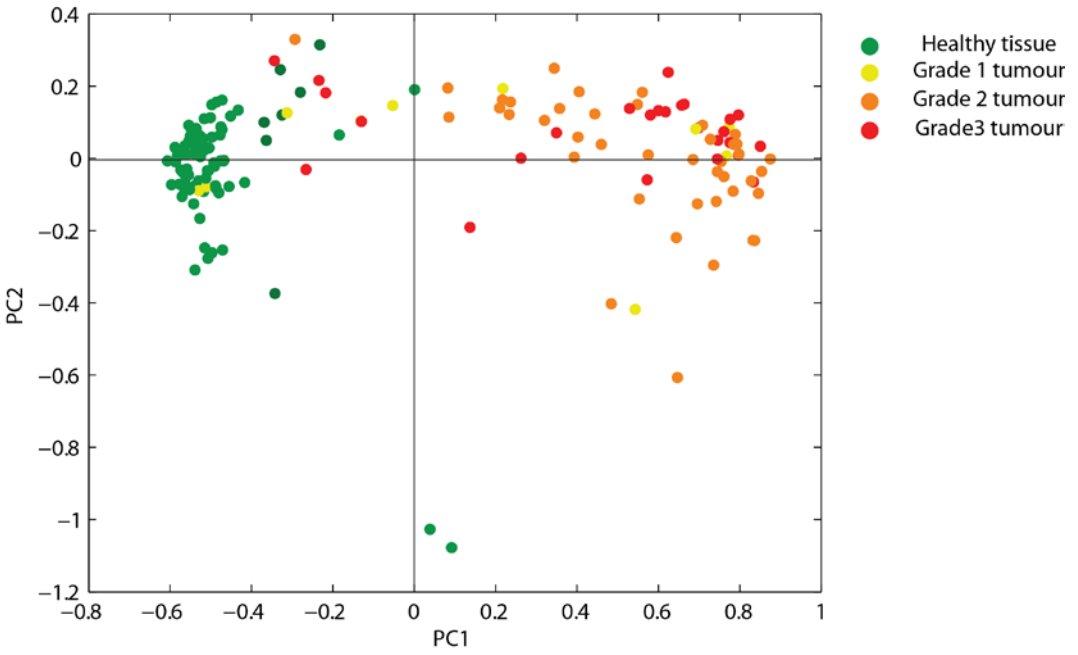

Fig. 45. Principal component score plot representing results of PCA of IR spectra of ECF taken from healthy kidney tissue and cancerous kidney tissue of various tumor grades.

PCA was performed as a complementary data analysis technique to show the relationship between the IR absorption spectra of healthy and tumor tissue films and the spectra of benign tumors and tumors of grade G1 and G3. The corresponding PC score plots of the first two principal components are presented in Figure 45 and Figure 46. The results of the PCA can be interpreted in a similar way as the results of the HCA. In Figure 45, the clusters of healthy and tumor tissues are well separated. It can be observed that while the data points in the group of the healthy tissue (green) are localized and relatively close to each other, the data points in the group of the

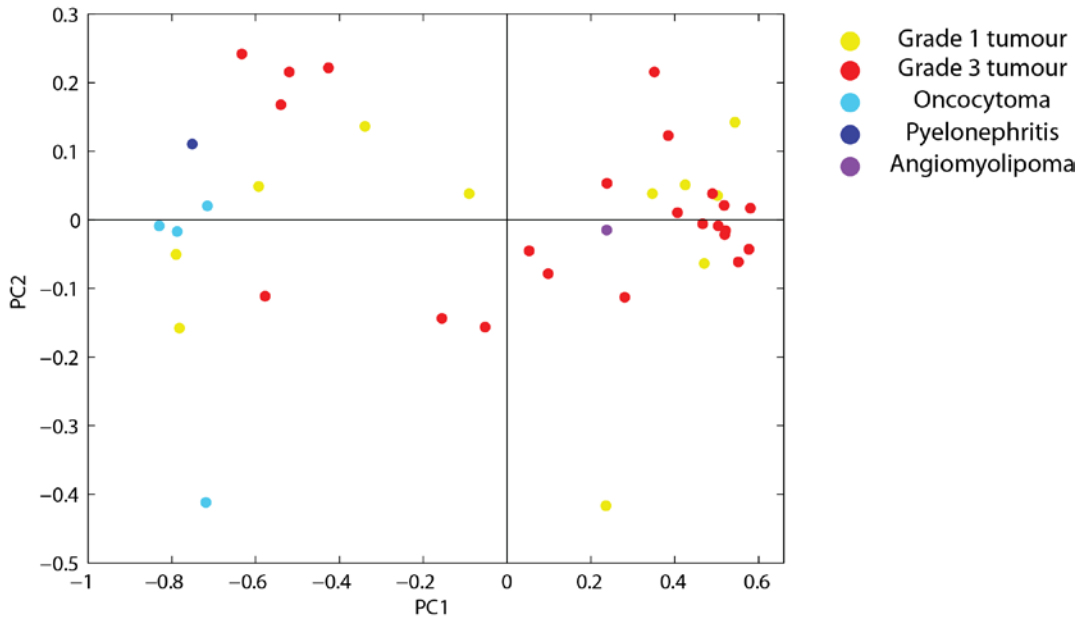

Fig. 46. Principal component score plot representing results of PCA of IR spectra of ECF taken from benign kidney tumours (oncocytomas and angiomyolipoma), kidney tissue inflamation (pyelonephritis) and kidney tumours of grades G1 and G3.

tumor tissue (red) are more spread out which means that the spectral differences are larger in this group.

In Figure 46 the clusters of benign tumors and tumors of grade G1 and G3 are mostly separated as well. This plot supplements the results presented in Figure 43, as it can be observed that the data points in the group of G3 tumors (red) are less spread than others. This shows that the spectral differences vary less between spectra of this group; thus, it can be well separated from the group of G1 and benign tumors (light blue).

3.7. Vibrational spectroscopy analysis of biological fluids: conclusions

1. For detection of metabolites in biological fluids, drop-dried colloidal substrates using Lee-Meisel, Leopold-Lendl and Aherne et al. colloids containing nanoparticles of different shapes were produced. Nearly uniform spread of the nanoparticles across the area of the drop was achieved which, in turn, led to relatively small variance (approx. 30 %) in analytical enhancement factor across the drops' diameter.

2. The SERS substrates produced by using the Lee-Meisel colloid allowed detecting uric acid in aqueous solutions of concentrations down to 10^{-6} M. DFT calculations of uric acid tautomer – five-atom silver cluster complexes allowed correct assignment uric acid spectral bands in SERS spectra. Differences between Raman and SERS spectra of uric acid can be mainly explained by tautomerization of the molecule and its bonding to the silver surface.

3. IR absorption spectra of dried ECF taken from kidney tissue contain reliable spectral markers, mainly assigned to glycogen, capable of differentiating between healthy and tumor tissue. Results of the HCA of the spectra show that the spectra of healthy and tumor tissue films can be reliably separated into two groups. Sensitivity and specificity values of the method are 91 % and 96 % respectively.

Bibliography

[1] F. Siebert and P. Hildebrandt, *Vibrational spectroscopy in life science* (Wiley-VCH, Weinheim, 2008).

[2] P. Lasch and J. Kneipp, Eds., *Biomedical vibrational spectroscopy* (Wiley-Interscience, Hoboken, N.J, 2008).

[3] C. Krafft and J. Popp, The many facets of Raman spectroscopy for biomedical analysis, Anal. Bioanal. Chem. **407**, 699–717 (2014).

[4] C. Krafft, I. W. Schie, T. Meyer, M. Schmitt, and J. Popp, Developments in spontaneous and coherent Raman scattering microscopic imaging for biomedical applications, Chem. Soc. Rev. **45**, 1819–1849 (2016).

[5] C. Hughes and M. J. Baker, Can mid-infrared biomedical spectroscopy of cells, fluids and tissue aid improvements in cancer survival? A patient paradigm, Analyst **141**, 467–475 (2016).

[6] L. Opilik, T. Schmid, and R. Zenobi, Modern Raman Imaging: Vibrational Spectroscopy on the Micrometer and Nanometer Scales, Annu. Rev. Annal. Chem. **6,** 379-398 (2013).

[7] A. A. Bunaciu, S. Fleschin, and H. Y. Aboul-Enein, Biomedical Investigations Using Fourier Transform-Infrared Microspectroscopy, Crit. Rev. Anal. Chem. **44**, 270–276 (2014).

[8] H. Kim and M. Cho, Infrared Probes for Studying the Structure and Dynamics of Biomolecules, Chem. Rev. **113**, 5817–5847 (2013).

[9] R. Adato and H. Altug, In-situ ultra-sensitive infrared absorption spectroscopy of biomolecule interactions in real time with plasmonic nanoantennas, Nat. Commun. **4**, 2154 (2013).

[10] A. Rygula, K. Majzner, K. M. Marzec, A. Kaczor, M. Pilarczyk, and M. Baranska, Raman spectroscopy of proteins: a review, J. Raman Spectrosc. **44**, 1061–1076 (2013).

[11] M. J. Baker, S. R. Hussain, L. Lovergne, V. Untereiner, C. Hughes, R. A. Lukaszewski, G. Thiéfin, and G. D. Sockalingum, Developing and understanding biofluid vibrational spectroscopy: a critical review, Chem. Soc. Rev. **45**, 1803–1818 (2016).

[12] J.-X. Cheng and X. S. Xie, Vibrational spectroscopic imaging of living systems: An emerging platform for biology and medicine, Science **350**, aaa8870 (2015).

[13] M. Diem, A. Ergin, S. Remiszewski, X. Mu, A. Akalin, and D. Raz, Infrared micro-spectroscopy of human tissue: principles and future promises, Faraday Discuss. (2016).

[14] D. I. Ellis, D. P. Cowcher, L. Ashton, S. O'Hagan, and R. Goodacre, Illuminating disease and enlightening biomedicine: Raman spectroscopy as a diagnostic tool, Analyst **138**, 3871–3884 (2013).

[15] A. L. Mitchell, K. B. Gajjar, G. Theophilou, F. L. Martin, and P. L. Martin-Hirsch, Vibrational spectroscopy of biofluids for disease screening or diagnosis: translation from the laboratory to a clinical setting, J. Biophotonics **7**, 153–165 (2014).

[16] M. J. Baker and K. Faulds, Fundamental developments in clinical infrared and Raman spectroscopy, Chem. Soc. Rev. **45**, 1792–1793 (2016).

[17] C. Petibois and B. Desbat, Clinical application of FTIR imaging: new reasons for hope, Trends Biotechnol. **28**, 495–500 (2010).

[18] A. B. Seddon, Mid-infrared (IR) – A hot topic: The potential for using mid-IR light for non-invasive early detection of skin cancer in vivo, Phys. Status Solidi B **250**, 1020–1027 (2013).

[19] K. Kong, C. Kendall, N. Stone, and I. Notingher, Raman spectroscopy for medical diagnostics — From in-vitro biofluid assays to in-vivo cancer detection, Adv. Drug Deliv. Rev. **89**, 121–134 (2015).

[20] Z. Wang, Y. Liu, L. Gao, Y. Chen, P. Luo, K. K. Wong, and S. T. Wong, Use of multimode optical fibers for fiber-based coherent anti-Stokes Raman scattering microendoscopy imaging, Opt. Lett. **36**, 2967–2969 (2011).

[21] S. Kumar, T. Verma, R. Mukherjee, F. Ariese, K. Somasundaram, and S. Umapathy, Raman and infra-red microspectroscopy: towards quantitative evaluation for clinical research by ratiometric analysis, Chem. Soc. Rev. **45**, 1879–1900 (2016).

[22] N. C. Purandare, J. Trevisan, I. I. Patel, K. Gajjar, A. L. Mitchell, G. Theophilou, G. Valasoulis, M. Martin, G. von Bünau, et al., Exploiting biospectroscopy as a novel screening tool for cervical cancer: towards a framework to validate its accuracy in a routine clinical setting, Bioanalysis **5**, 2697–2711 (2013).

[23] M. J. Baker, J. Trevisan, P. Bassan, R. Bhargava, H. J. Butler, K. M. Dorling, P. R. Fielden, S. W. Fogarty, N. J. Fullwood, et al., Using Fourier transform IR spectroscopy to analyze biological materials, Nat. Protoc. **9**, 1771–1791 (2014).

[24] H. J. Butler, L. Ashton, B. Bird, G. Cinque, K. Curtis, J. Dorney, K. Esmonde-White, N. J. Fullwood, B. Gardner, et al., Using Raman spectroscopy to characterize biological materials, Nat. Protoc. **11**, 664–687 (2016).

[25] J. Trevisan, P. P. Angelov, A. D. Scott, P. L. Carmichael, and F. L. Martin, IRootLab: a free and open-source MATLAB toolbox for vibrational biospectroscopy data analysis, Bioinformatics, btt084 (2013).

[26] J. C. Anderson, J. C. Williams, A. P. Evan, K. W. Condon, and A. J. Sommer, Analysis of urinary calculi using an infrared microspectroscopic surface reflectance imaging technique, Urol. Res. **35**, 41–48 (2007).

[27] M. Claybourn, External Reflection Spectroscopy, in Handb. Vib. Spectrosc. (John Wiley & Sons, Ltd, 2006).

[28] C. Haisch, Raman-based microarray readout: a review, Anal. Bioanal. Chem., 1–11 (2016).

[29] D.-W. Li, W.-L. Zhai, Y.-T. Li, and Y.-T. Long, Recent progress in surface enhanced Raman spectroscopy for the detection of environmental pollutants, Microchim. Acta **181**, 23–43 (2013).

[30] Valdas Sablinskas, Justinas Ceponkus, *Modernioji molekulių virpesinė spektrometrija* (*www.bfsk.ff.vu.lt/Modernioji_molekuliu_virpesine_spektrometrija.pdf).*

[31] Peter R. Griffiths, James A. De Haseth, *Fourier Transform Infrared Spectrometry, 2nd Edition* (John Wiley & Sons, Inc., Hoboken, New Jersey, 2007).

[32] Laurence A. Nafie, Theory of Raman Scattering in Handbook of Raman Spectroscopy, Ian R. Lewis, Howell G. M. Edwards, Eds. (Marcel Dekker AG, Basel 2001).

[33] http://refractiveindex.info/ (30 June 2016).

[34] K. V. Oliver, F. Matjiu, C. Davey, S. Moochhala, R. J. Unwin, and P. R. Rich, Attenuated total reflection Fourier transform infrared (ATR-FTIR) spectroscopy as a bedside diagnostic tool for detecting renal disease biomarkers in fresh urine samples, SPIE Proc. **9332**, 933202 (2015).

[35] J. R. Hands, K. M. Dorling, P. Abel, K. M. Ashton, A. Brodbelt, C. Davis, T. Dawson, M. D. Jenkinson, R. W. Lea, et al., Attenuated total reflection fourier transform infrared (ATR-FTIR) spectral discrimination of brain tumour severity from serum samples, J. Biophotonics **7**, 189–199 (2014).

[36] J. R. Hands, G. Clemens, R. Stables, K. Ashton, A. Brodbelt, C. Davis, T. P. Dawson, M. D. Jenkinson, R. W. Lea, et al., Brain tumour differentiation: rapid stratified serum diagnostics via attenuated total reflection Fourier-transform infrared spectroscopy, J. Neurooncol. **127**, 463–472 (2016).

[37] M. Zhao, G. Downey, and C. P. O'Donnell, Detection of adulteration in fresh and frozen beefburger products by beef offal using mid-infrared ATR spectroscopy and multivariate data analysis, Meat Sci. **96**, 1003–1011 (2014).

[38] S. Jawaid, F. N. Talpur, S. T. H. Sherazi, S. M. Nizamani, and A. A. Khaskheli, Rapid detection of melamine adulteration in dairy milk by SB-ATR–Fourier transform infrared spectroscopy, Food Chem. **141**, 3066–3071 (2013).

[39] J. y. Shim, I. k. Cho, H. k. Khurana, Q. x. Li, and S. Jun, Attenuated Total Reflectance–Fourier Transform Infrared Spectroscopy Coupled with Multivariate Analysis for Measurement of Acesulfame-K in Diet Foods, J. Food Sci. **73**, C426–C431 (2008).

[40] A. C. Galvis-Sánchez, A. Barros, and I. Delgadillo, FTIR-ATR infrared spectroscopy for the detection of ochratoxin A in dried vine fruit, Food Addit. Contam. **24**, 1299–1305 (2007).

[41] K. L. Andrew Chan and S. G. Kazarian, Attenuated total reflection Fourier-transform infrared (ATR-FTIR) imaging of tissues and live cells, Chem Soc Rev **45**, 1850–1864 (2016).

[42] M. K. Kuimova, K. L. A. Chan, and S. G. Kazarian, Chemical Imaging of Live Cancer Cells in the Natural Aqueous Environment, Appl. Spectrosc. **63**, 164–171 (2009).

[43] T. P. Wrobel, K. M. Marzec, K. Majzner, K. Kochan, M. Bartus, S. Chlopicki, and M. Baranska, Attenuated total reflection Fourier transform infrared (ATR-FTIR) spectroscopy of a single endothelial cell, Analyst **137**, 4135–4139 (2012).

[44] S. G. Kazarian and K. L. A. Chan, Micro- and Macro-Attenuated Total Reflection Fourier Transform Infrared Spectroscopic Imaging, Appl. Spectrosc. **64**, 135A–152A (2010).

[45] K. L. A. Chan, X. Niu, A. J. de Mello, and S. G. Kazarian, Rapid prototyping of microfluidic devices for integrating with FT-IR spectroscopic imaging, Lab. Chip **10**, 2170–2174 (2010).

[46] L. P. Choo, D. L. Wetzel, W. C. Halliday, M. Jackson, S. M. LeVine, and H. H. Mantsch, In situ characterization of beta-amyloid in Alzheimer's diseased tissue by synchrotron Fourier transform infrared microspectroscopy, Biophys. J. **71**, 1672–1679 (1996).

[47] M. Szczerbowska-Boruchowska, P. Dumas, M. Z. Kastyak, J. Chwiej, M. Lankosz, D. Adamek, and A. Krygowska-Wajs, Biomolecular investigation of human substantia nigra in Parkinson's disease by synchrotron radiation Fourier transform infrared microspectroscopy, Arch. Biochem. Biophys. **459**, 241–248 (2007).

[48] W. André, C. Sandt, P. Dumas, P. Djian, and G. Hoffner, Structure of Inclusions of Huntington's Disease Brain Revealed by Synchrotron Infrared Microspectroscopy: Polymorphism and Relevance to Cytotoxicity, Anal. Chem. **85**, 3765–3773 (2013).

[49] M. Bonda, V. Perrin, B. Vileno, H. Runne, A. Kretlow, L. Forró, R. Luthi-Carter, L. M. Miller, and S. Jeney, Synchrotron Infrared Microspectroscopy Detecting the Evolution of Huntington's Disease Neuropathology and Suggesting Unique Correlates of Dysfunction in White versus Gray Brain Matter, Anal. Chem. **83**, 7712–7720 (2011).

[50] M. J. Baker, E. Gazi, M. D. Brown, J. H. Shanks, P. Gardner, and N. W. Clarke, FTIR-based spectroscopic analysis in the identification of clinically aggressive prostate cancer, Br. J. Cancer **99**, 1859–1866 (2008).

[51] V. Sablinskas, V. Urboniene, J. Ceponkus, A. Laurinavicius, D. Dasevicius, F. Jankevicius, V. Hendrixson, E. Koch, and G. Steiner, Infrared spectroscopic imaging of renal tumor tissue, J. Biomed. Opt. **16**, 96006 (2011).

[52] H. Fabian, N. A. N. Thi, M. Eiden, P. Lasch, J. Schmitt, and D. Naumann, Diagnosing benign and malignant lesions in breast tissue sections by using IR-microspectroscopy, Biochim. Biophys. Acta BBA - Biomembr. **1758**, 874–882 (2006).

[53] M. Verdonck, A. Denayer, B. Delvaux, S. Garaud, R. D. Wind, C. Desmedt, C. Sotiriou, K. Willard-Gallo, and E. Goormaghtigh, Characterization of human breast cancer tissues by infrared imaging, Analyst **141**, 606–619 (2016).

[54] J. Nallala, O. Piot, M.-D. Diebold, C. Gobinet, O. Bouché, M. Manfait, and G. D. Sockalingum, Infrared imaging as a cancer diagnostic tool: Introducing a new concept of spectral barcodes for identifying molecular changes in colon tumors, Cytometry A **83A**, 294–300 (2013).

[55] L. C. Prinsloo, L. Wadley, and M. Lombard, Infrared reflectance spectroscopy as an analytical technique for the study of residues on stone tools: potential and challenges, J. Archaeol. Sci. **41**, 732–739 (2014).

[56] P. Dumas, G. D. Sockalingum, and J. Sulé-Suso, Adding synchrotron radiation to infrared microspectroscopy: what's new in biomedical applications?, Trends Biotechnol. **25**, 40–44 (2007).

[57] M. J. Tobin, L. Puskar, R. L. Barber, E. C. Harvey, P. Heraud, B. R. Wood, K. R. Bambery, C. T. Dillon, and K. L. Munro, FTIR spectroscopy of single live cells in aqueous media by synchrotron IR microscopy using microfabricated sample holders, Vib. Spectrosc. **53**, 34–38 (2010).

[58] H.-Y. N. Holman, M. C. Martin, E. A. Blakely, K. Bjornstad, and W. R. Mckinney, IR spectroscopic characteristics of cell cycle and cell death probed by synchrotron radiation based Fourier transform IR spectromicroscopy, Biopolymers **57**, 329–335 (2000).

[59] L. Kreplak, F. Briki, Y. Duvault, J. Doucet, C. Merigoux, F. Leroy, J. L. Lévêque, L. Miller, G. L. Carr, et al., Profiling lipids across Caucasian and

Afro-American hair transverse cuts, using synchrotron infrared microspectrometry, Int. J. Cosmet. Sci. **23**, 369–374 (2001).

[60] M. Petra, J. Anastassopoulou, T. Theologis, and T. Theophanides, Synchrotron micro-FT-IR spectroscopic evaluation of normal paediatric human bone, J. Mol. Struct. **733**, 101–110 (2005).

[61] S. Schlücker, Surface-Enhanced Raman Spectroscopy: Concepts and Chemical Applications, Angew. Chem. Int. Ed. **53**, 4756–4795 (2014).

[62] P. G. Etchegoin and E. C. Le Ru, Basic Electromagnetic Theory of SERS, in Surf. Enhanc. Raman Spectrosc., S. Schlücker, Ed. (Wiley-VCH Verlag GmbH & Co. KGaA, 2010).

[63] R. Aroca, *Surface enhanced vibrational spectroscopy* (Wiley, Hoboken, NJ, 2006).

[64] E. C. L. Ru, S. A. Meyer, C. Artur, P. G. Etchegoin, J. Grand, P. Lang, and F. Maurel, Experimental demonstration of surface selection rules for SERS on flat metallic surfaces, Chem. Commun. **47**, 3903–3905 (2011).

[65] W. Xie and S. Schlücker, Medical applications of surface-enhanced Raman scattering, Phys. Chem. Chem. Phys. **15**, 5329–5344 (2013).

[66] T. Vo-Dinh, F. Yan, and M. B. Wabuyele, Surface-enhanced Raman scattering for medical diagnostics and biological imaging, J. Raman Spectrosc. **36**, 640–647 (2005).

[67] J. H. Granger, M. C. Granger, M. A. Firpo, S. J. Mulvihill, and M. D. Porter, Toward development of a surface-enhanced Raman scattering (SERS)-based cancer diagnostic immunoassay panel, Analyst **138**, 410–416 (2012).

[68] M. Li, S. K. Cushing, J. Zhang, S. Suri, R. Evans, W. P. Petros, L. F. Gibson, D. Ma, Y. Liu, et al., Three-Dimensional Hierarchical Plasmonic Nano-Architecture Enhanced Surface-Enhanced Raman Scattering Immunosensor for Cancer Biomarker Detection in Blood Plasma, ACS Nano **7**, 4967–4976 (2013).

[69] T.-L. Wang, H. K. Chiang, H.-H. Lu, and F.-Y. Peng, Semi-quantitative Surface Enhanced Raman Scattering Spectroscopic Creatinine Measurement in Human Urine Samples, Opt. Quantum Electron. **37**, 1415–1422 (2006).

[70] G. D. Mistro, S. Cervo, E. Mansutti, R. Spizzo, A. Colombatti, P. Belmonte, R. Zucconelli, A. Steffan, V. Sergo, et al., Surface-enhanced Raman spectroscopy of urine for prostate cancer detection: a preliminary study, Anal. Bioanal. Chem. **407**, 3271–3275 (2015).

[71] S. Feng, D. Lin, J. Lin, B. Li, Z. Huang, G. Chen, W. Zhang, L. Wang, J. Pan, et al., Blood plasma surface-enhanced Raman spectroscopy for non-invasive optical detection of cervical cancer, Analyst **138**, 3967–3974 (2013).

[72] F. Inscore, C. Shende, A. Sengupta, H. Huang, and S. Farquharson, Detection of Drugs of Abuse in Saliva by Surface-Enhanced Raman Spectroscopy (SERS), Appl. Spectrosc. **65**, 1004–1008 (2011).

[73] P. Hu, X.-S. Zheng, C. Zong, M.-H. Li, L.-Y. Zhang, W. Li, and B. Ren, Drop-coating deposition and surface-enhanced Raman spectroscopies (DCDRS and SERS) provide complementary information of whole human tears, J. Raman Spectrosc. **45**, 565–573 (2014).

[74] C. Leordean, V. Canpean, and S. Astilean, Surface-Enhanced Raman Scattering (SERS) Analysis of Urea Trace in Urine, Fingerprint, and Tear Samples, Spectrosc. Lett. **45**, 550–555 (2012).

[75] K. Kairyte, Z. Luksiene, M. Pucetaite, and V. Sablinskas, Differentiation of bacterial strains by means of surface enhanced FT-Raman spectroscopy, Lith. J. Phys. **52** (2012).

[76] H. Chu, Y. Huang, and Y. Zhao, Silver Nanorod Arrays as a Surface-Enhanced Raman Scattering Substrate for Foodborne Pathogenic Bacteria Detection, Appl. Spectrosc. **62**, 922–931 (2008).

[77] A. P. Craig, A. S. Franca, and J. Irudayaraj, Surface-Enhanced Raman Spectroscopy Applied to Food Safety, Annu. Rev. Food Sci. Technol. **4**, 369–380 (2013).

[78] H. Zhou, D. Yang, N. P. Ivleva, N. E. Mircescu, R. Niessner, and C. Haisch, SERS Detection of Bacteria in Water by in Situ Coating with Ag Nanoparticles, Anal. Chem. **86**, 1525–1533 (2014).

[79] J. Kneipp, H. Kneipp, A. Rajadurai, R. W. Redmond, and K. Kneipp, Optical probing and imaging of live cells using SERS labels, J. Raman Spectrosc. **40**, 1–5 (2009).

[80] M. V. Yigit and Z. Medarova, In vivo and ex vivo applications of gold nanoparticles for biomedical SERS imaging, Am J Nucl Med Mol Imaging **2**, 232–241 (2012).

[81] X. Qian, X.-H. Peng, D. O. Ansari, Q. Yin-Goen, G. Z. Chen, D. M. Shin, L. Yang, A. N. Young, M. D. Wang, et al., In vivo tumor targeting and spectroscopic detection with surface-enhanced Raman nanoparticle tags, Nat. Biotechnol. **26**, 83–90 (2008).

[82] J.-X. Cheng, Coherent Anti-Stokes Raman Scattering Microscopy, Appl. Spectrosc. **61**, 197–208 (2007).

[83] W. Min, C. W. Freudiger, S. Lu, and X. S. Xie, Coherent Nonlinear Optical Imaging: Beyond Fluorescence Microscopy, Annu. Rev. Phys. Chem. **62**, 507–530 (2011).

[84] A. Volkmer, J.-X. Cheng, and X. Sunney Xie, Vibrational Imaging with High Sensitivity via Epidetected Coherent Anti-Stokes Raman Scattering Microscopy, Phys. Rev. Lett. **87** (2001).

[85] J.-X. Cheng, L. D. Book, and X. S. Xie, Polarization coherent anti-Stokes Raman scattering microscopy, Opt. Lett. **26**, 1341–1343 (2001).

[86] F. Ganikhanov, C. L. Evans, B. G. Saar, and X. S. Xie, High-sensitivity vibrational imaging with frequency modulation coherent anti-Stokes

Raman scattering (FM CARS) microscopy, Opt. Lett. **31**, 1872–1874 (2006).

[87] E. O. Potma, C. L. Evans, and X. S. Xie, Heterodyne coherent anti-Stokes Raman scattering (CARS) imaging, Opt. Lett. **31**, 241–243 (2006).

[88] M. Jurna, J. P. Korterik, C. Otto, L. Herek, and H. L. Offerhaus, Background free CARS imaging by local phase detection, SPIE Proc. **7183**, 718310 (2009).

[89] J. P. Pezacki, J. A. Blake, D. C. Danielson, D. C. Kennedy, R. K. Lyn, and R. Singaravelu, Chemical contrast for imaging living systems: molecular vibrations drive CARS microscopy, Nat Chem Biol **7**, 137–145 (2011).

[90] C. L. Evans and X. S. Xie, Coherent Anti-Stokes Raman Scattering Microscopy: Chemical Imaging for Biology and Medicine, Annu. Rev. Anal. Chem. **1**, 883–909 (2008).

[91] T. T. Le, S. Yue, and J.-X. Cheng, Shedding new light on lipid biology with coherent anti-Stokes Raman scattering microscopy, J. Lipid Res. **51**, 3091–3102 (2010).

[92] F. Légaré, C. L. Evans, F. Ganikhanov, and X. S. Xie, Towards CARS Endoscopy, Opt. Express **14**, 4427–4432 (2006).

[93] Y. Wu, Y. Leng, J. Xi, and X. Li, Scanning all-fiber-optic endomicroscopy system for 3D nonlinear optical imaging of biological tissues, Opt. Express **17**, 7907–7915 (2009).

[94] O. Uckermann, R. Galli, S. Tamosaityte, E. Leipnitz, K. D. Geiger, G. Schackert, E. Koch, G. Steiner, and M. Kirsch, Label-Free Delineation of Brain Tumors by Coherent Anti-Stokes Raman Scattering Microscopy in an Orthotopic Mouse Model and Human Glioblastoma, PLOS ONE **9**, e107115 (2014).

[95] R. Galli, V. Sablinskas, D. Dasevicius, A. Laurinavicius, F. Jankevicius, E. Koch, and G. Steiner, Non-linear optical microscopy of kidney tumours, J. Biophotonics **7**, 23–27 (2014).

[96] R. C. Burruss, A. D. Slepkov, A. F. Pegoraro, and A. Stolow, Unraveling the complexity of deep gas accumulations with three-dimensional multimodal CARS microscopy, Geology **40**, 1063–1066 (2012).

[97] Z. Wang, W. Zheng, C.-Y. Stephen Hsu, and Z. Huang, Epi-detected quadruple-modal nonlinear optical microscopy for label-free imaging of the tooth, Appl. Phys. Lett. **106**, 33701 (2015).

[98] P. Lasch, Spectral pre-processing for biomedical vibrational spectroscopy and microspectroscopic imaging, Chemom. Intell. Lab. Syst. **117**, 100–114 (2012).

[99] H. Anton, *Elementary linear algebra* (Wiley, New York, 1987).

[100] J. K. Kauppinen, D. J. Moffatt, H. H. Mantsch, and D. G. Cameron, Fourier Self-Deconvolution: A Method for Resolving Intrinsically Overlapped Bands, Appl. Spectrosc. **35**, 271–276 (1981).

[101] A. de Juan, S. Piqueras, M. Maeder, T. Hancewicz, L. Duponchel, and R. Tauler, Chemometric Tools for Image Analysis, in Infrared Raman Spectrosc. Imaging, R. Salzer and H. W. Siesler, Eds. (Wiley-VCH Verlag GmbH & Co. KGaA, 2014).

[102] E. Mooi and M. Sarstedt, Cluster Analysis, in Concise Guide Mark. Res. (Springer Berlin Heidelberg, Berlin, Heidelberg, 2010).

[103] H. J. Byrne, P. Knief, M. E. Keating, and F. Bonnier, Spectral pre and post processing for infrared and Raman spectroscopy of biological tissues and cells, Chem. Soc. Rev. **45**, 1865–1878 (2016).

[104] H.-F. Lu, J.-B. Shen, X.-Y. Lin, and J.-L. Fu, Relevance of Fourier transform infrared spectroscopy and leaf anatomy for species classification in Camellia (Theaceae), Taxon **57** (2008).

[105] A. Matulis, *Kompleksiniai skaičiai ir funkcijos. Analizinių skaičiavimų menas,* (VU leidykla, Vilnius, 2005).

[106] B. J. Davis, P. S. Carney, and R. Bhargava, Theory of mid-infrared absorption microspectroscopy, Anal. Chem. **82** (2010).

[107] H. Heers and B. W. Turney, Trends in urological stone disease: a 5-year update of hospital episode statistics, BJU Int., n/a-n/a (2016).

[108] H. S. Bagga, T. Chi, J. Miller, and M. L. Stoller, New Insights Into the Pathogenesis of Renal Calculi, Urol. Clin. North Am. **40**, 1–12 (2013).

[109] A. Mangera, K. Khan, and B. T. Parys, Has the incidence of urolithiasis presenting to secondary care increased in the last 10 years?, J. Clin. Urol. **6**, 239–242 (2013).

[110] M. López and B. Hoppe, History, epidemiology and regional diversities of urolithiasis, Pediatr. Nephrol. **25**, 49–59 (2008).

[111] N. M. Mehmet and O. Ender, Effect of urinary stone disease and its treatment on renal function, World J. Nephrol. **4**, 271–276 (2015).

[112] V. Romero, H. Akpinar, and D. G. Assimos, Kidney Stones: A Global Picture of Prevalence, Incidence, and Associated Risk Factors, Rev. Urol. **12**, e86–e96 (2010).

[113] G. Bihl and A. Meyers, Recurrent renal stone disease—advances in pathogenesis and clinical management, The Lancet **358**, 651–656 (2001).

[114] F. Grases, A. Costa-Bauzá, M. Ramis, V. Montesinos, and A. Conte, Recurrence of renal lithiasis, Scand. J. Urol. Nephrol. **37**, 482–486 (2003).

[115] P. M. Ferraro, G. C. Curhan, A. D'Addessi, and G. Gambaro, Risk of recurrence of idiopathic calcium kidney stones: analysis of data from the literature, J. Nephrol., 1–7 (2016).

[116] F. L. Coe, A. Evan, and E. Worcester, Kidney stone disease, J. Clin. Invest. **115**, 2598–2608 (2005).

[117] M. Daudon and P. Jungers, Stone Composition and Morphology: A Window on Etiology, in Urolithiasis, J. J. Talati, H.-G. Tiselius, D. M. Albala, and Z. YE, Eds. (Springer London, 2012).

[118] J. P. Kavanagh, Physicochemical Aspects of Uro-crystallization and Stone Formation, in Urin. Tract Stone Dis., N. P. Rao, G. M. Preminger, and J. P. Kavanagh, Eds. (Springer London, 2010).

[119] G. Schubert, Urinary Stone Analysis, in Urin. Tract Stone Dis., N. P. Rao, G. M. Preminger, and J. P. Kavanagh, Eds. (Springer London, London, 2010).

[120] L. Larsson, B. Sörbo, H.-G. Tiselius, and S. Öhman, A method for quantitative wet chemical analysis of urinary calculi, Clin. Chim. Acta **140**, 9–20 (1984).

[121] R. N. Sharma, I. Shah, S. Gupta, P. Sharma, and A. A. Beigh, Thermogravimetric Analysis of Urinary Stones, Br. J. Urol. **64**, 564–566 (1989).

[122] P. A. Bhatt and P. Paul, Analysis of urinary stone constituents using powder X-ray diffraction and FT-IR, J. Chem. Sci. **120**, 267–273 (2008).

[123] B. G, S. G, and B. C, 10,000 analyses of urinary calculi using X-ray diffraction and polarizing microscopy., Eur. Urol. **8**, 251–256 (1981).

[124] K. Štěpánková, K. Novotný, M. Vašinová Galiová, V. Kanický, J. Kaiser, and D. W. Hahn, Laser ablation methods for analysis of urinary calculi: Comparison study based on calibration pellets, Spectrochim. Acta Part B At. Spectrosc. **81**, 43–49 (2013).

[125] J. Anzano and R.-J. Lasheras, Strategies for the identification of urinary calculus by laser induced breakdown spectroscopy, Talanta **79**, 352–360 (2009).

[126] G. Hidas, R. Eliahou, M. Duvdevani, P. Coulon, L. Lemaitre, O. N. Gofrit, D. Pode, and J. Sosna, Determination of Renal Stone Composition with Dual-Energy CT: In Vivo Analysis and Comparison with X-ray Diffraction, Radiology **257**, 394–401 (2010).

[127] V. S. Joshi, S. R. Vasant, J. G. Bhatt, and M. J. Joshi, Some critical aspects of FT-IR, TGA, powder XRD, EDAX and SEM studies of calcium oxalate urinary calculi, Indian J Biochem Biophys **51**, 237–43 (2014).

[128] J. R. Guerra-López, J. A. Güida, and C. O. D. Védova, Infrared and Raman studies on renal stones: the use of second derivative infrared spectra, Urol. Res. **38**, 383–390 (2010).

[129] R. Selvaraju, A. Raja, and G. Thiruppathi, FT-Raman spectral analysis of human urinary stones, Spectrochim. Acta. A. Mol. Biomol. Spectrosc. **99**, 205–210 (2012).

[130] A. Spek, F. Strittmatter, A. Graser, P. Kufer, C. Stief, and M. Staehler, Dual energy can accurately differentiate uric acid-containing urinary calculi from calcium stones, World J. Urol., 1–6 (2016).

[131] G. Schubert, Stone analysis, Urol. Res. **34**, 146–150 (2006).

[132] S. D. Blaschko, J. Miller, T. Chi, L. Flechner, S. Fakra, A. Kahn, P. Kapahi, and M. L. Stoller, Microcomposition of Human Urinary Calculi Using Advanced Imaging Techniques, J. Urol. **189**, 726–734 (2013).

[133] M. Daudon, D. Bazin, and E. Letavernier, Randall's plaque as the origin of calcium oxalate kidney stones, Urolithiasis **43**, 5–11 (2015).

[134] M. Daudon and D. Bazin, When the Synchrotron radiations highlight the Randall's plaques and kidney concretions, J. Phys. Conf. Ser. **425**, 22006 (2013).

[135] H.-G. Tiselius, The role of calcium phosphate in the development of Randall's plaques, Urolithiasis **41**, 369–377 (2013).

[136] M. Daudon, O. Traxer, P. Jungers, and D. Bazin, Stone Morphology Suggestive of Randall's Plaque, AIP Conf. Proc. **200(26)**, 26–34 (2007).

[137] I. Singh, Renal geology (quantitative renal stone analysis) by 'Fourier transform infrared spectroscopy,' Int. Urol. Nephrol. **40**, 595–602 (2008).

[138] Z. Jing, W. GuoZeng, J. Ning, Y. JiaWei, G. Yan, and Y. Fang, Analysis of urinary calculi composition by infrared spectroscopy: a prospective study of 625 patients in eastern China, Urol. Res. **38**, 111–115 (2010).

[139] M. Daudon, C. Hennequin, B. Lacour, G. L. Moel, R. Donsimoni, S. Fellahi, M. Paris, and S. Troupel, Sex- and age-related composition of 10 617 calculi analyzed by infrared spectroscopy, Urol. Res. **23**, 319–326 (1995).

[140] R. Selvaraju, A. Raja, and G. Thiruppathi, FT-IR spectroscopic, thermal analysis of human urinary stones and their characterization, Spectrochim. Acta. A. Mol. Biomol. Spectrosc. **137**, 1397–1402 (2015).

[141] L. Benramdane, M. Bouatia, M. O. B. Idrissi, and M. Draoui, Infrared Analysis of Urinary Stones, Using a Single Reflection Accessory and a KBr Pellet Transmission, Spectrosc. Lett. **41**, 72–80 (2008).

[142] H. J. Gulley-Stahl, J. A. Haas, K. A. Schmidt, A. P. Evan, and A. J. Sommer, Attenuated Total Internal Reflection Fourier Transform Infrared Spectroscopy: A Quantitative Approach for Kidney Stone Analysis, Appl. Spectrosc. **63**, 759–766 (2009).

[143] M. Volmer, J. C. M. de Vries, and H. M. J. Goldschmidt, Infrared Analysis of Urinary Calculi by a Single Reflection Accessory and a Neural Network Interpretation Algorithm, Clin. Chem. **47**, 1287–1296 (2001).

[144] M. Daudon, P. Jungers, and D. Bazin, Stone Morphology: Implication for Pathogenesis, AIP Conf. Proc. **1049**, (2008).

[145] J. Cloutier, L. Villa, O. Traxer, and M. Daudon, Kidney stone analysis: “Give me your stone, I will tell you who you are!,” World J. Urol. **33**, 157–169 (2015).

[146] A. Boskey and N. Pleshko Camacho, FT-IR imaging of native and tissue-engineered bone and cartilage, Biomaterials **28**, 2465–2478 (2007).

[147] F. Blanco, P. Ortiz-Alías, M. López-Mesas, and M. Valiente, High precision mapping of kidney stones using μ-IR spectroscopy to determine urinary lithogenesis, J. Biophotonics **8**, 457–465 (2015).

[148] S. K. Khalil and M. A. Azooz, Application of vibrational spectroscopy in identification of the composition of the urinary stones, J Appl Sci Res **3**, 387–391 (2007).

[149] A. Miernik, Y. Eilers, C. Nuese, C. Bolwien, A. Lambrecht, A. Hesse, J. J. Rassweiler, D. Schlager, K. Wilhelm, et al., Is in vivo analysis of urinary stone composition feasible? Evaluation of an experimental setup of a Raman system coupled to commercial lithotripsy laser fibers, World J. Urol. **33**, 1593–1599 (2015).

[150] Y.-C. Chiu, H.-Y. Yang, S.-H. Lu, and H. K. Chiang, Micro-Raman spectroscopy identification of urinary stone composition from ureteroscopic lithotripsy urine powder, J. Raman Spectrosc. **41**, 136–141 (2010).

[151] A. Miernik, Y. Eilers, C. Bolwien, A. Lambrecht, D. Hauschke, G. Rebentisch, P. S. Lossin, A. Hesse, J. J. Rassweiler, et al., Automated Analysis of Urinary Stone Composition Using Raman Spectroscopy: Pilot Study for the Development of a Compact Portable System for Immediate Postoperative Ex Vivo Application, J. Urol. **190**, 1895–1900 (2013).

[152] http://webbook.nist.gov/chemistry/ (3 June 2016).

[153] http://rruff.info/ (3 June 2016).

[154] W. R. Hunter, Errors in using the Reflectance vs Angle of Incidence Method for Measuring Optical Constants, JOSA **55**, 1197–1204 (1965).

[155] C. Conti, M. Casati, C. Colombo, M. Realini, L. Brambilla, and G. Zerbi, Phase transformation of calcium oxalate dihydrate–monohydrate: Effects of relative humidity and new spectroscopic data, Spectrochim. Acta. A. Mol. Biomol. Spectrosc. **128**, 413–419 (2014).

[156] T. Knoll, A. B. Schubert, D. Fahlenkamp, D. B. Leusmann, G. Wendt-Nordahl, and G. Schubert, Urolithiasis Through the Ages: Data on More Than 200,000 Urinary Stone Analyses, J. Urol. **185**, 1304–1311 (2011).

[157] C. D. Scales, A. C. Smith, J. M. Hanley, and C. S. Saigal, Prevalence of Kidney Stones in the United States, Eur. Urol. **62**, 160–165 (2012).

[158] G. Foster, C. Stocks, and M. S. Borofsky, Emergency department visits and hospital admissions for kidney stone disease, 2009, Statistical Brief **139**, (2012).

[159] L. M. Miller, G. D. Smith, and G. L. Carr, Synchrotron-based Biological Microspectroscopy: From the Mid-Infrared through the Far-Infrared Regimes, J. Biol. Phys. **29**, 219–230 (2003).

[160] R. L. Frost, J. Yang, and Z. Ding, Raman and FTIR spectroscopy of natural oxalates: Implications for the evidence of life on Mars, Chin. Sci. Bull. **48**, 1844–1852 (2003).

[161] G. Vasuki and R. Selvaraju, Growth and Characterization of Uric Acid Crystals, International Journal of Science and Research **3(8)**, 696-699 (2014).

[162] B. L. Goodall, A. M. Robinson, and C. L. Brosseau, Electrochemical-surface enhanced Raman spectroscopy (E-SERS) of uric acid: a potential rapid diagnostic method for early preeclampsia detection, Phys. Chem. Chem. Phys. PCCP **15**, 1382–1388 (2013).

[163] J. Shi, A. Klocke, M. Zhang, and U. Bismayer, Thermal behavior of dental enamel and geologic apatite: An infrared spectroscopic study, Am. Mineral. **88**, 1866–1871 (2003).

[164] L. Berzina-Cimdina and N. Borodajenko, *Research of calcium phosphates using Fourier transform infrared spectroscopy* (INTECH Open Access Publisher, 2012).

[165] C. Rey, M. Shimizu, B. Collins, and M. J. Glimcher, Resolution-enhanced fourier transform infrared spectroscopy study of the environment of

phosphate ions in the early deposits of a solid phase of calcium-phosphate in bone and enamel, and their evolution with age. I: Investigations in thev 4 PO4 domain, Calcif. Tissue Int. **46**, 384–394 (1990).

[166] V. Stefov, B. Šoptrajanov, F. Spirovski, I. Kuzmanovski, H. . Lutz, and B. Engelen, Infrared and Raman spectra of magnesium ammonium phosphate hexahydrate (struvite) and its isomorphous analogues. I. Spectra of protiated and partially deuterated magnesium potassium phosphate hexahydrate, J. Mol. Struct. **689**, 1–10 (2004).

[167] S. Popescu, M. Stefanescu, E. Popovici, and I. Perhaita, Evaluation of the renal calculi compositions, J. Therm. Anal. Calorim. **114**, 765–775 (2013).

[168] J. A. DeSanto, Overview of Rough Surface Scattering, in Light Scatt. Nanoscale Surf. Rough., A. A. Maradudin, Ed. (Springer US, 2007).

[169] A. K. Chandra and T. Zeegers-Huyskens, Theoretical study of the acidity and basicity of uric acid and its interaction with water, J. Mol. Struct. THEOCHEM **811**, 215–221 (2007).

[170] John. C. Russ, *The Image Processing Handbook, 6th edition*, (Taylor & Francis Group, Boca Raton, 2011), Chapter 5, p.p. 320-323.

[171] H. G. M. Edwards, D. W. Farwell, and M. R. D. Seaward, Raman spectra of oxalates in lichen encrustations on Renaissance frescoes, Spectrochim. Acta Part Mol. Spectrosc. **47**, 1531–1539 (1991).

[172] J. Prywer, A. Torzewska, and T. Płociński, Unique surface and internal structure of struvite crystals formed by Proteus mirabilis, Urol. Res. **40**, 699–707 (2012).

[173] R. L. Frost and M. L. Weier, Thermal treatment of whewellite—a thermal analysis and Raman spectroscopic study, Thermochim. Acta **409**, 79–85 (2004).

[174] X. Sheng, T. Jung, J. A. Wesson, and M. D. Ward, Adhesion at calcium oxalate crystal surfaces and the effect of urinary constituents, Proc. Natl. Acad. Sci. U. S. A. **102**, 267–272 (2005).

[175] R. Shirley and D. J. Sutor, Anhydrous Uric Acid: Nature and Occurrence of a New Form in Urinary Calculi, Science **159**, 544–544 (1968).

[176] F. Grases, P. Sanchis, J. Perelló, and A. Costa-Bauzá, Role of uric acid in different types of calcium oxalate renal calculi, Int. J. Urol. **13**, 252–256 (2006).

[177] J. Gao, J.-F. Xue, M. Xu, B.-S. Gui, F.-X. Wang, and J.-M. Ouyang, Comparison of Physicochemical Properties of Nano- and Microsized Crystals in the Urine of Calcium Oxalate Stone Patients and Control Subjects, J Nanomater. **2014**, 49:49–49:49 (2014).

[178] K. Kohri, T. Yasui, A. Okada, M. Hirose, S. Hamamoto, Y. Fujii, K. Niimi, and K. Taguchi, Biomolecular mechanism of urinary stone formation involving osteopontin, Urol. Res. **40**, 623–637 (2012).

[179] K. P. Aggarwal, S. Tandon, P. K. Naik, S. K. Singh, and C. Tandon, Peeping into Human Renal Calcium Oxalate Stone Matrix: Characterization of Novel Proteins Involved in the Intricate Mechanism of Urolithiasis, PLOS ONE **8**, e69916 (2013).

[180] M. A. Warpehoski, P. J. Buscemi, D. C. Osborn, B. Finlayson, and E. P. Goldberg, Distribution of organic matrix in calcium oxalate renal calculi, Calcif. Tissue Int. **33**, 211–222 (1981).

[181] M. Pucetaite, V. Hendrixson, A. Zelvys, F. Jankevicius, R. Tyla, J. Ceponkus, and V. Sablinskas, Application of infrared spectroscopic imaging in specular reflection mode for determination of distribution of chemical components in urinary stones, J. Mol. Struct. **1031**, 38–42 (2013).

[182] M. Pucetaite, S. Tamosaityte, A. Engdahl, J. Ceponkus, V. Sablinskas, and P. Uvdal, Microspectroscopic infrared specular reflection chemical

imaging of multi-component urinary stones: MIR vs. FIR, Cent. Eur. J. Chem. **12**, 44–52 (2013).

[183] J. Y. He, S. P. Deng, and J. M. Ouyang, Morphology, Particle Size Distribution, Aggregation, and Crystal Phase of Nanocrystallites in the Urine of Healthy Persons and Lithogenic Patients, IEEE Trans. NanoBioscience **9**, 156–163 (2010).

[184] Y. M. F. Marickar and A. Salim, Photmicrography of urinary deposits in stone clinic, Urol. Res. **37**, 359–368 (2009).

[185] M. Daudon, C. Marfisi, B. Lacour, and C. Bader, Investigation of urinary crystals by Fourier transform infrared microscopy., Clin. Chem. **37**, 83–87 (1991).

[186] Z. Kaid-Omar, M. Daudon, A. Attar, A. Semmoud, B. Lacour, A. Addou, and others, Corrélation entre cristalluries et composition des calculs, Prog. En Urol. **9**, 633–641 (1999).

[187] S. Verdesca, G. B. Fogazzi, G. Garigali, P. Messa, and M. Daudon, Crystalluria: prevalence, different types of crystals and the role of infrared spectroscopy, Clin. Chem. Lab. Med. **49**, 515–520 (2010).

[188] A. Gul and P. Rez, Models for protein binding to calcium oxalate surfaces, Urol. Res. **35**, 63–71 (2007).

[189] T. C. Ngo and D. G. Assimos, Uric Acid Nephrolithiasis: Recent Progress and Future Directions, Rev. Urol. **9**, 17–27 (2007).

[190] W. L. Strohmaier, J. Seilnacht, and G. Schubert, Clinical significance of uric acid dihydrate in urinary stones, Urol. Res. **39**, 357–360 (2011).

[191] https://labtestsonline.org/understanding/analytes/body-fluid/tab/glance/ (3 June 2016).

[192] R. Mayeux, Biomarkers: Potential Uses and Limitations, NeuroRX **1**, 182–188 (2004).

[193] A. Sevinc, D. Yonar, and F. Severcan, Investigation of neurodegenerative diseases from body fluid samples using Fourier transform infrared spectroscopy, Biomed. Spectrosc. Imaging **4**, 341–357 (2015).

[194] J. Ollesch, S. L. Drees, H. M. Heise, T. Behrens, T. Brüning, and K. Gerwert, FTIR spectroscopy of biofluids revisited: an automated approach to spectral biomarker identification, Analyst **138**, 4092–4102 (2013).

[195] L. Lovergne, P. Bouzy, V. Untereiner, R. Garnotel, M. J. Baker, G. Thiéfin, and G. D. Sockalingum, Biofluid infrared spectro-diagnostics: pre-analytical considerations for clinical applications, Faraday Discuss. (2015).

[196] A. Bonifacio, S. Cervo, and V. Sergo, Label-free surface-enhanced Raman spectroscopy of biofluids: fundamental aspects and diagnostic applications, Anal. Bioanal. Chem. **407**, 8265–8277 (2015).

[197] H. Wang and S. Zou, A generalized electrodynamics model for surface enhanced Raman scattering and enhanced/quenched fluorescence calculations, RSC Adv. **3**, 21489–21493 (2013).

[198] G. McNay, D. Eustace, W. E. Smith, K. Faulds, and D. Graham, Surface-Enhanced Raman Scattering (SERS) and Surface-Enhanced Resonance Raman Scattering (SERRS): A Review of Applications, Appl. Spectrosc. **65**, 825–837 (2011).

[199] B. N. Ames, R. Cathcart, E. Schwiers, and P. Hochstein, Uric acid provides an antioxidant defense in humans against oxidant- and radical-caused aging and cancer: a hypothesis, Proc. Natl. Acad. Sci. U. S. A. **78**, 6858–6862 (1981).

[200] B. F. Becker, Towards the physiological function of uric acid, Free Radic. Biol. Med. **14**, 615–631 (1993).

[201] F. J. Nieto, C. Iribarren, M. D. Gross, G. W. Comstock, and R. G. Cutler, Uric acid and serum antioxidant capacity: a reaction to atherosclerosis?, Atherosclerosis **148**, 131–139 (2000).

[202] D. I. Feig, M. Mazzali, D.-H. Kang, T. Nakagawa, K. Price, J. Kannelis, and R. J. Johnson, Serum Uric Acid: A Risk Factor and a Target for Treatment?, J. Am. Soc. Nephrol. **17**, S69–S73 (2006).

[203] K.-H. Yu, S.-F. Luo, W.-P. Tsai, and Y.-Y. Huang, Intermittent elevation of serum urate and 24-hour urinary uric acid excretion, Rheumatology **43**, 1541–1545 (2004).

[204] N. Misra, V. Kumar, L. Borde, and L. Varshney, Localized surface plasmon resonance-optical sensors based on radiolytically synthesized silver nanoparticles for estimation of uric acid, Sens. Actuators B Chem. **178**, 371–378 (2013).

[205] S. A. Bainbridge, F. von Versen-Höynck, and J. M. Roberts, Uric acid inhibits placental system A amino acid uptake, Placenta **30**, 195–200 (2009).

[206] D. I. Feig, D.-H. Kang, and R. J. Johnson, Uric Acid and Cardiovascular Risk, N. Engl. J. Med. **359**, 1811–1821 (2008).

[207] G. Bellomo, S. Venanzi, C. Verdura, P. Saronio, A. Esposito, and M. Timio, Association of uric acid with change in kidney function in healthy normotensive individuals, Am. J. Kidney Dis. Off. J. Natl. Kidney Found. **56**, 264–272 (2010).

[208] J. Galbán, Y. Andreu, M. J. Almenara, S. de Marcos, and J. R. Castillo, Direct determination of uric acid in serum by a fluorometric-enzymatic method based on uricase, Talanta **54**, 847–854 (2001).

[209] H. M. KALCKAR and A. N. BESSMANN, Differential spectrophotometry of purine compounds by means of specific enzymes. 2. Determination of adenine compounds., J. Biol. Chem. **167**, 445–459 (1947).

[210] J. Zhao, Simultaneous determination of plasma creatinine, uric acid, kynurenine and tryptophan by high-performance liquid chromatography: method validation and in application to the assessment of renal function, Biomed. Chromatogr. **29**, 410–415 (2015).

[211] L. Zhao, J. Blackburn, and C. L. Brosseau, Quantitative Detection of Uric Acid by Electrochemical-Surface Enhanced Raman Spectroscopy Using a Multilayered Au/Ag Substrate, Anal. Chem. **87**, 441–447 (2015).

[212] K. Tan, G. Yang, H. Chen, P. Shen, Y. Huang, and Y. Xia, Facet dependent binding and etching: Ultra-sensitive colorimetric visualization of blood uric acid by unmodified silver nanoprisms, Biosens. Bioelectron. **59**, 227–232 (2014).

[213] A. Bonifacio, S. D. Marta, R. Spizzo, S. Cervo, A. Steffan, A. Colombatti, and V. Sergo, Surface-enhanced Raman spectroscopy of blood plasma and serum using Ag and Au nanoparticles: a systematic study, Anal. Bioanal. Chem. **406**, 2355–2365 (2014).

[214] P. C. Lee and D. Meisel, Adsorption and surface-enhanced Raman of dyes on silver and gold sols, J. Phys. Chem. **86**, 3391–3395 (1982).

[215] N. Leopold and B. Lendl, A New Method for Fast Preparation of Highly Surface-Enhanced Raman Scattering (SERS) Active Silver Colloids at Room Temperature by Reduction of Silver Nitrate with Hydroxylamine Hydrochloride, J. Phys. Chem. B **107**, 5723–5727 (2003).

[216] D. Aherne, D. M. Ledwith, M. Gara, and J. M. Kelly, Optical Properties and Growth Aspects of Silver Nanoprisms Produced by a Highly Reproducible and Rapid Synthesis at Room Temperature, Adv. Funct. Mater. **18**, 2005–2016 (2008).

[217] M. Frisch, G. Trucks, H. Schlegel, G. Scuseria, M. Robb, J. Cheeseman, G. Scalmani, V. Barone, B. Mennucci, et al., Gaussian 09, Revision B.01, Gaussian 09 Revis. B01 Gaussian Inc Wallingford CT (2009).

[218] R. Dennington, T. Keith, and J. Millam, GaussView, Version 5, Semichem Inc., Shawnee Mission, KS, (2009).

[219] M. Altarsha, G. Monard, and B. Castro, Comparative semiempirical and ab initio study of the structural and chemical properties of uric acid and its anions, Int. J. Quantum Chem. **107**, 172–181 (2007).

[220] A. F. Routh, Drying of thin colloidal films, Rep. Prog. Phys. **76**, 46603 (2013).

[221] R. D. Deegan, Pattern formation in drying drops, Phys. Rev. E **61**, 475–485 (2000).

[222] P. Šimáková, M. Procházka, Ko&#x10d, i&#x161, ov&#xE1, E, P. ŠimákoP. Šimáková, M. Procházka, E, P. Šimáková, M. Procházka, et al., SERS Microspectroscopy of Biomolecules on Dried Ag Colloidal Drops, J. Spectrosc. J. Spectrosc. **27**, **27**, 449, 449–453, 453 (2012).

[223] P. J. Yunker, T. Still, M. A. Lohr, and A. G. Yodh, Suppression of the coffee-ring effect by shape-dependent capillary interactions, Nature **476**, 308–311 (2011).

[224] X. Shen, C.-M. Ho, and T.-S. Wong, Minimal Size of Coffee Ring Structure, J. Phys. Chem. B **114**, 5269–5274 (2010).

[225] D. J. Harris, H. Hu, J. C. Conrad, and J. A. Lewis, Patterning Colloidal Films via Evaporative Lithography, Phys. Rev. Lett. **98**, 148301 (2007).

[226] L. Cui, J. Zhang, X. Zhang, L. Huang, Z. Wang, Y. Li, H. Gao, S. Zhu, T. Wang, et al., Suppression of the Coffee Ring Effect by Hydrosoluble Polymer Additives, ACS Appl. Mater. Interfaces **4**, 2775–2780 (2012).

[227] B. Michen, C. Geers, D. Vanhecke, C. Endes, B. Rothen-Rutishauser, S. Balog, and A. Petri-Fink, Avoiding drying-artifacts in transmission electron microscopy: Characterizing the size and colloidal state of nanoparticles, Sci. Rep. **5** (2015).

[228] Y. Xie, S. Guo, C. Guo, M. He, D. Chen, Y. Ji, Z. Chen, X. Wu, Q. Liu, et al., Controllable Two-Stage Droplet Evaporation Method and Its

Nanoparticle Self-Assembly Mechanism, Langmuir **29**, 6232–6241 (2013).

[229] L.-Q. Lu, Y. Zheng, W.-G. Qu, H.-Q. Yu, and A.-W. Xu, Hydrophobic Teflon films as concentrators for single-molecule SERS detection, J. Mater. Chem. **22**, 20986 (2012).

[230] T. A. H. Nguyen, M. A. Hampton, and A. V. Nguyen, Evaporation of Nanoparticle Droplets on Smooth Hydrophobic Surfaces: The Inner Coffee Ring Deposits, J. Phys. Chem. C **117**, 4707–4716 (2013).

[231] M. Parsa, S. Harmand, K. Sefiane, M. Bigerelle, and R. Deltombe, Effect of Substrate Temperature on Pattern Formation of Nanoparticles from Volatile Drops, Langmuir **31**, 3354–3367 (2015).

[232] L. Mulfinger, S. D. Solomon, M. Bahadory, A. V. Jeyarajasingam, S. A. Rutkowsky, and C. Boritz, Synthesis and study of silver nanoparticles, J Chem Educ **84**, 322 (2007).

[233] H. Hu and R. G. Larson, Analysis of the Microfluid Flow in an Evaporating Sessile Droplet, Langmuir **21**, 3963–3971 (2005).

[234] E. C. Le Ru, E. Blackie, M. Meyer, and P. G. Etchegoin, Surface Enhanced Raman Scattering Enhancement Factors: A Comprehensive Study, J. Phys. Chem. C **111**, 13794–13803 (2007).

[235] X. Li, W. Xu, J. Zhang, H. Jia, B. Yang, B. Zhao, B. Li, and Y. Ozaki, Self-Assembled Metal Colloid Films: Two Approaches for Preparing New SERS Active Substrates, Langmuir **20**, 1298–1304 (2004).

[236] N. Pazos-Pérez, W. Ni, A. Schweikart, R. A. Alvarez-Puebla, A. Fery, and L. M. Liz-Marzán, Highly uniform SERS substrates formed by wrinkle-confined drying of gold colloids, Chem. Sci. **1**, 174–178 (2010).

[237] A. Saha, S. Palmal, and N. R. Jana, Highly reproducible and sensitive surface-enhanced Raman scattering from colloidal plasmonic nanoparticle via stabilization of hot spots in graphene oxide liquid crystal, Nanoscale **4**, 6649–6657 (2012).

[238] F. S. Ameer, W. Hu, S. M. Ansar, K. Siriwardana, W. E. Collier, S. Zou, and D. Zhang, Robust and Reproducible Quantification of SERS Enhancement Factors Using a Combination of Time-Resolved Raman Spectroscopy and Solvent Internal Reference Method, J. Phys. Chem. C **117**, 3483–3488 (2013).

[239] M. Pucetaite, M. Velicka, S. Tamosaityte, and V. Sablinskas, Application of SERS spectroscopy for detection of trace components in urinary deposits, SPIE Proc. **895708**, 895708–8 (2014).

[240] http://www.who.int/mediacentre/factsheets/fs297/en/ (2 June 2016).

[241] http://cancerguide.org/basic.html (2 June 2016).

[242] L. H. Sobin, M. K. Gospodarowicz, and C. Wittekind, *TNM Classification of Malignant Tumours* (John Wiley & Sons, 2011).

[243] P. Guinan, L. H. Sobin, F. Algaba, F. Badellino, S. Kameyama, G. MacLennan, and A. Novick, TNM staging of renal cell carcinoma, Cancer **80**, 992–993 (1997).

[244] http://urology.ucla.edu/more-about-kidney-cancer#rcc (2 June 2016).

[245] C. V. Thakar and K. Gaitonde, Kidney Function and Injury After Nephrectomy for Kidney Cancer, in Perioper. Kidney Inj., C. V. Thakar and C. R. Parikh, Eds. (Springer New York, 2015).

[246] M. V. Brown, J. E. McDunn, P. R. Gunst, E. M. Smith, M. V. Milburn, D. A. Troyer, and K. A. Lawton, Cancer detection and biopsy classification using concurrent histopathological and metabolomic analysis of core biopsies, Genome Med. **4**, 33 (2012).

[247] G. Steiner and M. Kirsch, Optical spectroscopic methods for intraoperative diagnosis, Anal. Bioanal. Chem. **406**, 21–25 (2014).

[248] O. J. Old, L. M. Fullwood, R. Scott, G. R. Lloyd, L. M. Almond, N. A. Shepherd, N. Stone, H. Barr, and C. Kendall, Vibrational spectroscopy for cancer diagnostics, Anal. Methods **6**, 3901–3917 (2014).

[249] L. Dong, X. Sun, Z. Chao, S. Zhang, J. Zheng, R. Gurung, J. Du, J. Shi, Y. Xu, et al., Evaluation of FTIR spectroscopy as diagnostic tool for colorectal cancer using spectral analysis, Spectrochim. Acta. A. Mol. Biomol. Spectrosc. **122**, 288–294 (2014).

[250] A. Benard, C. Desmedt, M. Smolina, P. Szternfeld, M. Verdonck, G. Rouas, N. Kheddoumi, F. Rothé, D. Larsimont, et al., Infrared imaging in breast cancer: automated tissue component recognition and spectral characterization of breast cancer cells as well as the tumor microenvironment, Analyst **139**, 1044–1056 (2014).

[251] B. Bird, Milo&sbreve, Miljković, S. Remiszewski, A. Akalin, M. Kon, and M. Diem, Infrared spectral histopathology (SHP): a novel diagnostic tool for the accurate classification of lung cancer, Lab. Invest. **92**, 1358–1373 (2012).

[252] T. J. Fairchild and P. A. Fournier, Glycogen determination using periodic acid-schiff: artifact of muscle preparation, Med. Sci. Sports Exerc. **36**, 2053–2058 (2004).

[253] R. G. Jones and C. B. Thompson, Tumor suppressors and cell metabolism: a recipe for cancer growth, Genes Dev. **23**, 537–548 (2009).

[254] H. Wiig and M. A. Swartz, Interstitial Fluid and Lymph Formation and Transport: Physiological Regulation and Roles in Inflammation and Cancer, Physiol. Rev. **92**, 1005–1060 (2012).

[255] C. R. Santos and A. Schulze, Lipid metabolism in cancer, FEBS J. **279**, 2610–2623 (2012).

[256] R. J. Gillies, I. Robey, and R. A. Gatenby, Causes and Consequences of Increased Glucose Metabolism of Cancers, J. Nucl. Med. **49**, 24S–42S (2008).

[257] C. E. Zois, E. Favaro, and A. L. Harris, Glycogen metabolism in cancer, Biochem. Pharmacol. **92**, 3–11 (2014).

[258] V. Urboniene, M. Pucetaite, F. Jankevicius, A. Zelvys, V. Sablinskas, and G. Steiner, Identification of kidney tumor tissue by infrared spectroscopy of extracellular matrix, J. Biomed. Opt. **19**, 87005 (2014).

[259] Z. Bar-Joseph, D. K. Gifford, and T. S. Jaakkola, Fast optimal leaf ordering for hierarchical clustering, Bioinforma. Oxf. Engl. **17 Suppl 1**, S22-29 (2001).

[260] A. Barth, Infrared spectroscopy of proteins, Biochim. Biophys. Acta BBA - Bioenerg. **1767**, 1073–1101 (2007).

[261] M. Diem, M. Miljković, B. Bird, A. I. Mazur, J. M. Schubert, D. Townsend, N. Laver, M. Almond, and O. Old, Cancer screening via infrared spectral cytopathology (SCP): results for the upper respiratory and digestive tracts, Analyst **141**, 416–428 (2016).

[262] O. Warburg, On the Origin of Cancer Cells, Science **123**, 309–314 (1956).

[263] A. G. Lalkhen and A. McCluskey, Clinical tests: sensitivity and specificity, Contin. Educ. Anaesth. Crit. Care Pain **8**, 221–223 (2008).

Appendix I

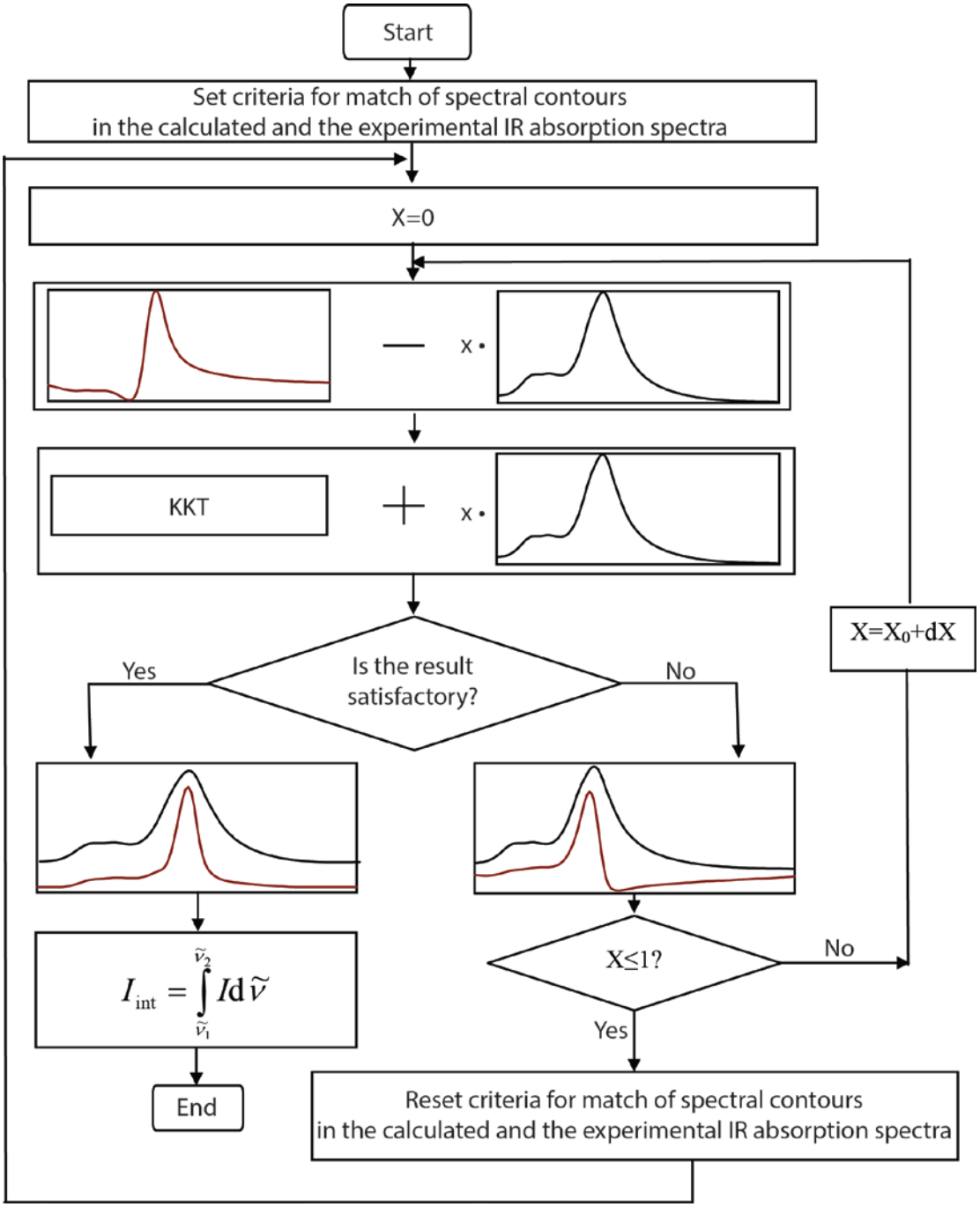

Fig. AI-1. Block scheme of the procedure of diffuse reflection subtraction from the experimental reflectance spectra.

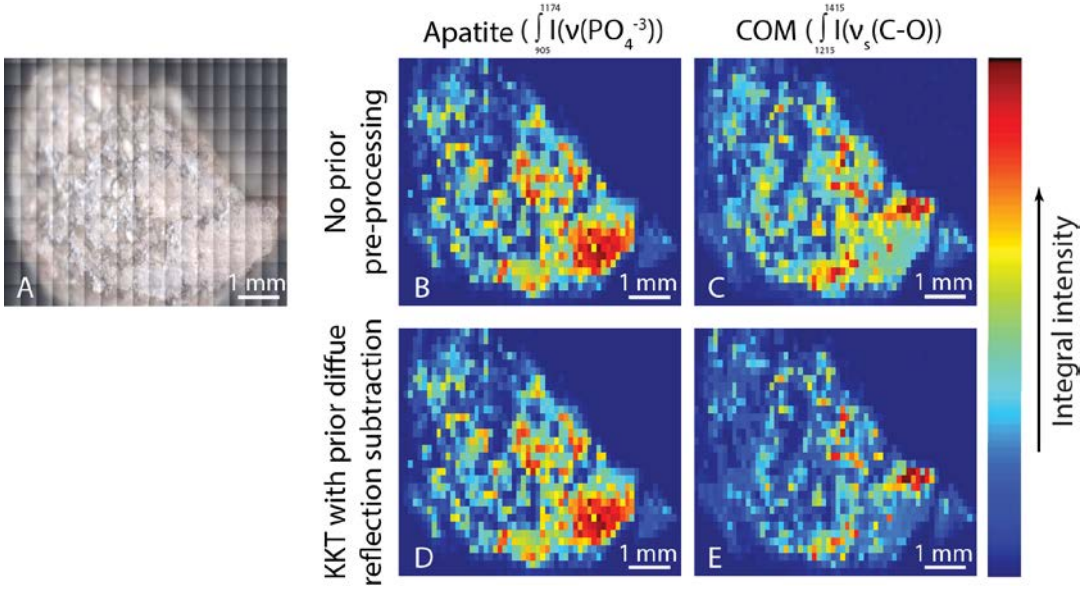

Fig. AI-2. Optical (A) and IR chemical (B-E) images of urinary stone constituted from apatite and COM. (B) and (C) shows distribution of apatite and COM respectively as determined by calculating integral intensity of characteristic spectral bands in the raw spectra; (D) and (E) shows distribution of apatite and COM respectively as determined by calculating integral intensity of characteristic spectral bands in the KKT corrected spectra after the subtraction of diffuse reflection.

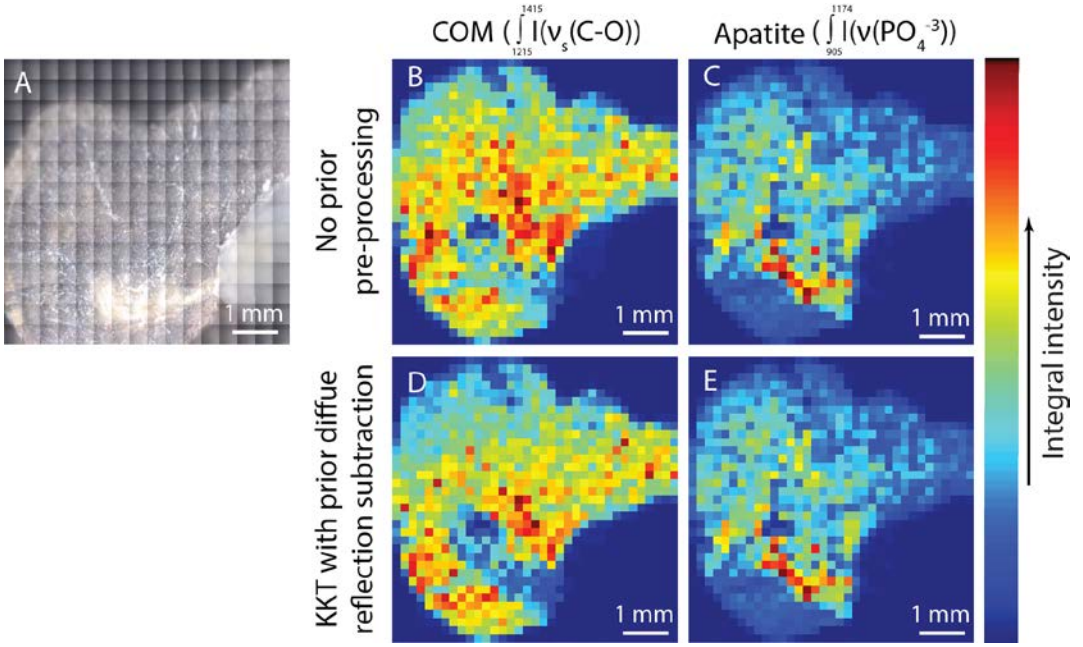

Fig. AI-3. Optical (A) and IR chemical (B-E) images of urinary stone constituted from COM and apatite. (B) and (C) shows distribution of COM and apatite respectively as determined by calculating integral intensity of characteristic spectral bands in the raw spectra; (D) and (E) shows distribution of COM and apatite respectively as determined by calculating integral intensity of characteristic spectral bands in the KKT corrected spectra after the subtraction of diffuse reflection.

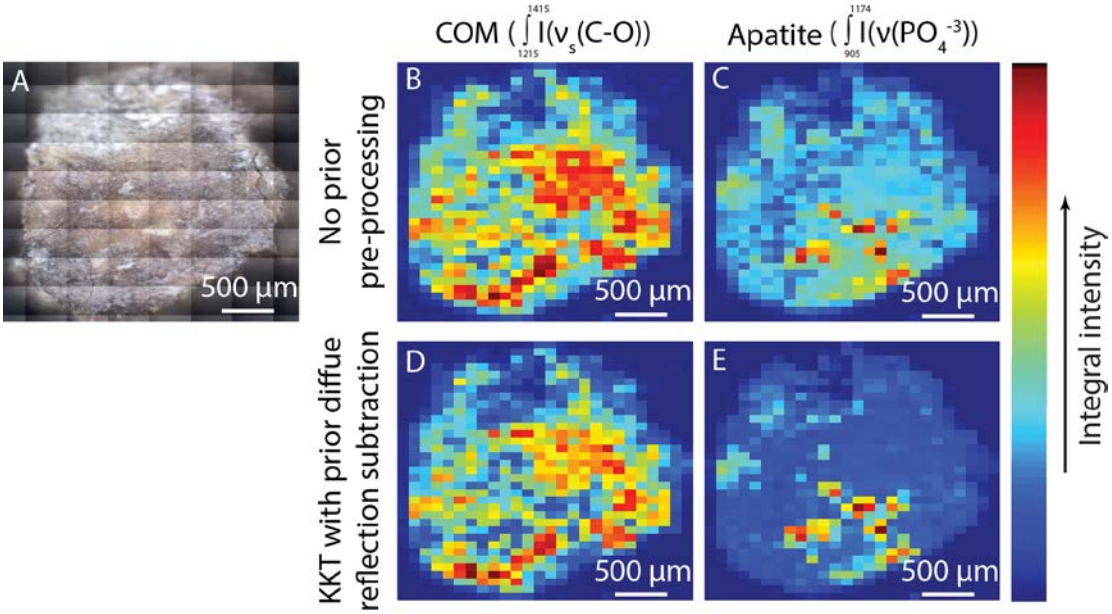

Fig. AI-4. Optical (A) and IR chemical (B-E) images of urinary stone constituted from COM and apatite. (B) and (C) shows distribution of COM and apatite respectively as determined by calculating integral intensity of characteristic spectral bands in the raw spectra; (D) and (E) shows distribution of COM and apatite respectively as determined by calculating integral intensity of characteristic spectral bands in the KKT corrected spectra after the subtraction of diffuse reflection.

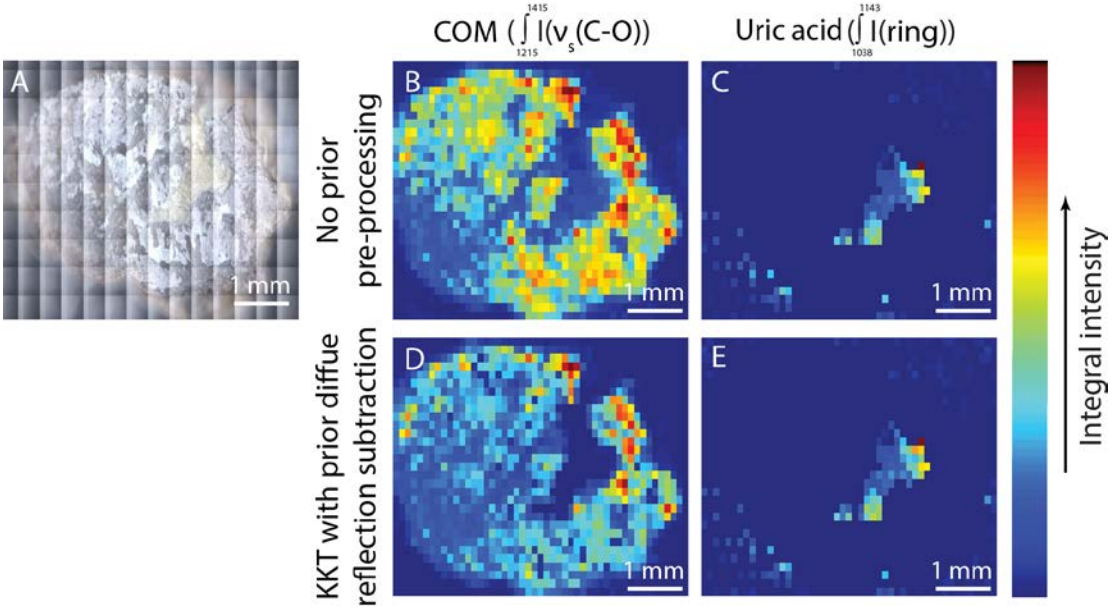

Fig. AI-5. Optical (A) and IR chemical (B-E) images of urinary stone constituted from COM and uric acid. (B) and (C) shows distribution of COM and uric acid respectively as determined by calculating integral intensity of characteristic spectral bands in the raw spectra; (D) and (E) shows distribution of COM and uric acid respectively as determined by calculating integral intensity of characteristic spectral bands in the KKT corrected spectra after the subtraction of diffuse reflection.

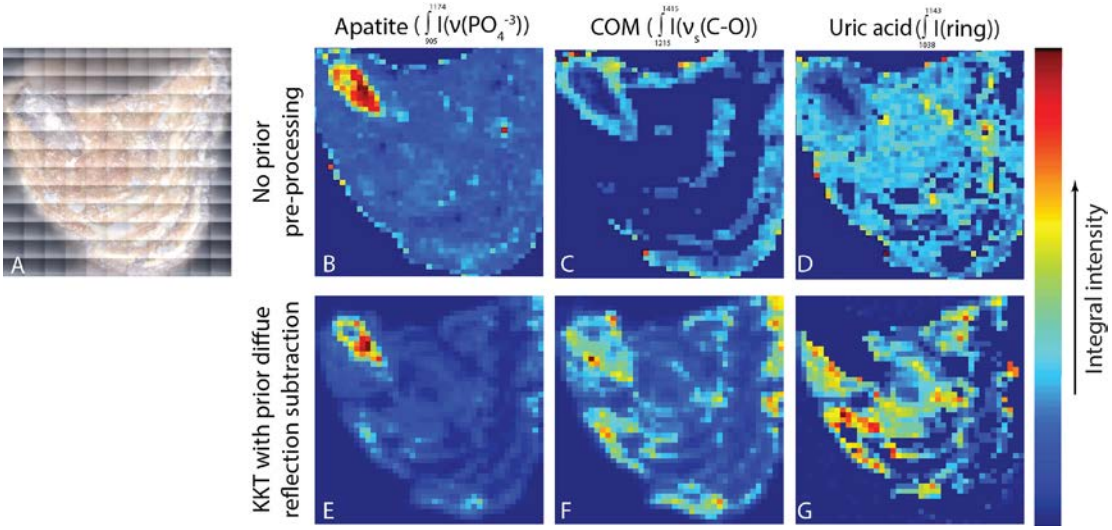

Fig. AI-6. Optical (A) and IR chemical (B-G) images of urinary stone constituted from apatite, COM and uric acid. (B), (C) and (D) shows distribution of apatite, COM and uric acid respectively as determined by calculating integral intensity of characteristic spectral bands in the raw spectra; (E), (F) and (G) shows distribution of apatite, COM and uric acid respectively as determined by calculating integral intensity of characteristic spectral bands in the KKT corrected spectra after the subtraction of diffuse reflection.

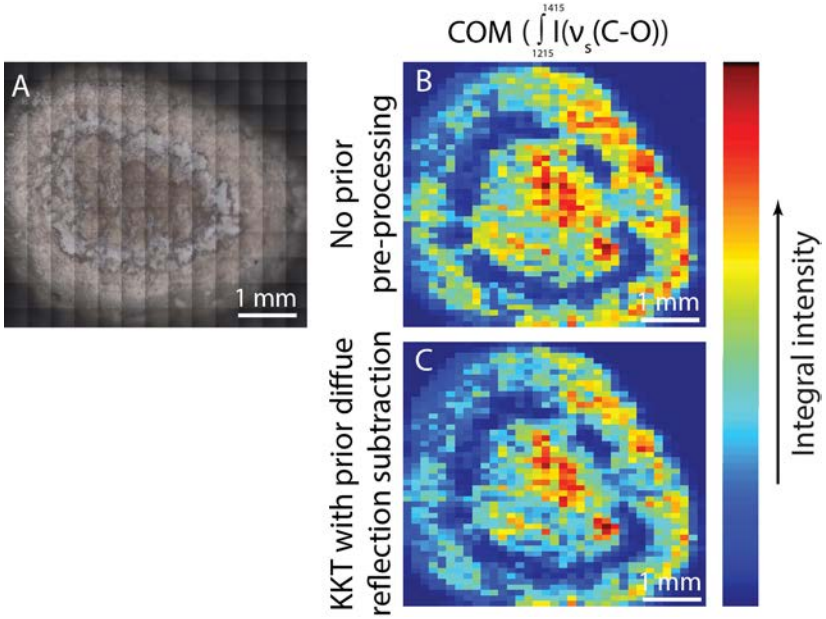

Fig. AI-7. Optical (A) and IR chemical (B, C) images of urinary stone constituted from COM. (B) shows distribution of COM as determined by calculating integral intensity of characteristic spectral bands in the raw spectra; (C) shows distribution of COM as determined by calculating integral intensity of characteristic spectral bands in the KKT corrected spectra after the subtraction of diffuse reflection.

Appendix II

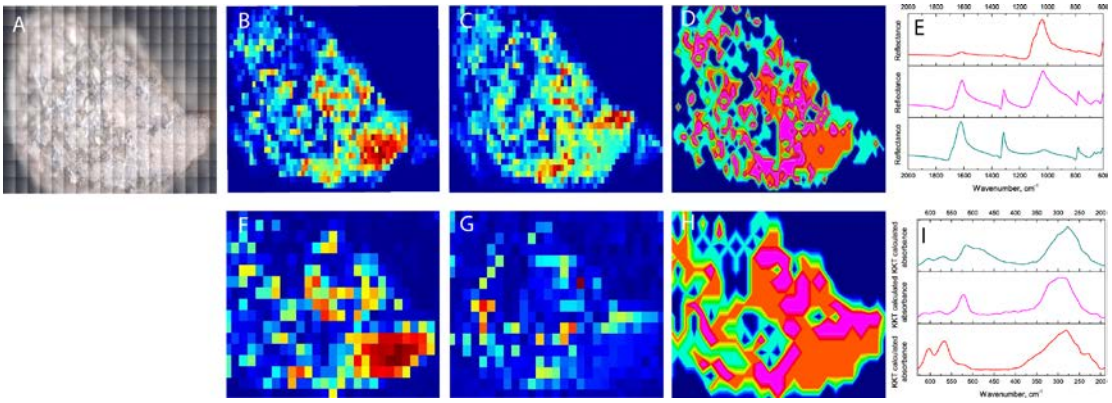

Fig. AII-1. Optical (A), MIR (B-D) and FIR (E-I) chemical images of urinary stone constituted from apatite and COM. (B) and (C) shows distribution of apatite and COM respectively as determined by calculating integral intensity of characteristic spectral bands in the raw MIR spectra; (E) and (G) shows distribution of apatite and COM respectively as determined by calculating integral intensity of characteristic spectral bands in the raw FIR spectra; (D) and (H) shows MIR and FIR chemical images created based on the HCA analysis; (E) and (I) shows characteristic spectra in each group identified by the HCA in (D) and (H) respectively.

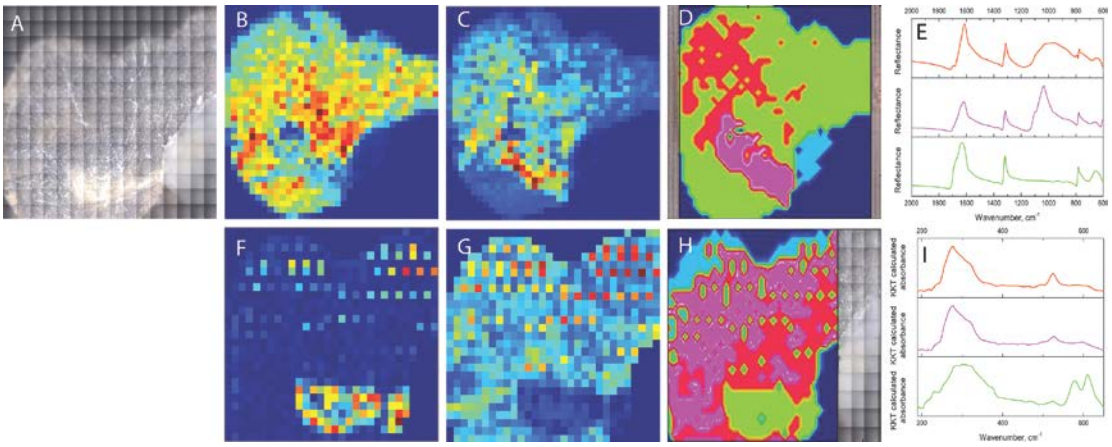

Fig. AII-2. Optical (A), MIR (B-D) and FIR (E-I) chemical images of urinary stone constituted from COM and apatite. (B) and (C) shows distribution of COM and apatite respectively as determined by calculating integral intensity of characteristic spectral bands in the raw MIR spectra; (E) and (G) shows distribution of COM and apatite respectively as determined by calculating integral intensity of characteristic spectral bands in the raw FIR spectra; (D) and (H) shows MIR and FIR chemical images created based on the HCA analysis; (E) and (I) shows characteristic spectra in each group identified by the HCA in (D) and (H) respectively.

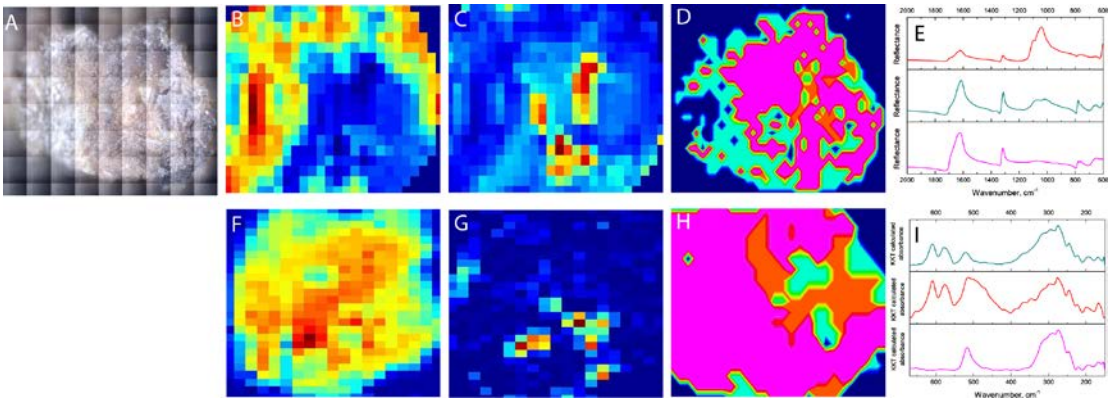

Fig. AII-3. Optical (A), MIR (B-D) and FIR (E-I) chemical images of urinary stone constituted from COM and apatite. (B) and (C) shows distribution of COM and apatite respectively as determined by calculating integral intensity of characteristic spectral bands in the raw MIR spectra; (E) and (G) shows distribution of COM and apatite respectively as determined by calculating integral intensity of characteristic spectral bands in the raw FIR spectra; (D) and (H) shows MIR and FIR chemical images created based on the HCA analysis; (E) and (I) shows characteristic spectra in each group identified by the HCA in (D) and (H) respectively.

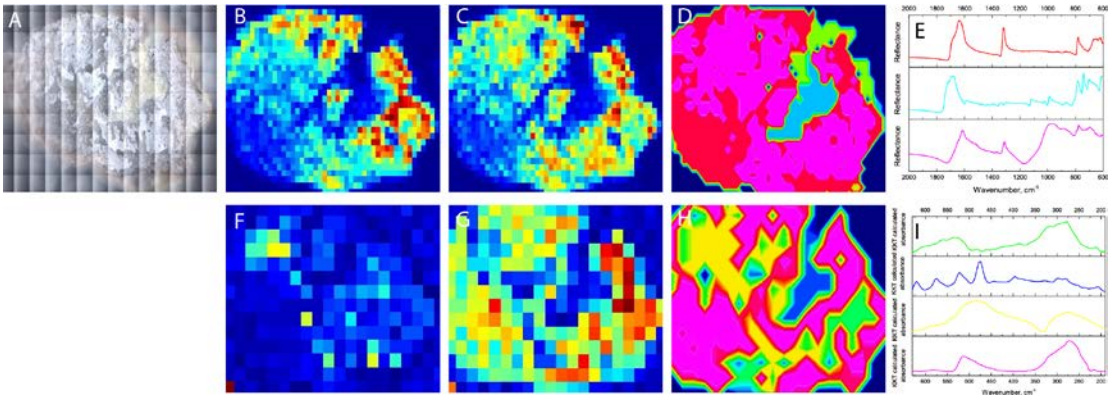

Fig. AII-4. Optical (A), MIR (B-D) and FIR (E-I) chemical images of urinary stone constituted from uric acid and COM. (B) and (C) shows distribution of uric acid and COM respectively as determined by calculating integral intensity of characteristic spectral bands in the raw MIR spectra; (E) and (G) shows distribution of uric acid and COM respectively as determined by calculating integral intensity of characteristic spectral bands in the raw FIR spectra; (D) and (H) shows MIR and FIR chemical images created based on the HCA analysis; (E) and (I) shows characteristic spectra in each group identified by the HCA in (D) and (H) respectively.

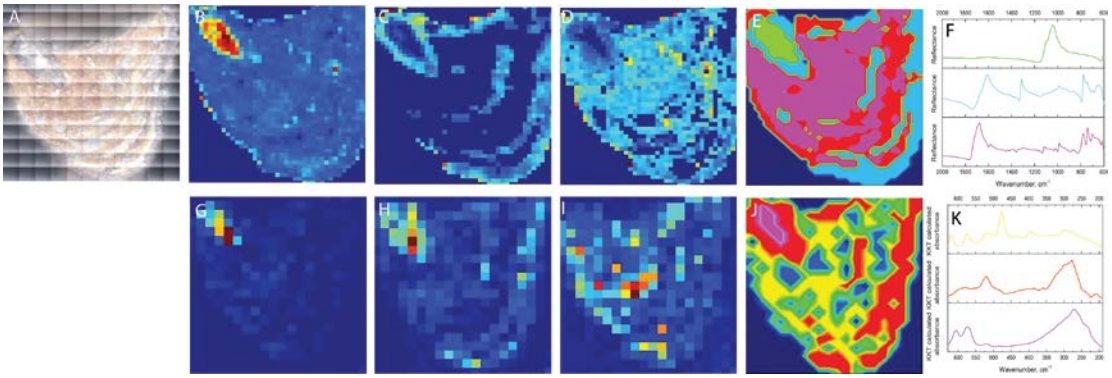

Fig. AII-5. Optical (A), MIR (B-E) and FIR (G-J) chemical images of urinary stone constituted from apatite, COM and uric acid. (B), (C) and (D) shows distribution of apatite, COM and uric acid respectively as determined by calculating integral intensity of characteristic spectral bands in the raw MIR spectra; (G), (H) and (I) shows distribution of apatite, COM and uric acid respectively as determined by calculating integral intensity of characteristic spectral bands in the raw FIR spectra; (E) and (J) shows MIR and FIR chemical images created based on the HCA analysis; (F) and (K) shows characteristic spectra in each group identified by the HCA in (E) and (J) respectively.

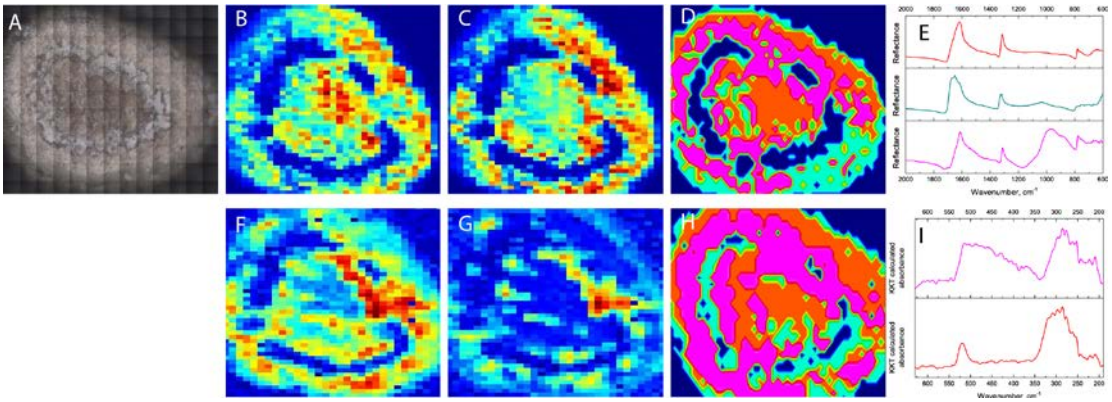

Fig. AII-6. Optical (A), MIR (B-D) and FIR (E-I) chemical images of urinary stone constituted from COM and ACP. (B) and (C) shows distribution of COM and ACP respectively as determined by calculating integral intensity of characteristic spectral bands in the raw MIR spectra; (E) and (G) shows distribution of COM and ACP respectively as determined by calculating integral intensity of characteristic spectral bands in the raw FIR spectra; (D) and (H) shows MIR and FIR chemical images created based on the HCA analysis; (E) and (I) shows characteristic spectra in each group identified by the HCA in (D) and (H) respectively.

Appendix III

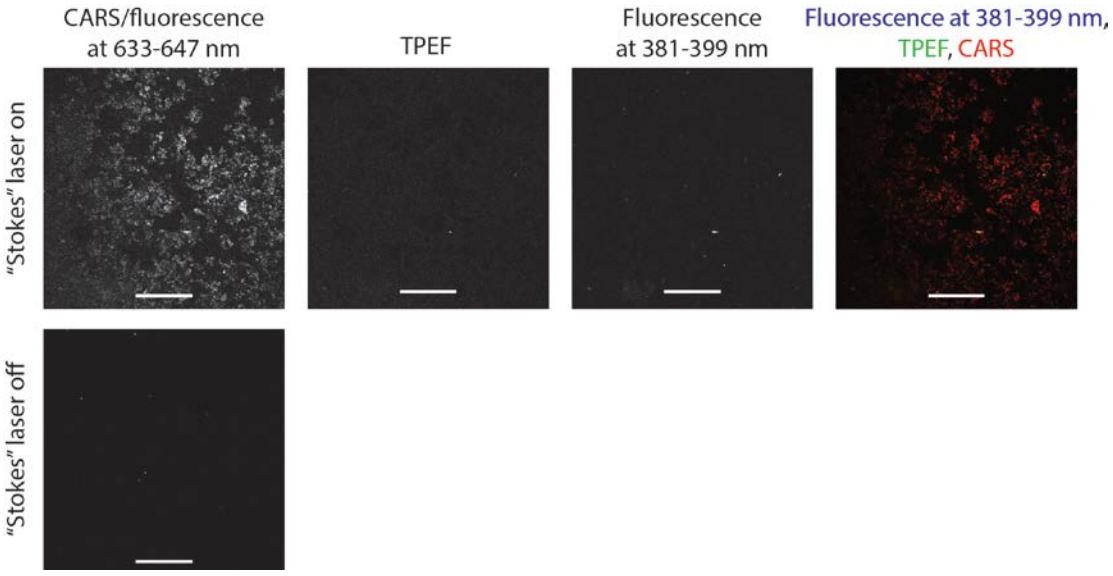

Fig. AIII-1. Multimodal CARS images of synthetic calcium oxalate monohydrate powder recorded with the "Stokes" laser turned on (top row) and off (bottom).

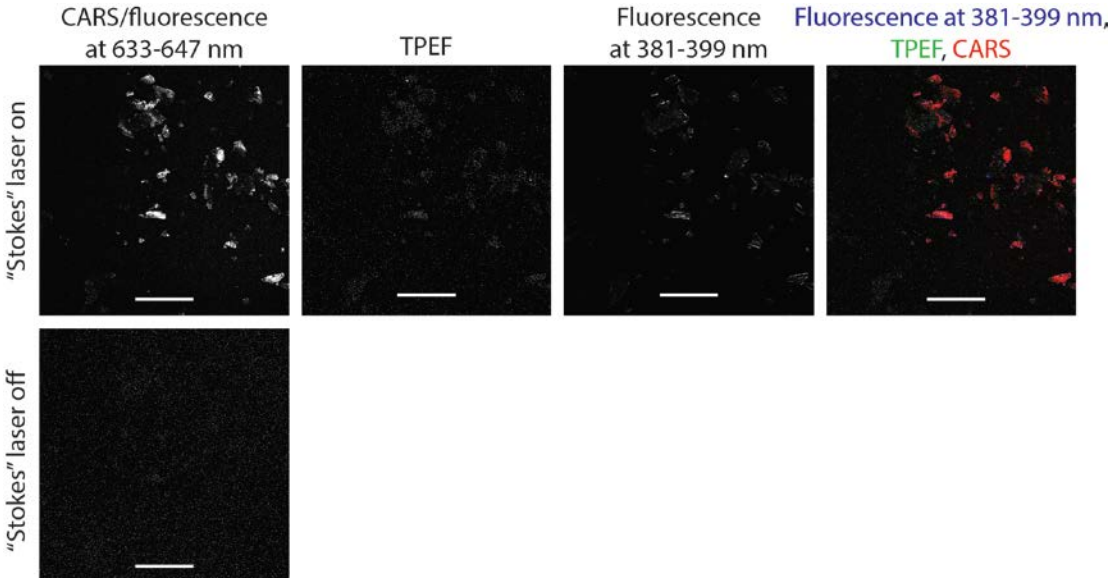

Fig. AIII-2. Multimodal CARS images of synthetic uric acid powder recorded with the "Stokes" laser turned on (top row) and off (bottom).

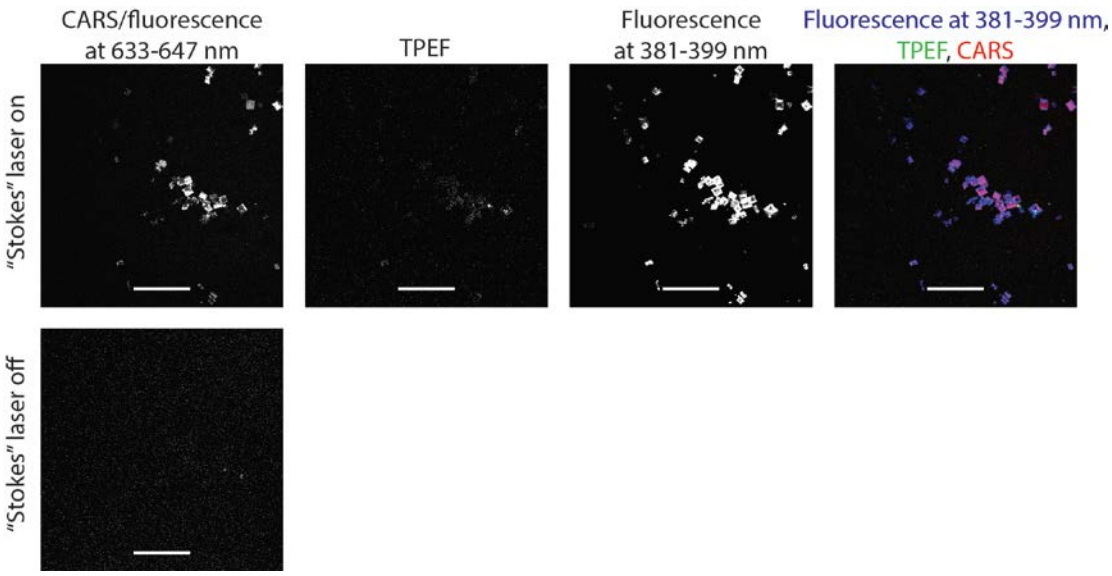

Fig. AIII-3. Multimodal CARS images of synthetic uric acid dihydrate powder recorded with the "Stokes" laser turned on (top row) and off (bottom).

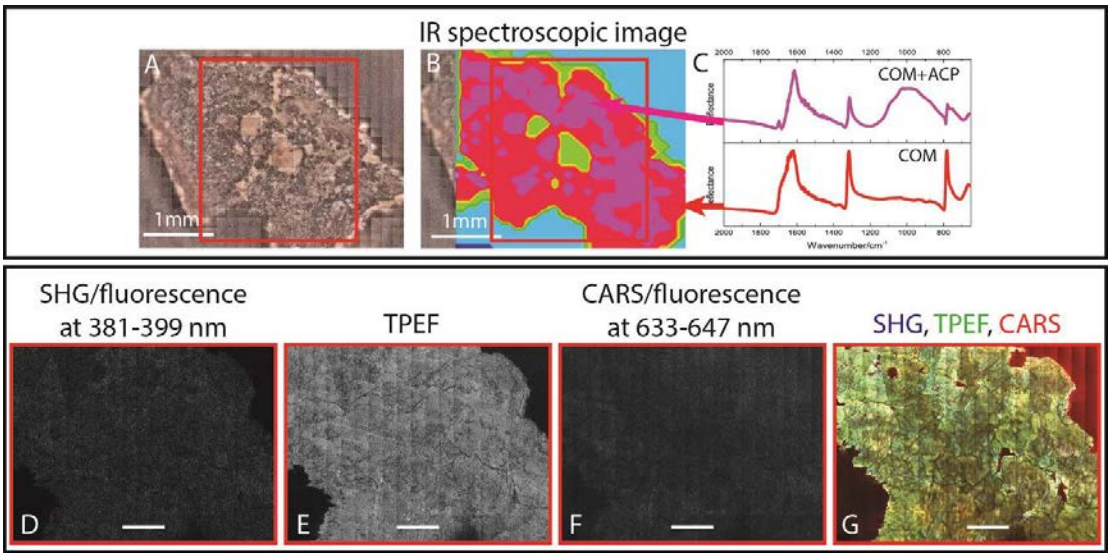

Fig. AIII-4. Optical (A), FT-IR (B) and multimodal CARS chemical (D-I) images of one half of urinary stone constituted from calcium oxalate monohydrate (COM) and amorphous calcium phosphate (ACP); IR reflectance spectra in (C) correspond to areas of different color (chemical composition) in (B). Boxes in (A) and (B) shows the areas imaged by multimodal CARS microscopy: (D) fluorescence at 390 nm signal intensity image; (E) TPEF signal intensity image; (F) CARS and fluorescence at 647 nm intensity image; (G) merged fluorescence at 390 nm (blue), TPEF (green) and CARS/fluorescence at 647 nm (red) intensities image. Scale bar (D-G): 200 μm.

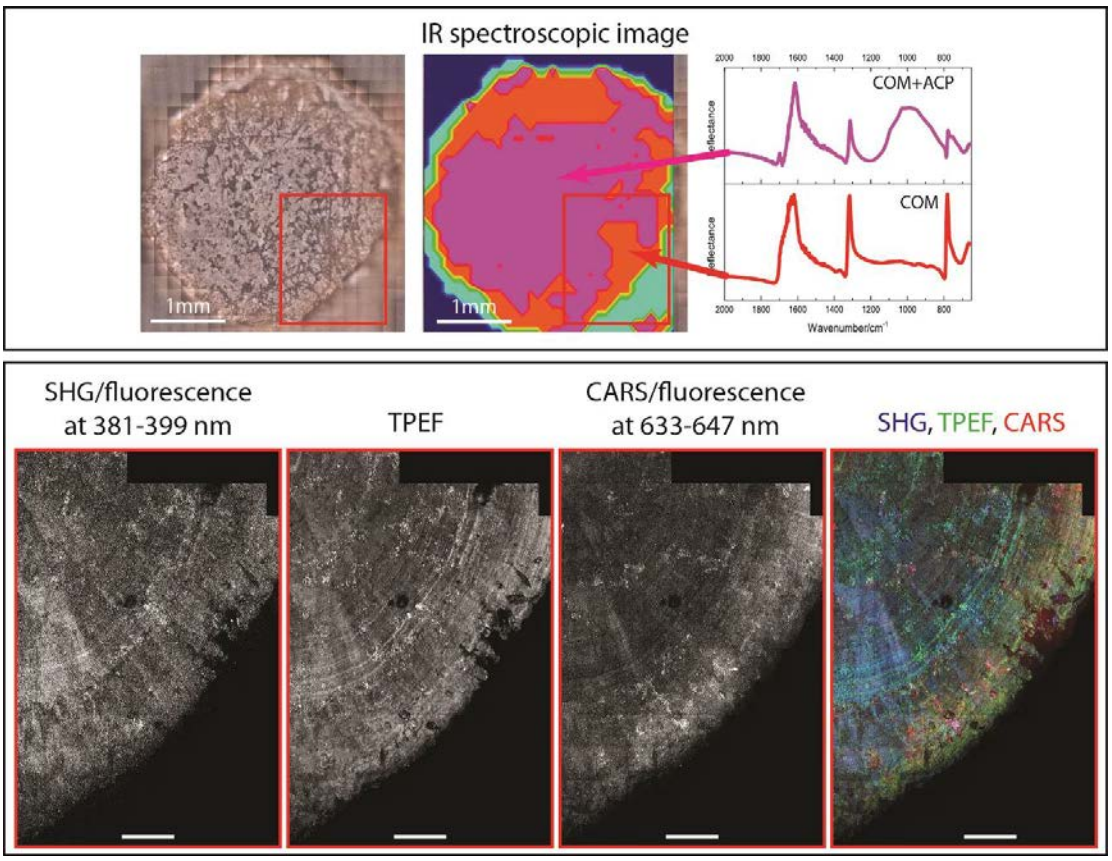

Fig. AIII-5. Optical (A), FT-IR (B) and multimodal CARS chemical (D-I) images of one half of urinary stone constituted from calcium oxalate monohydrate (COM) and amorphous calcium phosphate (ACP); IR reflectance spectra in (C) correspond to areas of different color (chemical composition) in (B). Boxes in (A) and (B) shows the areas imaged by multimodal CARS microscopy: (D) fluorescence at 390 nm signal intensity image; (E) TPEF signal intensity image; (F) CARS and fluorescence at 647 nm intensity image; (G) merged fluorescence at 390 nm (blue), TPEF (green) and CARS/fluorescence at 647 nm (red) intensities image. Scale bar (D-G): 250 µm.

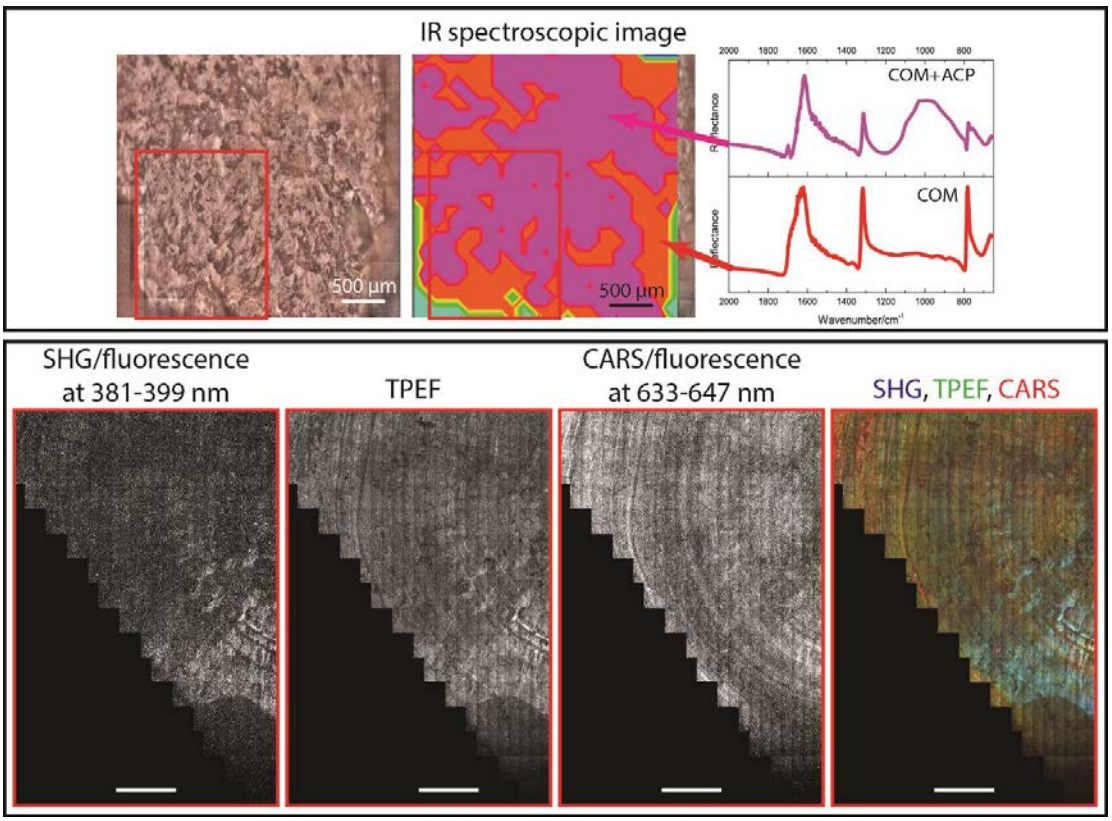

Fig. AIII-6. Optical (A), FT-IR (B) and multimodal CARS chemical (D-I) images of one half of urinary stone constituted from calcium oxalate monohydrate (COM) and amorphous calcium phosphate (ACP); IR reflectance spectra in (C) correspond to areas of different color (chemical composition) in (B). Boxes in (A) and (B) shows the areas imaged by multimodal CARS microscopy: (D) fluorescence at 390 nm signal intensity image; (E) TPEF signal intensity image; (F) CARS and fluorescence at 647 nm intensity image; (G) merged fluorescence at 390 nm (blue), TPEF (green) and CARS/fluorescence at 647 nm (red) intensities image. Scale bar (D-G): 500 µm.

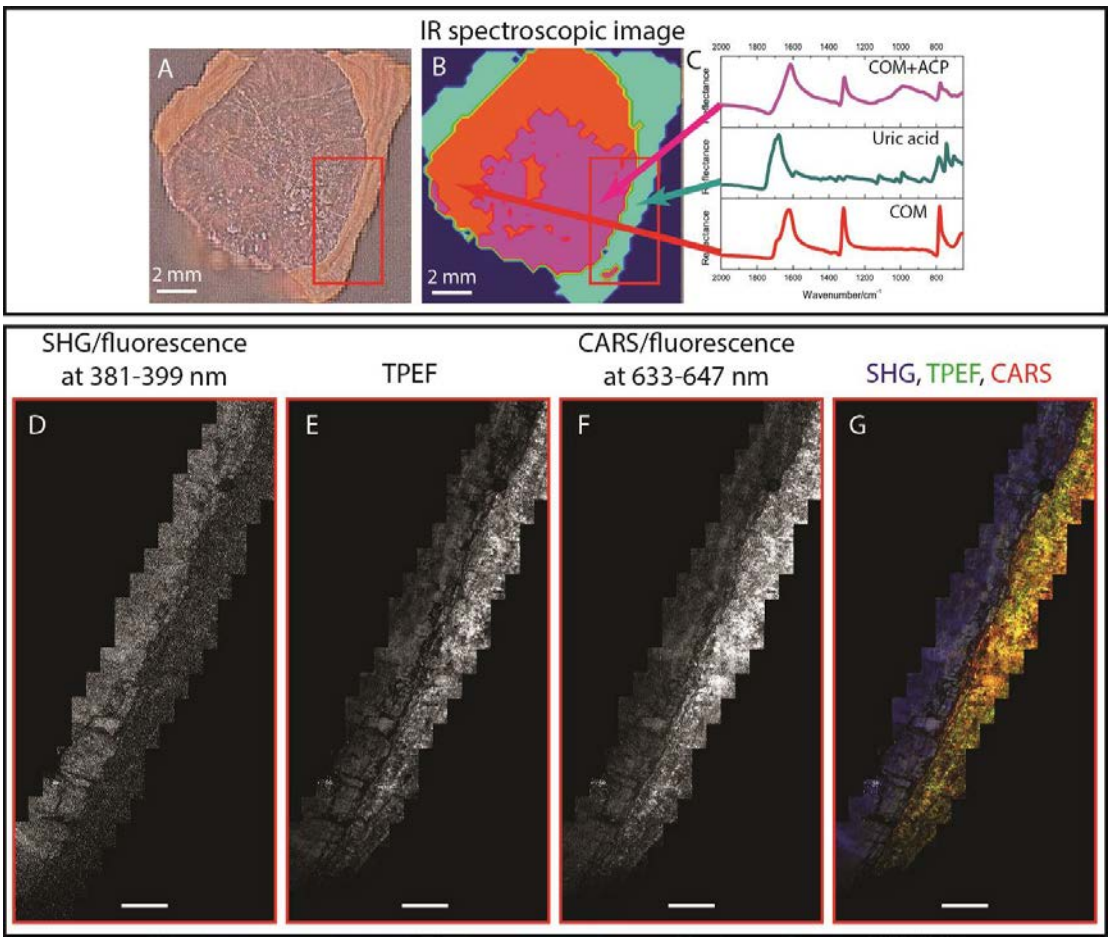

Fig. AIII-7. Optical (A), FT-IR (B) and multimodal CARS chemical (D-I) images of one half of urinary stone constituted from calcium oxalate monohydrate (COM), amorphous calcium phosphate (ACP) and uric acid; IR reflectance spectra in (C) correspond to areas of different color (chemical composition) in (B). Boxes in (A) and (B) shows the areas imaged by multimodal CARS microscopy: (D) fluorescence at 390 nm signal intensity image; (E) TPEF signal intensity image; (F) CARS and fluorescence at 647 nm intensity image; (G) merged fluorescence at 390 nm (blue), TPEF (green) and CARS/fluorescence at 647 nm (red) intensities image. Scale bar (D-G): 200 µm.

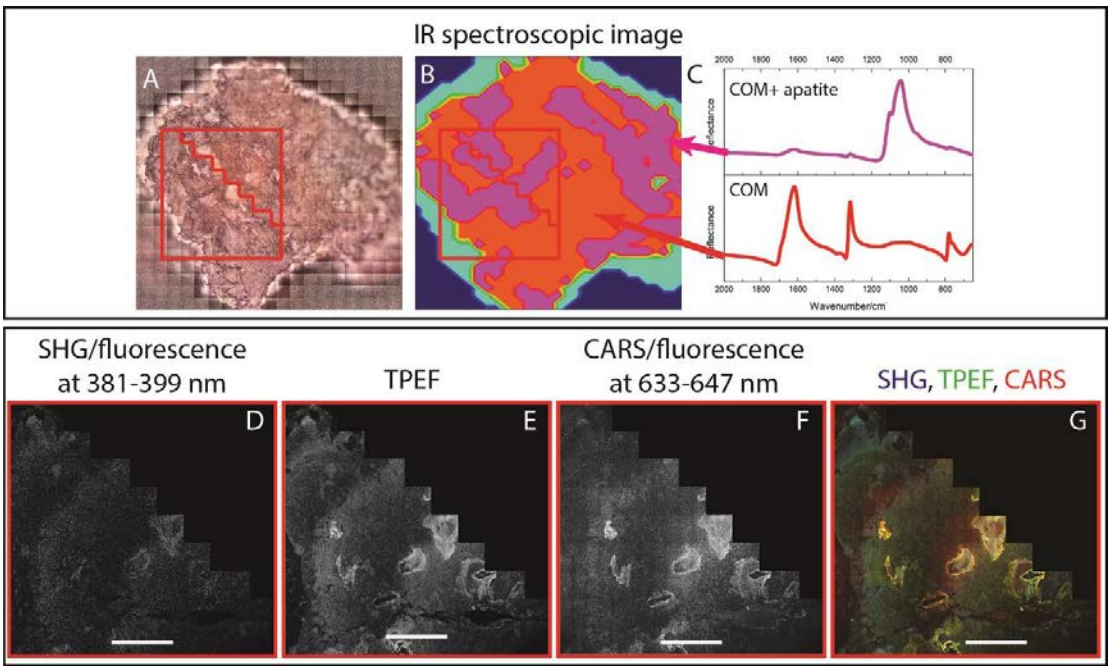

Fig. AIII-8. Optical (A), FT-IR (B) and multimodal CARS chemical (D-I) images of one half of urinary stone constituted from calcium oxalate monohydrate (COM) and apatite; IR reflectance spectra in (C) correspond to areas of different color (chemical composition) in (B). Boxes in (A) and (B) shows the areas imaged by multimodal CARS microscopy: (D) fluorescence at 390 nm signal intensity image; (E) TPEF signal intensity image; (F) CARS and fluorescence at 647 nm intensity image; (G) merged fluorescence at 390 nm (blue), TPEF (green) and CARS/fluorescence at 647 nm (red) intensities image. Scale bar (D-G): 500 µm.

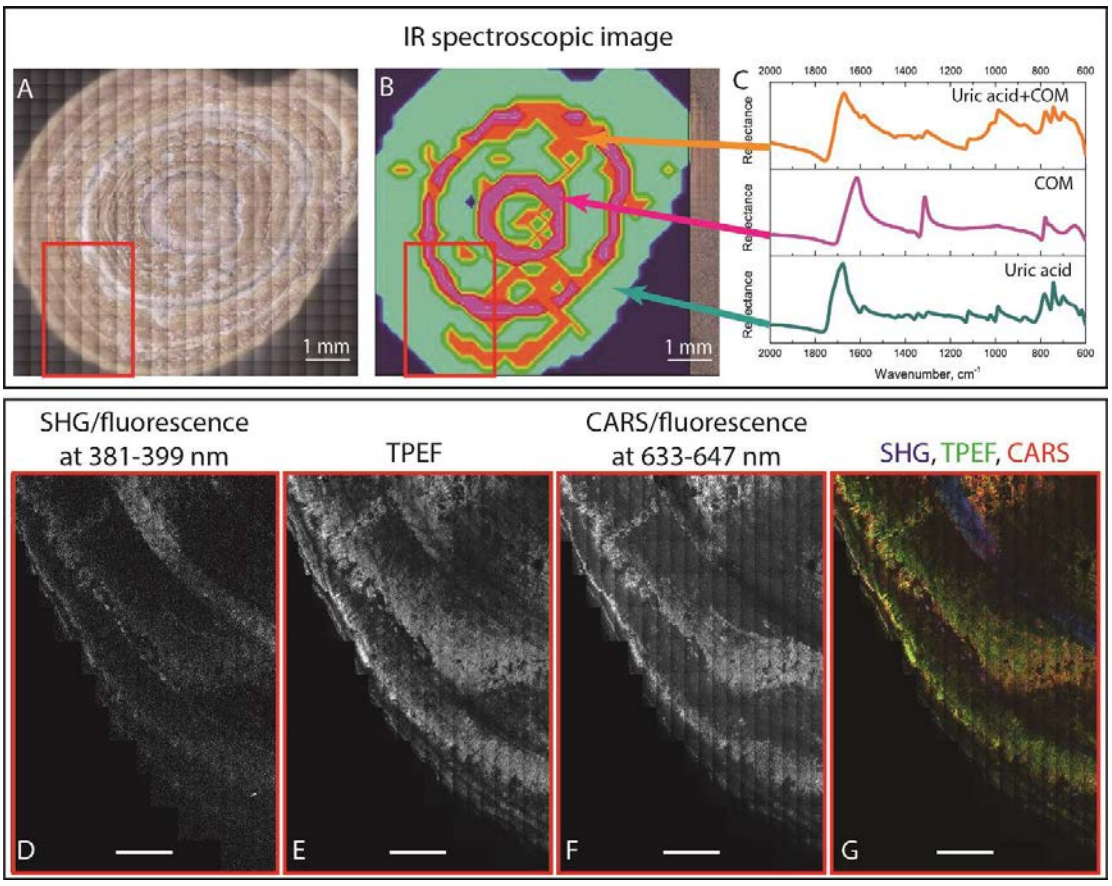

Fig. AIII-9. Optical (A), FT-IR (B) and multimodal CARS chemical (D-I) images of one half of urinary stone constituted from calcium oxalate monohydrate (COM) and uric acid; IR reflectance spectra in (C) correspond to areas of different color (chemical composition) in (B). Boxes in (A) and (B) shows the areas imaged by multimodal CARS microscopy: (D) fluorescence at 390 nm signal intensity image; (E) TPEF signal intensity image; (F) CARS and fluorescence at 647 nm intensity image; (G) merged fluorescence at 390 nm (blue), TPEF (green) and CARS/fluorescence at 647 nm (red) intensities image. Scale bar (D-G): 500 µm.

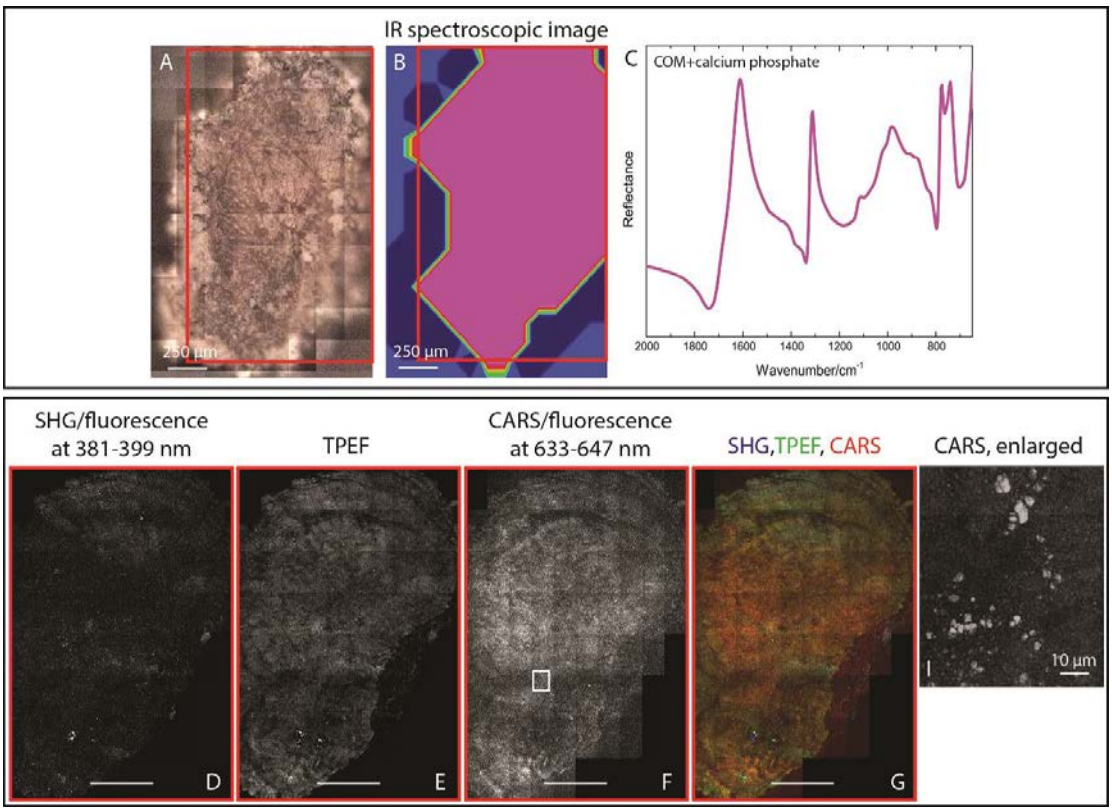

Fig. AIII-10. Optical (A), FT-IR (B) and multimodal CARS chemical (D-I) images of one half of urinary stone constituted from calcium oxalate monohydrate (COM) and amorphous calcium phosphate (ACP); IR reflectance spectra in (C) correspond to areas of different color (chemical composition) in (B). Boxes in (A) and (B) shows the areas imaged by multimodal CARS microscopy: (D) fluorescence at 390 nm signal intensity image; (E) TPEF signal intensity image; (F) CARS and fluorescence at 647 nm intensity image; (G) merged fluorescence at 390 nm (blue), TPEF (green) and CARS/fluorescence at 647 nm (red) intensities image. Box in (F) indicates the enlarged region which contains CARS active structures represented in (I). Scale bar (D-G): 250 µm.

Appendix IV

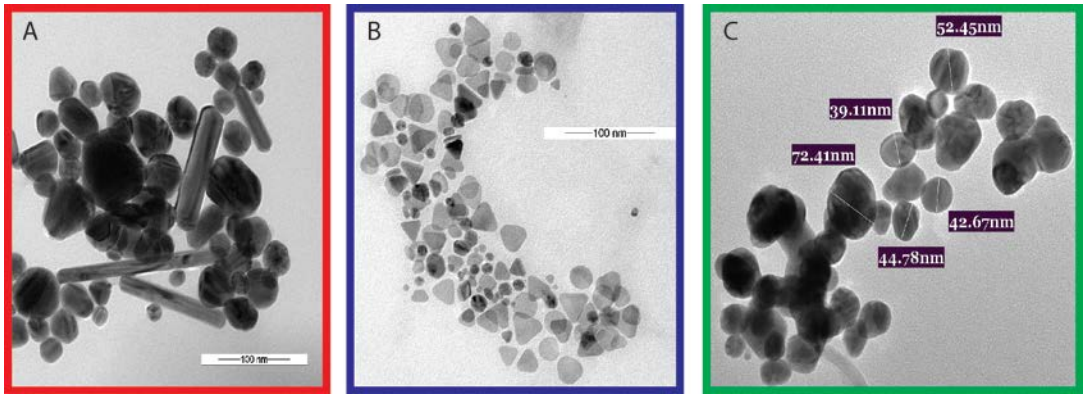

Fig. AIV-1. Transmission electron micrographs of Lee-Meisel (A), Aherne et al. (B), Leopold-Lendl (C) colloids.

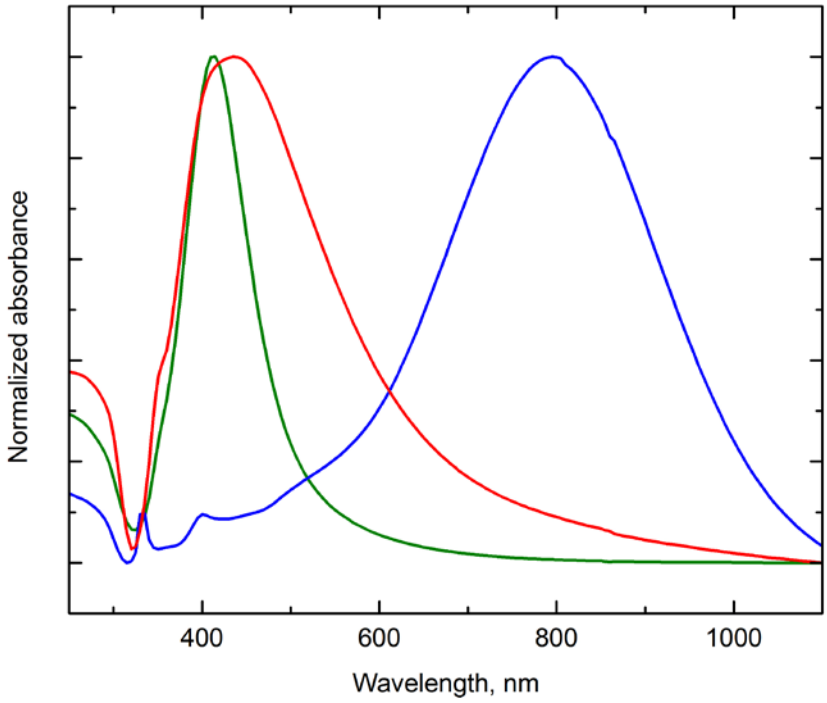

Fig. AIV-2. UV-VIS spectra of Lee-Meisel (red), Leopold-Lendl (green) and Aherne et al. (blue) concentrated colloids.

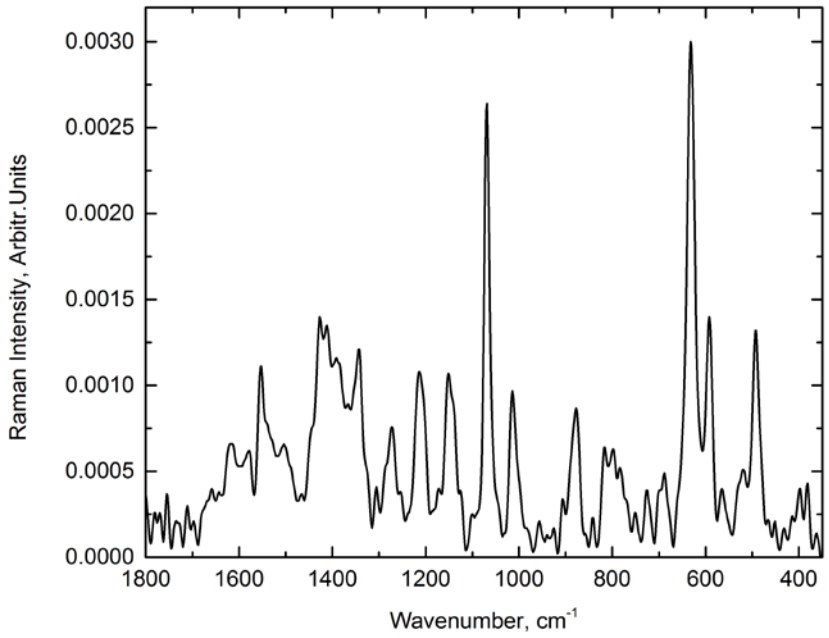

Fig. AIV-3. Raman spectrum of 65 mM uric acid aqueous solution.

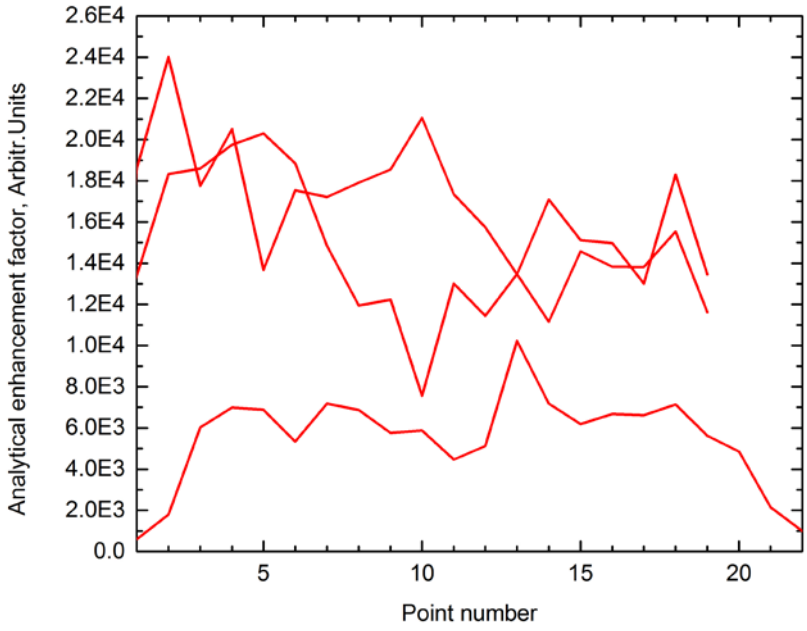

Fig. AIV-4. Profiles of SERS enhancement factor distribution across Lee-Meisel colloidal drops. The analytical enhancement factors were calculated as described by E. C. Le Ru *et al.* [234] for the spectral band at 500 cm^{-1} representing CN bending/in-plane ring deformation vibrations in uric acid. Raman spectrum of 65 mM uric acid solution was used in the calculations.

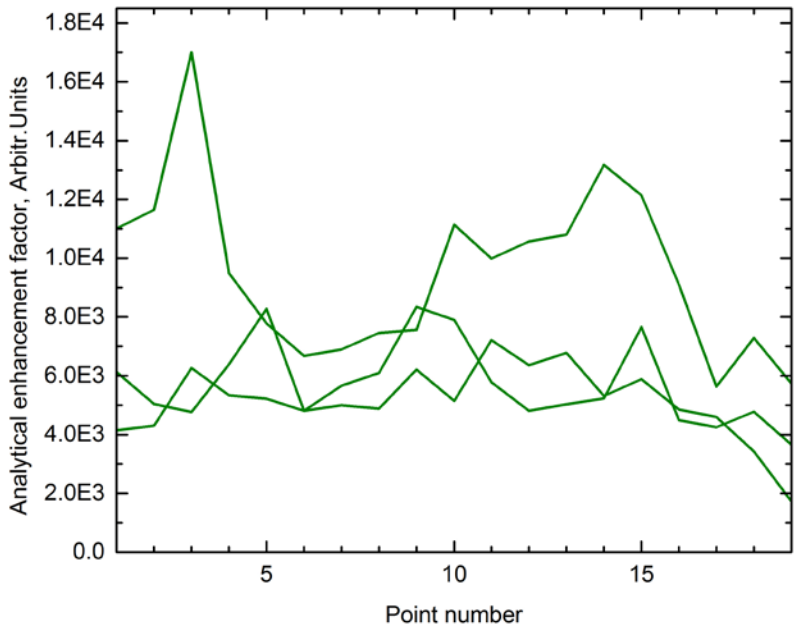

Fig. AIV-5. Profiles of SERS enhancement factor distribution across Leopold-Lendl colloidal drops. The analytical enhancement factors were calculated as described by E. C. Le Ru *et al.* [234] for the spectral band at 500 cm^{-1} representing CN bending/in-plane ring deformation vibrations in uric acid. Raman spectrum of 65 mM uric acid solution was used in the calculations.

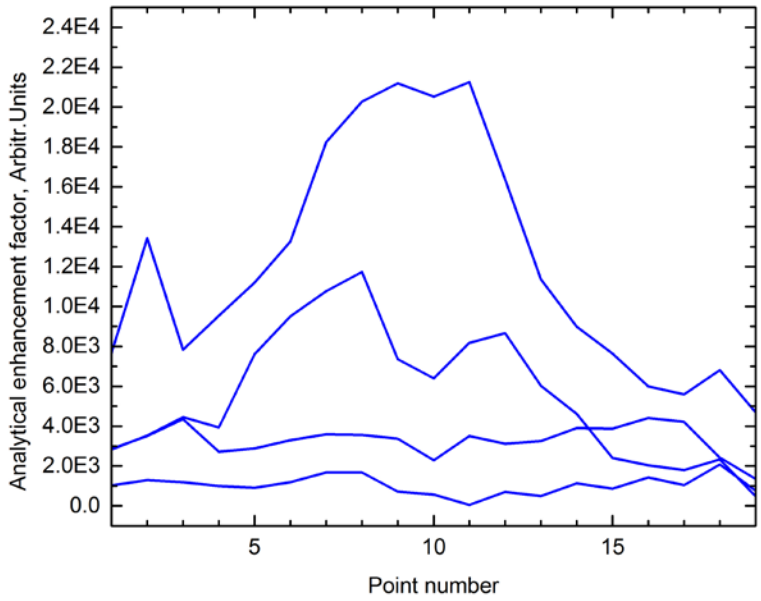

Fig. AIV-6. Profiles of SERS enhancement factor distribution across Aherne *et al.* colloidal drops. The analytical enhancement factors were calculated as described by E. C. Le Ru *et al.* [234] for the spectral band at 500 cm^{-1} representing CN bending/in-plane ring deformation vibrations in uric acid. Raman spectrum of 65 mM uric acid solution was used in the calculations.

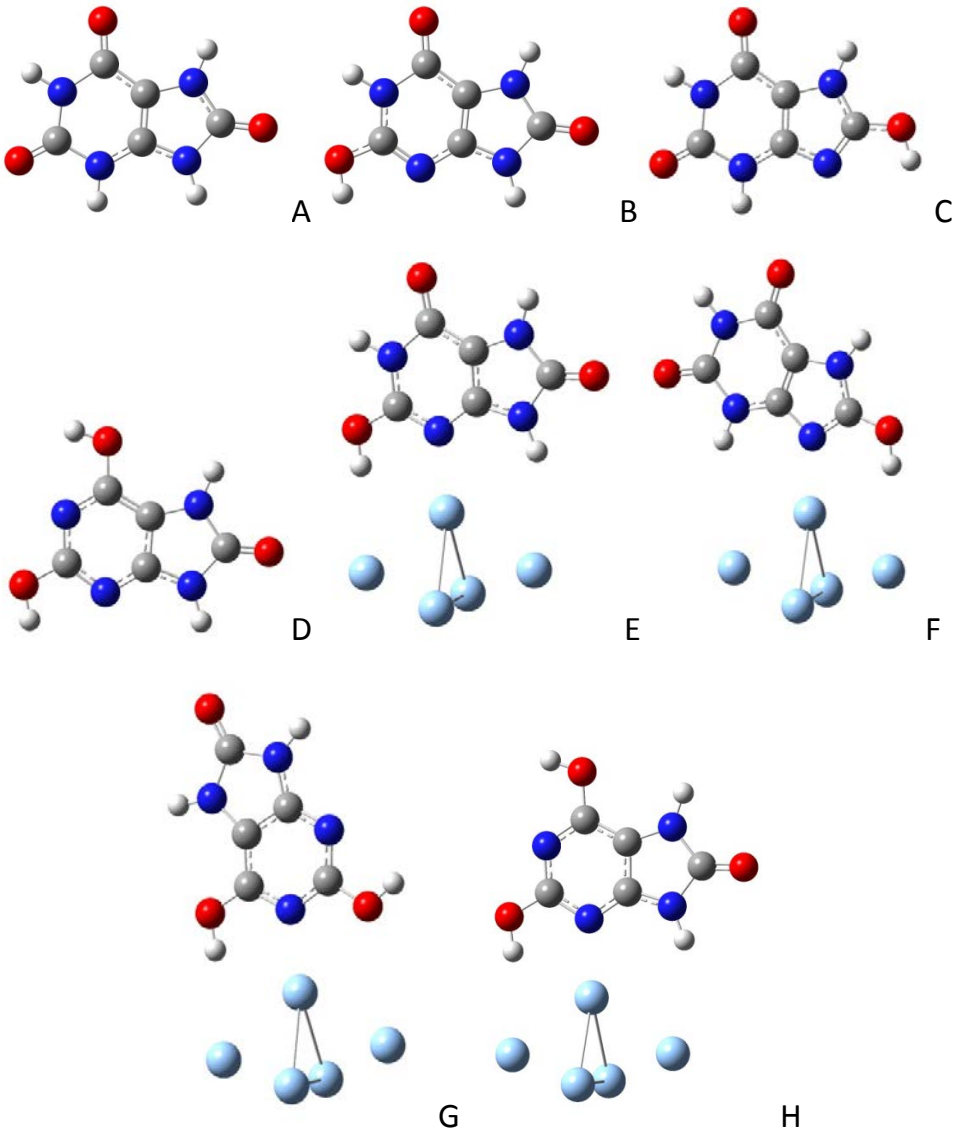

Fig. AIV-7. Uric acid, its tautomers, anions (structures named after M. Altarsha *et al*.[219]) and their complexes with five-atom silver cluster as calculated by DFT B3LYP functional and LANL2DZ basis set: A – monomeric uric acid U0A (ΔE = = 0 kcal/mol); B – uric acid tautomer U1L (ΔE = 3.45 kcal/mol); C – uric acid tautomer U1B (ΔE = 4.52 kcal/mol); D – uric acid tautomer U2G (ΔE = = 6.32 kcal/mol); E – complex of uric acid tautomer U1L and five-atom silver cluster (ΔE = 162.59 kcal/mol); F – complex of uric acid tautomer U1B and five-atom silver cluster (ΔE = 161.52 kcal/mol); G – complex of uric acid tautomer U2G and five-atom silver cluster (ΔE = 162.02 kcal/mol); H – complex of uric acid tautomer U2G and five-atom silver cluster (ΔE = 169.05 kcal/mol). Such large ΔE of the complexes implies that molecular bond is forming between the uric acid molecule and the silver atoms. The corresponding uric acid anions and their complexes with silver presented much larger values of ΔE (i.e., were less stabile) and therefore are not displayed separately.

Acknowledgements

The knowledge and experience gained during the years of my PhD studies widely exceeds the content of this thesis. I would like to take the opportunity and express my most sincere gratitude to the many people who made it possible.

First and foremost, I would like to thank my supervisor, Prof. Valdas Šablinskas, for introducing me to the ways of science, long before the actual start of the PhD studies, for guidance, for the immense patience and support, for encouraging and, sometimes, pushing me forward. Here, I would also like to convey my appreciation to Prof. Gintaras Dikčius, for introducing me, at that time, a lost second-year student, to my supervisor.

Second, I wish to thank my scientific advisor, Prof. Per Uvdal, for welcoming me in MAX IV laboratory in Lund and for, together with Prof. Vivi Vajda, challenging me with new and interesting tasks.

Third, I would like to express my gratitude to Prof. Gerald Steiner and Dr. Roberta Galli for both their hospitality during my stay in their laboratory in Dresden and the immense help in writing the paper. Also, to the fellow students and researchers here in Vilnius University, Faculties of Physics and Chemistry who kindly let me in their laboratories and offered help with experiments. This thesis would not have existed without them. In addition, I greatly acknowledge financial support from the Research Council of Lithuania, Vilnius University Mobility Fund of Doctoral Students and Utrecht Network.

Further, I am grateful to all my colleagues in the Department of General Physics and Spectroscopy for creating a nice and friendly atmosphere to work in. Many thanks go to Justinas for always sharing his knowledge and his manifold help in the laboratory. Especially, I would like to thank Martynas for fun and fruitful everyday discussions and being a great office-mate.

Finally, I am immensely grateful to my family and friends who always support me in all my endeavors. I give my special thanks to Neimantas for challenging me, for listening and making a joke when I most needed it and for taking me on inspiring adventures.